

# Galaxy formation and evolution in the Millennium Simulation

Dissertation der Fakultät für Physik  
der  
Ludwig-Maximilians-Universität München

vorgelegt von Manfred Georg Kitzbichler  
aus Erl, Tirol, Österreich



München, den 1. Juni 2007



# Galaxy formation and evolution in the Millennium Simulation

Dissertation der Fakultät für Physik  
der  
Ludwig-Maximilians-Universität München

vorgelegt von Manfred Georg Kitzbichler  
aus Erl, Tirol, Österreich

München, den 1. Juni 2007

Erstgutachter: Prof. Dr. Simon D. M. White

Zweitgutachter: Prof. Dr. Ralf Bender

Promotionskommission

Vorsitzender: Prof. Dr. Otmar Biebel

1. Prüfer: Prof. Dr. Simon D. M. White

2. Prüfer: Prof. Dr. Martin Faessler (i.V. Prof. Bender)

Weiterer Prüfer: Prof. Dr. Harald Weinfurter

Tag der mündlichen Prüfung: 20. Mai 2008



*Für meine Eltern  
Peter und Katharina*



# Contents

<b>Zusammenfassung (German)</b>	<b>5</b>
<b>Summary</b>	<b>7</b>
<b>1 Introduction</b>	<b>9</b>
1.1 The Universe . . . . .	9
1.2 Linear growth of structure . . . . .	14
1.3 Formation of dark-matter haloes . . . . .	19
1.4 Gas cooling and galaxy formation . . . . .	21
<b>2 The model</b>	<b>23</b>
2.1 The Millennium Simulation . . . . .	23
2.2 The semi-analytic model . . . . .	25
2.2.1 Gas infall and cooling . . . . .	26
2.2.2 Reionisation . . . . .	27
2.2.3 Star formation . . . . .	27
2.2.4 Supernova feedback . . . . .	28
2.2.5 Black hole growth, AGN outflows, and cooling suppression	29
2.2.6 The importance of feedback . . . . .	31
2.2.7 Dust treatment . . . . .	33
2.3 Lightcones . . . . .	38
2.3.1 Spatial replication . . . . .	38
2.3.2 Magnitudes . . . . .	40
2.3.3 Geometry in curved space-time . . . . .	41
<b>3 PLE: Missing Bright Galaxies at High Redshift</b>	<b>45</b>
3.1 Introduction . . . . .	46
3.2 The Models . . . . .	49
3.2.1 From the local LF to the models . . . . .	49
3.2.2 The <i>K</i> -band LF as a consistency test . . . . .	52
3.3 Comparison of <i>K</i> -band Selected Redshift Distributions . . . . .	54
3.4 Discussion and Conclusions . . . . .	56

## Contents

---

<b>4</b>	<b>High redshift galaxies</b>	<b>63</b>
4.1	Introduction . . . . .	64
4.2	The Model . . . . .	66
4.2.1	The Millennium dark matter simulation . . . . .	66
4.2.2	The basic semi-analytic model . . . . .	66
4.2.3	Improved dust treatment for the fiducial model . . . . .	67
4.2.4	Making mock observations: lightcones . . . . .	69
4.3	Results . . . . .	76
4.3.1	Number Counts . . . . .	76
4.3.2	Redshift Distributions for $K$ -selected samples . . . . .	77
4.3.3	Luminosity Function evolution . . . . .	78
4.3.4	The evolution of the stellar mass function . . . . .	83
4.3.5	The evolution of the colour-magnitude relation . . . . .	86
4.4	Discussion and Conclusions . . . . .	87
<b>5</b>	<b>Galaxy pairs</b>	<b>91</b>
5.1	Introduction . . . . .	92
5.2	Model . . . . .	94
5.2.1	The Millennium N-body simulation . . . . .	94
5.2.2	The semi-analytic model . . . . .	95
5.2.3	Merger rates and pair counts . . . . .	96
5.2.4	Fiducial merger rates of DM haloes and galaxies . . . . .	98
5.2.5	Dependence on mass and luminosity . . . . .	100
5.2.6	The mock lightcone . . . . .	102
5.3	Methods . . . . .	104
5.3.1	Finding pairs . . . . .	104
5.3.2	Identifying mergers . . . . .	107
5.4	Results . . . . .	108
5.4.1	Redshift distribution of pairs . . . . .	108
5.4.2	The average merging time of galaxy pairs . . . . .	110
5.4.3	Completeness and contamination . . . . .	113
5.4.4	Distribution of merging times . . . . .	115
5.4.5	Pair versus merger fraction evolution . . . . .	117
5.5	Conclusions . . . . .	117
<b>6</b>	<b>Conclusions</b>	<b>123</b>
6.1	Discussion of results . . . . .	123
6.2	Outlook . . . . .	126
<b>A</b>	<b>Appendix</b>	<b>127</b>
A.1	Possible improvements to the model . . . . .	127



## Contents

---

A.1.1	Star formation in satellites . . . . .	128
A.1.2	Disk sizes . . . . .	130
A.1.3	Interactions . . . . .	130
A.1.4	Gas recycling . . . . .	130
A.2	WMAP 3rd year cosmology . . . . .	130
	<b>Acknowledgements</b>	<b>135</b>
	<b>Curriculum Vitae</b>	<b>137</b>
	<b>Bibliography</b>	<b>141</b>

## Contents

---

# Zusammenfassung

Diese Doktorarbeit befaßt sich mit der Frage wie Galaxien entstehen und wie sie sich in weiterer Folge entwickeln.

In Zusammenarbeit mit D. Croton, G. de Lucia, V. Springel und S.D.M. White bediente ich mich der Millennium Simulation, einer extrem großen ‘N-body’ Simulation der gravitativen Wechselwirkung Dunkler Materie (engl. dark matter; DM) in einem kosmologischen Volumen, die im Jahre 2005 am MPA ausgeführt wurde, um die Vorhersagen der neuesten Generation semi-analytischer Modelle zur Galaxienentstehung zu untersuchen. Diese Modelle enthalten einen neuen Modus für die Regulierung von Sternentstehung durch negative Rückkopplung (engl. feedback) von “Aktiven Galaktischen Kernen” (engl.: AGN), welche ihren Ursprung in super-massiven schwarzen Löchern haben, die umgebende Materie verschlucken und in Energie umwandeln. Da Hinweise auf diesen Mechanismus hauptsächlich im Radiobereich beobachtet werden, wird dieses Feedback “Radiomode” genannt. Es wirkt Flüssen kalten Gases (engl. cooling flows) in Dunkle Materie Halos entgegen, welche Galaxienhaufen beheimaten, die ansonsten viel höhere Sternentstehungsraten ihrer zentralen Galaxie zeigen würden, als beobachtet wird. Bisherige Arbeiten von [Croton et al. \(2006\)](#) und [De Lucia & Blaizot \(2007\)](#) haben gezeigt, daß mit dem neuen semi-analytischen Modell die lokale Galaxienpopulation ziemlich genau reproduziert werden kann. Um die Entwicklung der Galaxien zu höheren Rotverschiebungen zu studieren, sind die semi-analytischen Vorhersagen mit einer Anzahl von Beobachtungen in verschiedenen Filterbändern verglichen worden, insbesondere mit zwei neuen Anstrengungen einen kompletten Multiwellenlängen-Datensatz von Galaxien hoher Rotverschiebung zu erhalten, die derzeit von der DEEP2 ([Davis et al. 2001](#)) und der COSMOS ([Scoville et al. 2006](#)) Kollaboration unternommen werden. Ziel war es, einen Vergleich auf breiter Basis durchzuführen, um unser physikalisches Modell möglichst exakt bestimmen zu können. Folglich wurden eine ganze Reihe von beobachteten Galaxieneigenschaften mit den Modellvorhersagen verglichen, so etwa die räumliche Galaxienverteilung (engl. clustering), Helligkeitsfunktionen (engl. luminosity functions; LF), stellare Massenfunktionen (SMF), Galaxiendichte am Himmel und Rotverschiebungsverteilung bei einem bestimmten Magnitudenlimit. Um den Vergleich zwischen Simulationen und den neuen Beobachtungen bei mittleren und hohen Rotverschiebungen zu erleichtern, ist es sehr nützlich eine Anzahl unabhängiger simulierter Galaxienbeobachtungen (engl. mocks) zur Verfügung zu haben, die ausreichend gute Statistik über die Unterschiede in der Galaxiendichte entlang unterschiedlicher Sichtlinien (engl. cosmic variance) liefern. Zu diesem Zweck habe ich ein Computerprogramm entwickelt, das die simulierten Galaxien beliebiger Rotverschiebung errechnet, die auf dem sogenannten Vergangenheitslichtkegel (ein Ausdruck aus der Relativitätstheorie; engl. lightcone) eines hypothetischen Beobachters liegen, wobei die Periodizität des Simulationsvolumens ausgenutzt wird, ohne daß Galaxien repliziert werden. Als Ergebnis stellt dieses Programm genau interpolierte Rotverschiebungen, Positionen, Magnituden in

## Zusammenfassung

---

verschiedenen Bezugssystemen, Staubextinktion, sowie alle intrinsischen Galaxieeigenschaften wie stellare Masse und SFR zur Verfügung. Unter Verwendung dieses Werkzeuges ist es auch möglich, Vorhersagen für zukünftige Galaxiensurveys zu machen, welche tiefer ins All blicken werden als gegenwärtig möglich. Derzeit werden die Mock Kataloge von den DEEP2 und COSMOS-Teams benutzt, als Vergleichsdaten im allgemeinen, und für die Beurteilung von Selektionseffekten und um die Datenreduktion zu verbessern im besonderen. Erste Vergleiche von Galaxienzählungen und Rotverschiebungsverteilung ergaben vielversprechende Resultate und zeigten gute Übereinstimmung im Bereich niedriger bis mittlerer Rotverschiebungen. Wir stellen daher fest, daß unser gegenwärtiges Verständnis der Prozesse, die die Galaxieentstehung und -entwicklung von den allerersten Objekten bis zur heute beobachteten Galaxienpopulation zwar realistisch aber noch unvollständig ist. Insbesondere haben die Modellierung der Wechselwirkung zwischen Sternentstehung und negativem Feedback und der verschiedenen Prozesse, die Satellitengalaxien in den großen Galaxiehaufen beeinflussen, noch einiges Potential für Verbesserung.

Im folgenden gebe ich einen kurzen Überblick der Themen in dieser Doktorarbeit. Nach einer Einführung in Kapitel 1, welche die Geometrie des Universums behandelt, die Voraussetzung für jegliches Modell, beschreibe ich unser semi-analytisches Modell der Galaxienentstehung in Kapitel 2, wo auch erklärt wird, wie man realistische Mock Beobachtungen der simulierten Galaxien konstruiert. Zuerst wird in Kapitel 3 gezeigt, daß ein einfaches Modell, das annimmt, daß sich Galaxien in den letzten 10 Milliarden Jahren nur in ihrer Helligkeit verändert haben, aber weder neu gebildet noch durch Verschmelzung (engl. merging) vernichtet wurden, nicht die beobachtete Entwicklung der Galaxienpopulation im Universum erklären kann. Diese Tatsache kann im Kontext hierarchischer Modelle verstanden werden, in denen massive und leuchtkräftige Galaxien gebildet werden indem sich kleinere Objecte verschmelzen. Konsequenterweise werden daher in Kapitel 4 die Vorhersagen unseres beträchtlich komplexeren semi-analytischen Modelles untersucht, welches auf einer N-body Simulation des hierarchischen Wachstums der Dunklen Materie Strukturen basiert. Für diese Analyse wurde eine Anzahl von Mock "Lightcones" für den direkten Vergleich mit den Daten konstruiert, welcher recht gute Übereinstimmung zwischen Modell und Beobachtungen bei niedrigen Rotverschiebungen und für helle Magnituden ergibt. Diese Lightcones stellen einen der größten derzeit verfügbaren Datensatz realistisch simulierter Beobachtungen dar. Sie können zum Beispiel für den Test von Datenanalysetechniken benutzt werden, wie sie normalerweise auf reale Beobachtungen angewendet werden, um anhand eines gut definierten Katalogs künstlicher Galaxien herauszufinden, wie gut die Bestimmung von Galaxieeigenschaften aus den Beobachtungsdaten funktioniert. In Kapitel 5 wird gezeigt, wie man die Entwicklung der Galaxienverschmelzungsrate (engl. merger rate) aus Beobachtungen projizierter Galaxiepaare ableiten kann. Interessanterweise finden wir, daß die dafür notwendige Kalibrierung erheblich von jener abweicht, die gewöhnlich in den bisherigen Studien angenommen wurde. Zusätzlich zeigen wir, daß die Verschmelzungsrate der Galaxien und jene der Dunklen Materie eine deutlich unterschiedliche Abhängigkeit mit der Rotverschiebung an den Tag legen. Infolgedessen stellen wir fest, daß Studien der Verschmelzungsrate als Test für die kosmische Strukturbildung, wofür sie ursprünglich konzipiert wurden, nicht sehr geeignet sind, aber von großer Hilfe sein können, die Entstehung und Entwicklung der Galaxien in einem hierarchischen Universum zu verstehen.

Schließlich werden diese Resultate in Kapitel 6 zusammengefaßt und diskutiert. Daran anschließend gebe ich auch einen kurzen Ausblick darauf, wie es in Zukunft weitergehen könnte.

## Summary

This Thesis addresses the topic of galaxy formation and evolution in the universe.

In collaboration with D. Croton, G. de Lucia, V. Springel, and S.D.M. White, I made use of the Millennium simulation, a very large N-body simulation of dark-matter evolution in a cosmological volume carried out at the MPA in 2005 by [Springel et al. \(2005\)](#), to explore the predictions made by the most recent generation of semi-analytic models for galaxy formation. These models are incorporating a new mode of feedback from active galactic nuclei (AGN), which have their origins in super-massive black holes accreting mass and turning it into energy. Because of its observational signature in the radio regime this feedback is called “radio mode” and it counteracts the cooling flows of cold gas in undisturbed dark-matter haloes hosting galaxy clusters, which would otherwise show much higher star-formation of their central object than is observed. Previous work by [Croton et al. \(2006\)](#) and [De Lucia & Blaizot \(2007\)](#) has shown that with the new semi-analytic model the population of local galaxies can be reproduced quite accurately. In order to study the evolution of the population out to higher redshifts, the semi-analytic predictions have been compared to a number of observations in various filter bands, in particular to two recent efforts to get a comprehensive multi-wavelength dataset of high redshift galaxies carried out by the DEEP2 ([Davis et al. 2001](#)) and COSMOS ([Scoville et al. 2006](#)) collaborations. The approach taken was to perform as broad a comparison as possible to gain firm constraints on the assumed physics in our model. Therefore a multitude of observational properties was contrasted with the model predictions such as clustering, luminosity functions, stellar mass functions, number counts per area and redshift to a certain magnitude limit. In order to facilitate the comparison between simulations and recent intermediate and high-redshift surveys, it is very useful to have a number of independent mock observations of the simulated galaxies, which provide good enough statistics to get a handle on cosmic variance. To this end I have devised a computer program that calculates the simulated galaxies lying on the backward light cone of a hypothetical observer out to arbitrarily high redshifts, taking advantage of the periodicity of the simulation box but avoiding replications. The output provides accurately interpolated redshifts, positions, observer frame and rest-frame magnitudes, dust extinction, as well as all the intrinsic galaxy properties like stellar mass and star formation rate. Utilising this tool it is also possible to make predictions for future galaxy surveys, deeper in magnitude and redshift than current

## Summary

---

ones. Presently the mock catalogues are used by the DEEP2 and COSMOS teams as a comparison sample in general and as a means to assess their selection effects and improve their data reduction in particular. First comparisons of counts in apparent magnitude and redshift gave promising results, showing good agreement in the low and intermediate range. The same holds for the angular clustering analysis except for the faintest magnitudes. Thus we conclude that our current understanding of the processes governing galaxy formation and evolution from the very first objects to the present day population is realistic but still incomplete. In particular the treatment of the interplay between star formation and negative feedback and the various processes influencing satellite galaxies in big galaxy clusters have potential for improvement.

In the following I will give a brief outline of the thesis. After setting the stage for any kind of model in Chapter 1 by defining the geometry of the universe and the cosmological parameters that determine it, I will describe our semi-analytical model of galaxy formation in Chapter 2, where it will be also explained how to construct realistic mock observations of the simulated galaxies. First in Chapter 3 it will be verified that a simple model which assumes that galaxies are conserved but evolve in luminosity due to their star formation histories cannot account for the observed evolution of the galaxy population in the universe. This fact can be understood in the context of hierarchical models where massive and luminous galaxies assembled from smaller objects. Chapter 4 proceeds with exploring the predictions from the considerably more sophisticated semi-analytic model based on an N-body simulation of the hierarchical growth of dark matter structures. For this analysis a set of mock light-cones was constructed for direct comparison with the data which shows reasonably good agreement between model and observations at low redshift and for bright apparent magnitudes. These light-cones represent one of the largest samples of realistic mock observations currently available. They can be used for testing data analysis techniques usually applied to real observations on a well defined sample of artificial galaxies to verify how well the derivation of galaxy properties from the data works. In Chapter 5 we will demonstrate how one can measure the evolution of the galaxy merger rate from observing close projected galaxy pairs. Interestingly we find that the calibration needed for the conversion is significantly different from what has typically been assumed in previous studies. Additionally we will demonstrate that galaxy merger rates and dark-matter merger rates show considerably different evolution with redshift. Consequently we conclude that merger rate studies are less suitable as a probe of cosmic structure formation than initially assumed, but nonetheless they can be of great help to understand the formation and evolution of galaxies in a hierarchical universe.

Finally these results will be summarised and discussed in Chapter 6 where I will also give a brief outlook on the future of this work, a short glimpse of which is already presented in the Appendix.

*In the beginning the Universe was created. This has made a lot of people very angry and been widely regarded as a bad move.*

— The Hitchhiker’s Guide to the Galaxy

# 1

## Introduction

In this chapter the basic ideas of modern cosmology will be outlined briefly in order to set the stage for the introduction of the particular galaxy formation model that has been used in this work in the following chapter.

### 1.1. The Universe

Philosophically, the universe is simply everything that is, by definition. If one restricts oneself to the aspect that it is the container for all the objects we see around us, then according to the currently favoured paradigm it can be described mathematically as a four-dimensional manifold, where the three spatial dimensions and time are considered to be equivalent. This manifold is called space-time and its properties are given by Einstein’s field equations.

Starting from special relativity and the idea that the gravitational force is due to curved space-time, there are a number of different paths one can choose to arrive at the Einstein field equations. The hardest one was presumably taken by Einstein himself, since he had to break new grounds without any guidance, so he tried several things before he finally arrived at the correct solution. Shortly after Hilbert presented a more elegant derivation based on the action principle which states that the action defined as the integral over the Lagrangian density

$$S = \int d^4x \sqrt{-g} \left( \mathcal{L}_m - \frac{R}{16\pi G} \right) \quad (1.1)$$

## 1. Introduction

---

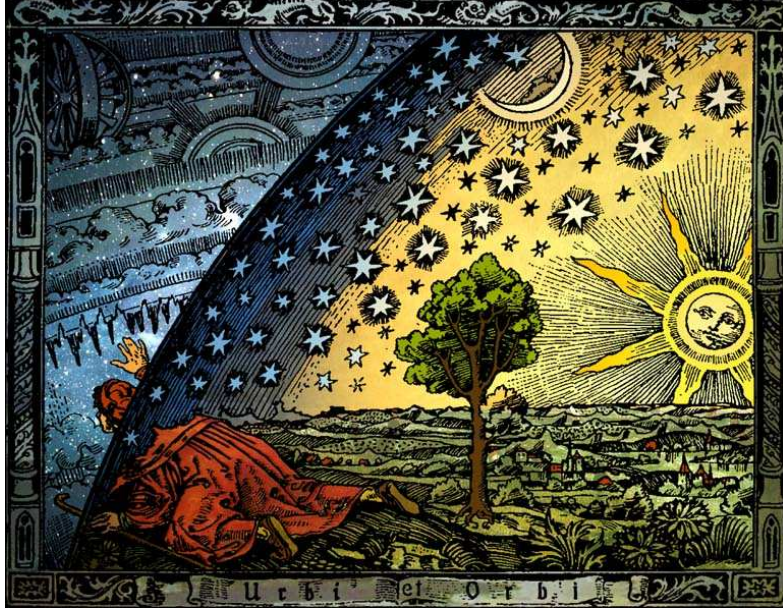


Figure 1.1.: Discovering the Universe (from “L’atmosphère: météorologie populaire” by Camille Flammarion, 1888).

has to be stationary, i.e.  $\delta S = 0$ . Going through all the math and adding  $\Lambda$  as a Lagrangian multiplier (in turn an addition from Einstein), the field equations come out as

$$R_{ij} - \frac{1}{2}g_{ij}R - \Lambda g_{ij} = 8\pi G T_{ij} \quad (1.2)$$

or

$$R_{ij} = 8\pi G(T_{ij} - \frac{1}{2}g_{ij}T) + \Lambda g_{ij} \quad (1.3)$$

due to their symmetry. On the left hand side is the geometry of space, expressed in terms of the Ricci tensor  $R_{ij}$  and scalar  $R$ ,  $g_{ij}$  is the metric, and  $T_{ij}$  is the energy momentum tensor whose covariant divergence has to be zero to satisfy energy and momentum conservation:

$$T^{ij}{}_{;j} = 0 \quad (1.4)$$

For an ideal fluid it can be written in terms of the 4-velocity  $u^i$ , density  $\rho$  and pressure  $p$

$$T^{ij} = (\rho + p)u^i u^j - g^{ij}p \quad (1.5)$$

In the non-relativistic case where only  $u^0$  is relevant, we get  $T^{00} = \rho$  and  $T^{11} = T^{22} = T^{33} = p$  for the diagonal elements.



Assuming the universe is homogeneous and isotropic, but not static, as first done by Friedmann, yields the Friedmann-Lemaître-Robertson-Walker (FLRW) metric with the corresponding line element (in a particular coordinate system) being

$$ds^2 = dt^2 - a(t)^2 \left[ \frac{dr^2}{1 \pm r^2/R^2} + r^2(d\theta^2 + \sin^2 \theta d\phi^2) \right], \quad (1.6)$$

where  $R$  is now the curvature radius and the  $\pm$  in the denominator can be either positive for open geometries or negative for a closed universe. The expansion parameter  $a(t)$  is a measure for the size of the universe and is  $a(t_0) \equiv a_0$  at the present.

Feeding this metric together with the energy momentum tensor into the Einstein field equation results in the Friedmann equations:

$$\frac{\ddot{a}}{a} = -\frac{4\pi G}{3}(\rho + 3p) + \frac{\Lambda}{3}, \quad (1.7)$$

and

$$\left(\frac{\dot{a}}{a}\right)^2 = \frac{8\pi G}{3}\rho + \frac{1}{a^2 R^2} + \frac{\Lambda}{3}. \quad (1.8)$$

which together with the definition

$$\left(\frac{\dot{a}}{a}\right)(t_0) \equiv H_0 \quad (1.9)$$

uniquely govern the evolution of the universe.

More generally we can define an effective  $\rho' = \sum \rho_w$  that includes several components, such as matter, radiation, cosmological constant or dark energy which evolve differently with redshift. To this end we introduce  $w$  as

$$p = w\rho_w, \quad (1.10)$$

which characterises the equation of state of a given component.

We can calculate  $w$  for different components if we know how the total energy  $u_w = \rho_w V$  dilutes with expansion, i.e.

$$w = -\frac{\log u_w}{\log V} = -\frac{\log \rho_w}{\log V} - 1 \quad (1.11)$$

where we have used  $du = -p dV$ . For ordinary matter  $u$  stays constant and  $\rho_M \sim V^{-1}$ , thus  $w = 0$ , for a cosmological constant  $\rho_\Lambda = \text{const}$  yielding  $w = -1$ , and finally for radiation  $\rho_\gamma \sim a^{-4}$  which together with  $a^3 \sim V$  leads to  $w = \frac{1}{3}$ .

Therefore we can write

$$\rho_w a^{3(1+w)} = \rho_{w,0} a_0^{3(1+w)}. \quad (1.12)$$

## 1. Introduction

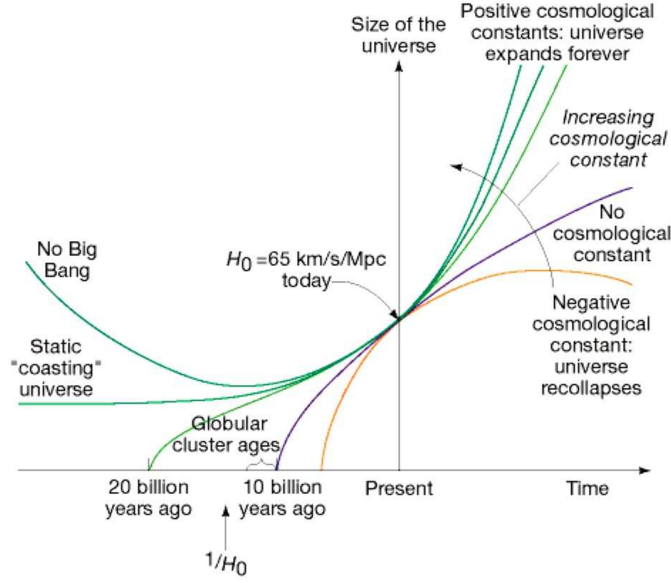


Figure 1.2.: The expansion of the universe with time for different cosmological parameters. Open universes expand forever, closed universes will collapse again at some point in the future.

Additionally we define the critical density for a closed universe

$$\rho_{\text{cr}} = \frac{3H_0^2}{8\pi G}, \quad (1.13)$$

and use it as a normalisation for the new quantity  $\Omega$

$$\Omega_{w,0} \equiv \frac{\rho_{w,0}}{\rho_{\text{cr}}}. \quad (1.14)$$

such that

$$\Omega_{m,0} = \frac{8\pi G\rho}{3H_0^2}, \quad \Omega_{\Lambda,0} = \frac{\Lambda}{3H_0^2} \quad (1.15)$$

then Eqn. 1.8 becomes

$$H^2(t) \equiv \left(\frac{\dot{a}}{a}\right)^2 = H_0^2 \left(\frac{a_0}{a}\right)^2 \left[ \sum_w \Omega_{w,0} \left(\frac{a_0}{a}\right)^{1+3w} + \Omega_R \right], \quad (1.16)$$

where we have summed over all components and used

$$\Omega_R = \frac{1}{H_0^2 a_0^2 R^2} = 1 - \sum_w \Omega_{w,0} \quad (1.17)$$

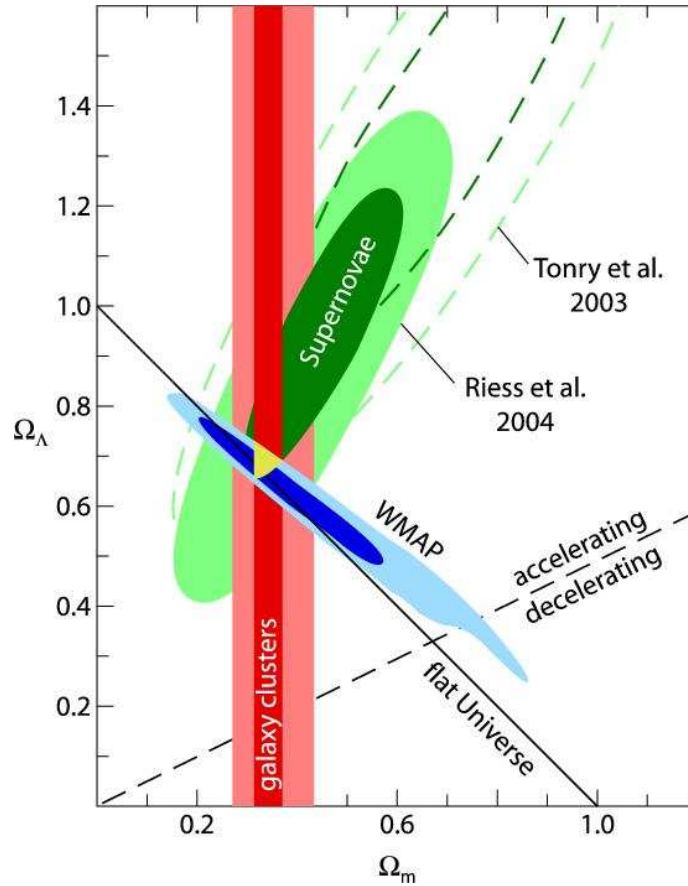


Figure 1.3.: Constraints on the cosmological parameters  $\Omega_m$  and  $\Omega_\Lambda$  from different observations yielding complementary results.

Radiation is diluting too fast to be relevant apart from the immediate aftermath of the Big Bang and thus we can restrict ourselves to considering only matter and  $\Lambda$  which inserted into Eqn. 1.16 yields

$$H^2(t) = H_0^2 \left[ \Omega_{m,0} \left( \frac{a_0}{a} \right)^3 + \Omega_R \left( \frac{a_0}{a} \right)^2 + \Omega_{\Lambda,0} \right], \quad (1.18)$$

## 1. Introduction

---

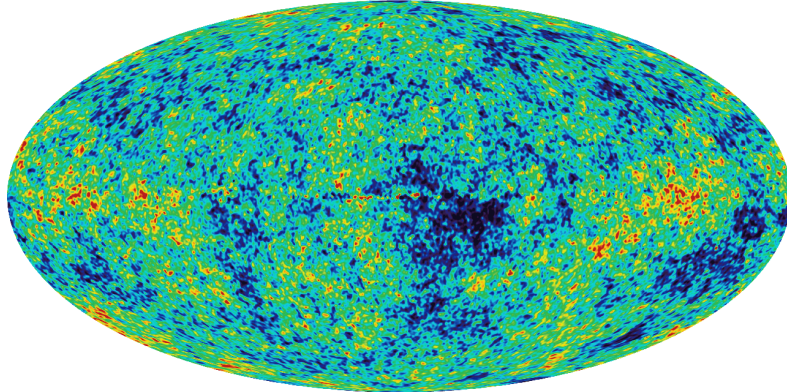


Figure 1.4.: An Aitoff projection of the temperature fluctuations in the CMB measured by the WMAP satellite. The monopole at a temperature of  $T=2.7$  K and the dipole from the peculiar motion of Earth have already been subtracted. In addition the region around the galactic equator where the signal is dominated by radiation from our Galaxy was masked out and reconstructed. This is the origin for the prominent features in this region which suggest a deviation from homogeneity and isotropy that is however not real. Another curiosity is the appearance of the initials “S.H.” above and to the left of the centre.

### 1.2. Linear growth of structure

The results in the previous section are for a completely homogeneous and isotropic universe, an assumption that is quite justified on scales larger than a few hundred Mpc, and thus good enough for the sake of calculating its overall geometry and evolution. However, such a universe would be rather boring and the existence of Earth, our solar system, and the Galaxy is sufficient proof that on smaller scales structure exists and thus homogeneity is not satisfied anymore.

In order to understand the origins of these structures, we can start out with the “plain” universe described above and study what happens to small relative density fluctuations that perturb the overall average density  $\rho_b$  which we model as

$$\delta(\mathbf{x}, t) = \frac{\rho(\mathbf{x}, t) - \rho_b}{\rho_b} \ll 1, \quad (1.19)$$

Such an assumption can be motivated by the existence of a relative density fluctuation in the cosmic microwave background (CMB). [Penzias & Wilson \(1965\)](#) discovered this ubiquitous background radiation with a spectrum corresponding to a black

## 1.2. Linear growth of structure

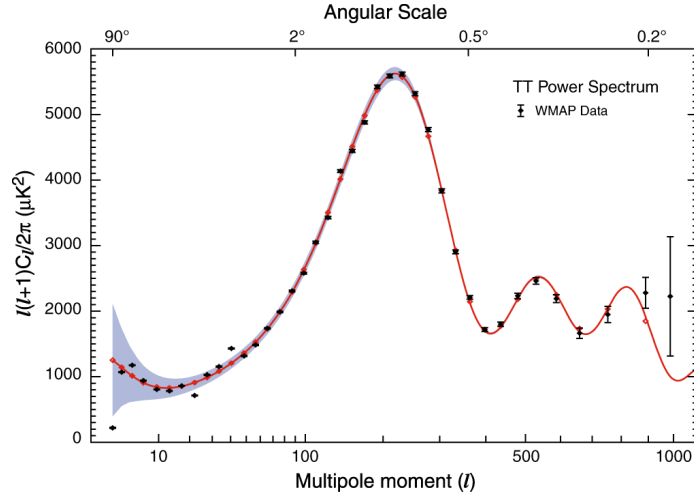


Figure 1.5.: The power spectrum of the CMB fluctuations measured by WMAP, where the x-axis denotes the multipoles of a spherical harmonics decomposition due to the spherical geometry of the sky. The first peak is called the acoustic peak and its position is a measure of the spatial curvature of the Universe. The other peaks can be used to derive the abundance of baryons at the time of recombination.

body of temperature 2.73 K by accident. It turned out to be the long looked after evidence that the universe was initially much smaller and hotter, since this radiation is the cooled off echo of the recombination of a hot plasma that must have once filled the universe. This implies that there has been an initial singularity from which everything came, the famous Big Bang. The relative temperature fluctuations in the CMB are of the order of only  $10^{-5}$  as measured by COBE and recently confirmed with unprecedented accuracy by the Wilkinson Microwave Anisotropy Probe (WMAP).

Peebles (1993) gives a very elegant derivation of the evolution of the density contrast with time simply based on the relation  $\rho a^3 = \text{const}$  which is true for non-relativistic ordinary matter where the pressure can be neglected compared to the mass density. Birkhoff's theorem states that different parts of the universe, here assumed to have slightly different matter density  $\rho$ , evolve as independent homogeneous universes. That is to say that where the universe has a density excess it will also expand more slowly, which can be parametrised as

$$\epsilon(\mathbf{x}, t) = \frac{a_b - a}{a_b} = -\frac{\delta\alpha}{a} \frac{\partial a}{\partial \alpha} \quad (1.20)$$

## 1. Introduction

---

where  $a = a(t, \alpha)$  and the change is due to a change in parameter  $\alpha$ .

It follows then that density excess and retarded expansion are connected by

$$\delta = 3\epsilon = -3 \frac{\delta\alpha}{a} \frac{\partial a}{\partial\alpha} \quad (1.21)$$

The expansion parameter depends on cosmology and cosmic time via Eqn. 1.8 which, with the definition

$$X \equiv \dot{a}^2 = \frac{8\pi G}{3} \rho_b a^2 + r^{-2} + \frac{1}{3} \Lambda a^2 \quad (1.22)$$

can be written in integral form as

$$t = \int^a \frac{da}{X^{1/2}} + C \quad (1.23)$$

Differentiating this equation with respect to  $R^{-2}$  yields

$$0 = \frac{1}{X^{1/2}} \frac{\partial a}{\partial(R^{-2})} - \frac{1}{2} \int^a \frac{da}{X^{3/2}} \quad (1.24)$$

which in combination with Eqn. 1.21 finally gives the solution<sup>1</sup> for the growth of the density contrast

$$\delta(t) = -\frac{3X^{1/2}\delta R^{-2}}{2a} \int^a \frac{da}{X^{3/2}}. \quad (1.25)$$

In an Einstein-de Sitter universe  $\Lambda = 0 = R^{-2}$  and thus  $X \propto a^{-1}$  resulting in

$$\delta(t) \propto a \propto t^{2/3} \quad (1.26)$$

There is a very important implication of this result, the initial density fluctuations we see in the CMB have only grown by a factor of  $a_0/a$  since the time of observation. This is not enough to explain everything that is around us, galaxies, and galaxy clusters in particular. The argument goes as follows: the redshift

$$z = \frac{\lambda_{\text{obs}} - \lambda_{\text{em}}}{\lambda_{\text{em}}} \quad (1.27)$$

---

<sup>1</sup>There is a second solution that derives from differentiating with respect to the integration constant but can usually be neglected since for any practical cosmology it decays with time.

## 1.2. Linear growth of structure

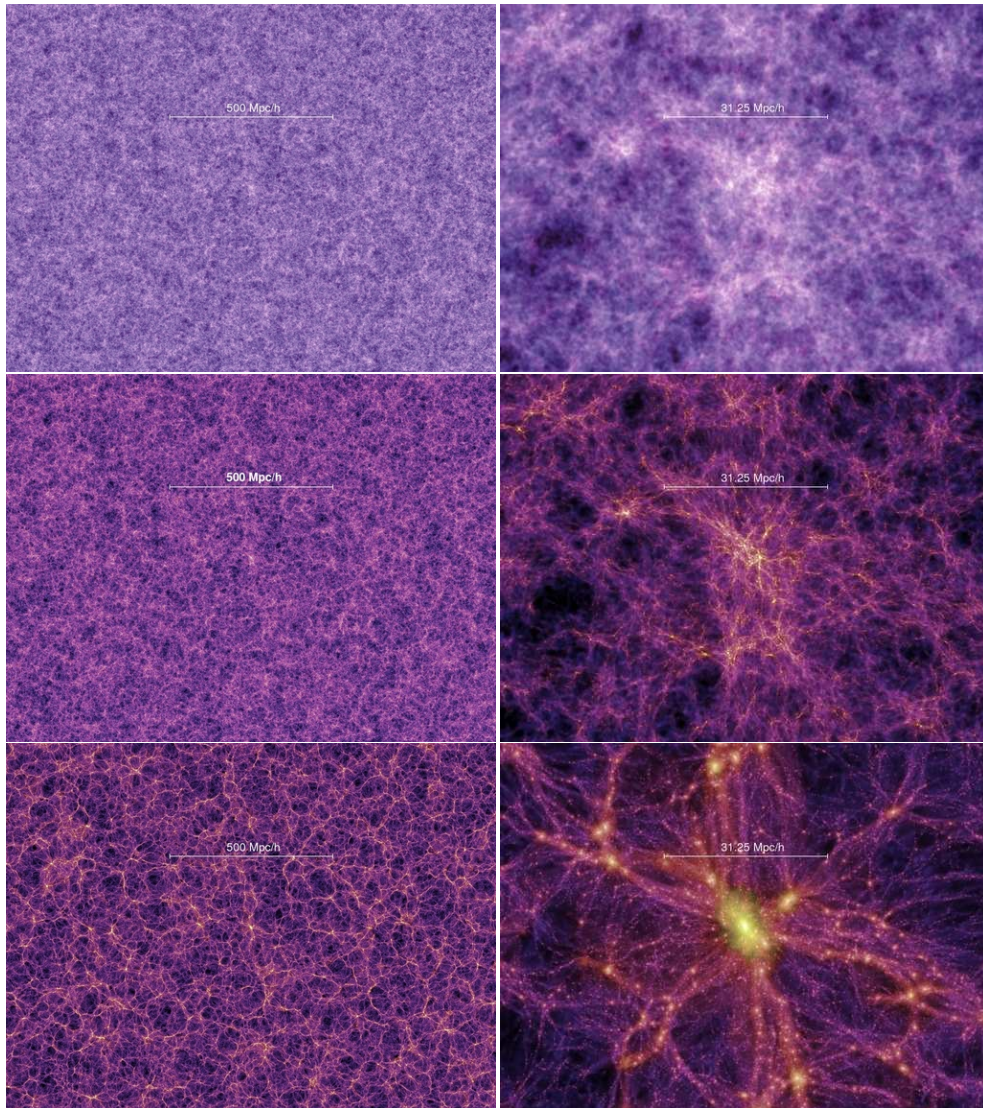


Figure 1.6.: Growth of structure in the Millennium run on large (left) and small (right) scales for redshifts  $z=[18, 6, 0]$  from top to bottom. (By courtesy of V. Springel)

of the CMB which has now a temperature of 2.73 K is about  $z = 1000$ , since at the time of recombination the universe must have been much hotter, of order of a few 1000 K. The expansion factor is connected to the redshift simply as  $1 + z = a^{-1}$

## 1. Introduction

---

and thus it follows that the initial CMB fluctuations of order  $10^{-5}$  would have grown only by a factor of 1000 to  $10^{-2}$  which would never have been enough to trigger a gravitational collapse that would result in dense enough gas to form stars<sup>2</sup>. This is one of the reasons why the matter density in the universe cannot be due to baryonic matter alone but there has to be an additional component that cannot be seen in the CMB and which must already at the time of recombination have had density fluctuations that were orders of magnitudes larger than the ones in the visible matter. Contrary to the original reason for the postulation for dark-matter, the flat rotation curves in galaxies, this argument does not allow the possibility of it being made of ordinary matter that would have heated up and “glown” in the CMB. Instead this has to be some yet unknown and unaccounted for form of matter.

This dark-matter also has to be “cold”, that is non-relativistic, as can be seen by deriving the growth of density fluctuations again, now in a more general case where pressure is taken into account. It would be beyond the scope of this thesis, to give the detailed derivation here, but it will be sketched briefly, how to arrive at the solution.

Apart from the spatial distribution of matter  $\rho$  also the velocity field has to be considered and together they have to satisfy the continuity equation.

$$\frac{\partial \rho}{\partial t} + \nabla(\rho \mathbf{v}) = 0. \quad (1.28)$$

Moreover the Euler equation governs how the change of velocity of a given mass parcel along its trajectory depends on the pressure and potential gradient

$$\frac{\partial \mathbf{v}}{\partial t} + (\mathbf{v} \cdot \nabla) \mathbf{v} + \frac{1}{\rho} \nabla p + \nabla \varphi = 0. \quad (1.29)$$

where the potential in turn is determined by the matter distribution via Poisson’s equation

$$\nabla^2 \varphi = 4\pi G \rho. \quad (1.30)$$

Now one has to first decouple the Hubble expansion by changing to comoving coordinates  $\mathbf{r} \rightarrow \mathbf{x} = \mathbf{r}/a$  and peculiar velocities  $\mathbf{v} \rightarrow \mathbf{u} = \mathbf{v} - H\mathbf{r}$ . Then after inserting into the above equations the non-perturbed terms will drop out since they have already been accounted for by the original derivation of the completely homogeneous universe and only terms for the density contrast and peculiar velocities remain. Due to the form of the equations it is then convenient to go into Fourier

---

<sup>2</sup>To be precise the  $10^{-5}$  is in temperature, not mass but for this order-of-magnitude consideration this doesn’t make a significant difference.



### 1.3. Formation of dark-matter haloes

---

space and express the evolution of  $\delta$  in terms of its modes  $\delta_k$  with wavenumber  $k$ . Finally by combining everything one arrives at:

$$\ddot{\delta}_k + 2\frac{\dot{a}}{a}\dot{\delta}_k + \delta_k \left( \frac{k^2 v_s^2}{a^2} - 4\pi G \rho_b \right) = 0. \quad (1.31)$$

where  $v_s^2 = \frac{\partial p}{\partial \rho}$  is the sound velocity. This equation has an oscillating solution if the term in brackets is positive and results in a monotonically growing mode if it is negative. Thus one can define a characteristic Jeans length

$$\lambda_J \simeq \frac{v_s}{\sqrt{G \rho_b}}, \quad (1.32)$$

above which the modes will grow and below which they will oscillate. Additionally it should be noted that the ‘‘damping’’ term is proportional to  $\dot{a}/a$ , i.e. larger for more rapid expansion. Now it is also clear why so called ‘‘hot’’ dark-matter (like neutrinos), with fast moving particles, is not favoured by current cosmological models since it would result in a very large Jeans length and hence not allow any small scale structures to grow. This would be a ‘‘top-down’’ scenario in which small objects form by fragmentation of big objects, in contradiction to the observed universe in which the ‘‘bottom-up’’ scenario of hierarchical growth of structure seems to have taken place, where first small objects formed and then merged in order to become bigger ones.

### 1.3. Formation of dark-matter haloes

The dark-matter component is considerably more abundant than ordinary matter and thus it dominates the growth of the total density fluctuations as the baryons fall into the dark matter potential wells. Since the initial density fluctuations in the dark-matter were larger than in the ordinary matter, the linear growth of structure as derived above will eventually lead to overdensities of the order unity, such that the assumption  $\delta \ll 1$  is not satisfied anymore. One can further study the gravitational collapse at this point by referring to Birkhoff’s theorem again. A region of the universe that has unity overdensity will behave like the whole universe would if it had twice its density. Hence we can make use of Eqn. 1.8 once more to follow the evolution of such a patch of space where we replace the expansion parameter  $a$  by the patch size  $R$  such that we get

$$\left( \frac{\dot{R}}{R} \right)^2 = \frac{8\pi G}{3} \rho. \quad (1.33)$$

## 1. Introduction

---

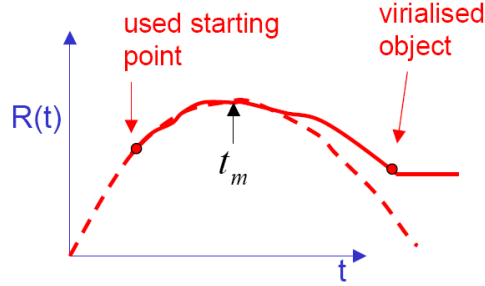


Figure 1.7.: Evolution of an overdense region of the universe according to the spherical collapse model.

Here we have assumed that the background universe is Einstein-de Sitter, i.e. it is flat and the cosmological constant  $\Lambda = 0$ . General solutions can be calculated in a similar way. The equation above has the solution

$$\frac{R}{R_m} = \frac{1}{2}(1 - \cos \eta) \quad (1.34)$$

$$\frac{t}{t_m} = \frac{1}{\pi}(\eta - \sin \eta) \quad (1.35)$$

which has the shape of a cycloid parametrised along the angle  $\eta$  (see Fig. 1.7). The extension becomes maximal at the “turn-around” point when  $R = R_m$ ,  $t = t_m$ , and this region of space decouples from the overall expansion of the universe. At time  $t = 2t_m$  the region has formally collapsed and  $R = 0$ . However, in reality a dynamically stable object of size  $R = R_m/2$  will form through virialisation. It can be shown that the overdensity at turn-over  $\rho_m/\rho_0 = 5.55$  and thus at the time of virialisation when it has collapsed to half the size it will be

$$\frac{\rho_{\text{vir}}}{\rho_0} = 5.55 \cdot 2^3 \cdot 2^2 = 177 \quad (1.36)$$

where the extra factor  $2^2 = t^2 = a^3$  stems from the ongoing expansion of the background universe during the collapse. This result is commonly simplified to  $\frac{\rho_{\text{vir}}}{\rho_0} \simeq 200$ , since it is not a rigorous derivation anyway and only valid for an Einstein-de Sitter universe.

## 1.4. Gas cooling and galaxy formation

---

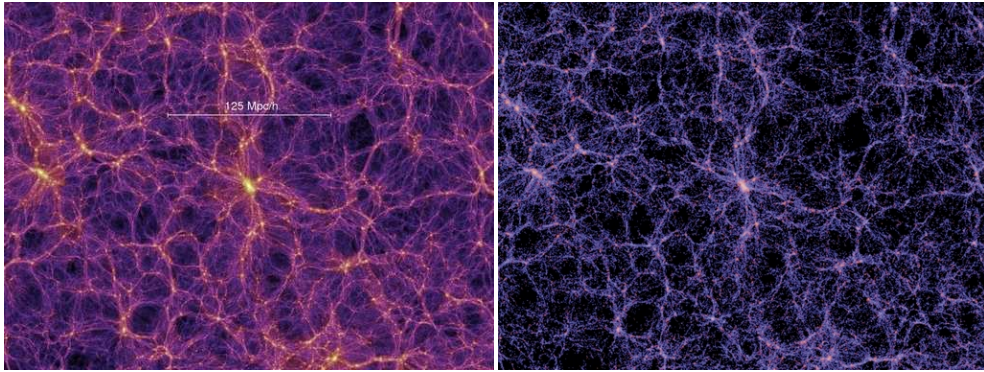


Figure 1.8.: The panel on the right illustrates how galaxies are distributed with respect to the dark-matter distribution in the Millennium run (left). Colours indicate actual galaxy colours, demonstrating the increased red galaxy fraction in the denser regions, which is one of the results of the model. (*By courtesy of V. Springel*)

### 1.4. Gas cooling and galaxy formation

After the dark matter has collapsed into such virialised objects, they start to attract baryonic gas which falls into their potential well and gets shock heated to the virial temperature. However baryons can radiate away energy and hence the hot gas cools on a certain timescale depending on its density and in the centre of the potential well this cooled gas will form a disk. This is already an object very similar to the gas disk in our own galaxy and analogously it will further fragment into clouds of molecular hydrogen that collapse and finally form stars. Planets too, presumably. Also black holes that are produced after the most massive stars die, which is very soon, because massive stars blaze away much more rapidly than small ones. These black holes collect in the very centre of the proto galaxy and merge with each other to form super-massive black holes which can be observed as quasars when they accrete gas.

So far the scenario would produce only isolated disk galaxies of different sizes. However, the dark matter objects, usually called haloes, with the galaxies in their centres merge with each other due to the hierarchical structure growth and so do their central objects. During this process the galaxy disks are destroyed and new cold gas is funnelled to the centre where it forms stars and feeds the black hole. The result of the process is a galaxy of more elliptical shape without a disk. This happens most frequently in very large dark matter haloes which correspond to observed clusters of galaxies. In their centres sit gigantic elliptical galaxies with extremely massive black holes. However these black holes prevent any more hot gas to cool onto the galaxy

## 1. Introduction

---

and hence it cannot form any more stars but keeps on growing through mergers with other massive galaxies that fall into the cluster.

In this chapter a qualitative description was given of the mechanisms shaping the universe as we observe it. A more quantitative treatment will be presented in the next chapter where the semi-analytic model of galaxy formation is explained.

*Far out in the uncharted backwaters of the unfashionable end of the western spiral arm of the Galaxy lies a small unregarded yellow sun. Orbiting this at a distance of roughly ninety-two million miles is an utterly insignificant little blue green planet whose ape-descended life forms are so amazingly primitive that they still think digital watches are a pretty neat idea.*

— The Hitchhiker’s Guide to the Galaxy

# 2

## The model

### 2.1. The Millennium Simulation

This thesis makes use of the Millennium Run, a very large N-body simulation which follows the hierarchical growth of dark matter structures from redshift  $z = 127$  to the present. The simulation assumes the concordance  $\Lambda$ CDM cosmology and follows the trajectories of  $2160^3 \simeq 1.0078 \times 10^{10}$  particles in a periodic box  $500 \text{ Mpc}/h$  on a side. A full description is given by [Springel et al. \(2005\)](#); the the main simulation characteristics are as follows:

The adopted cosmological parameter values are consistent with a combined analysis of the 2dFGRS ([Colless et al. 2001](#)) and the first-year WMAP data ([Spergel et al. 2003](#); [Seljak et al. 2005](#)). Specifically, the simulation takes  $\Omega_m = \Omega_{\text{dm}} + \Omega_b = 0.25$ ,  $\Omega_b = 0.045$ ,  $h = 0.73$ ,  $\Omega_\Lambda = 0.75$ ,  $n = 1$ , and  $\sigma_8 = 0.9$  where all parameters are defined in the standard way. The adopted particle number and simulation volume imply a particle mass of  $8.6 \times 10^8 h^{-1} M_\odot$ . This mass resolution is sufficient to resolve the haloes hosting galaxies as faint as  $0.1 L_*$  with at least  $\sim 100$  particles. The initial conditions at  $z = 127$  were created by displacing particles from a homogeneous, ‘glass-like’ distribution using a Gaussian random field with the  $\Lambda$ CDM linear power spectrum.

In order to perform such a large simulation on the available hardware, a special version of the GADGET-2 code ([Springel et al. 2001b](#); [Springel 2005](#)) was created with very low memory consumption. The computational algorithm combines a hierarchical multipole expansion, or ‘tree’ method ([Barnes & Hut 1986](#)), with a Fourier transform particle-mesh method ([Hockney & Eastwood 1981](#)). The short-range grav-

## 2. The model

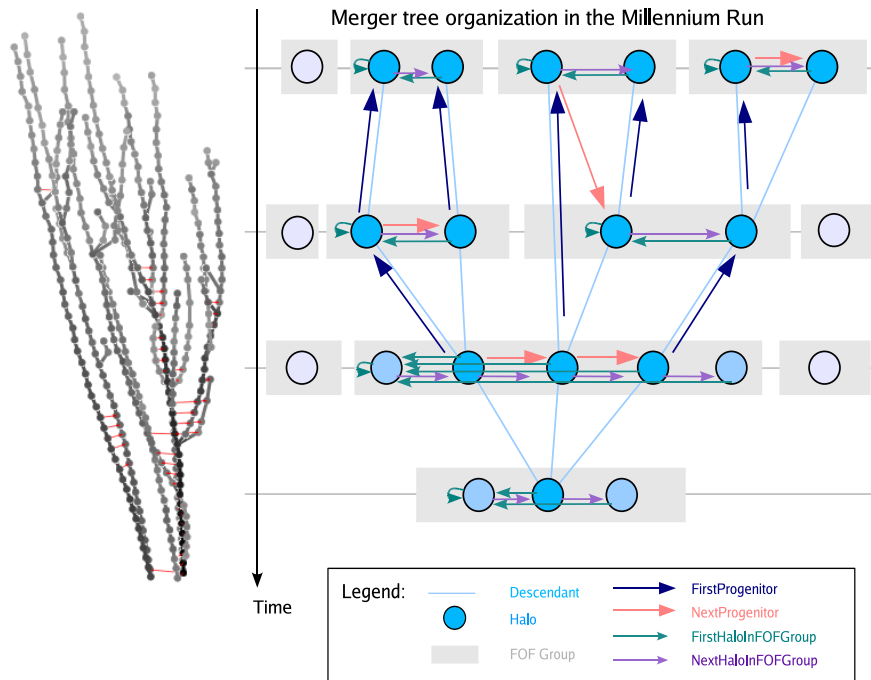


Figure 2.1.: The left panel shows a merger tree extracted from the simulation where the x-axis denotes actual spatial coordinates and the y-axis represents time. The more massive a halo is the darker its colour. Red lines indicate haloes being part of the same FOF object. A schematic view of a merger tree of dark matter haloes is shown on the right hand side. The Millennium Run produced many millions of such trees which were the basis for the subsequent semi-analytic modelling of baryon physics. (*By courtesy of V. Springel*)

itational force law is softened on comoving scale  $5 h^{-1} \text{kpc}$  which may be taken as the spatial resolution limit of the calculation, thus achieving a dynamic range of  $10^5$  in 3D. Data from the simulation were stored at 63 epochs spaced approximately logarithmically in time at early times and approximately linearly in time at late times (with  $\Delta t \sim 300 \text{Myr}$ ). Post-processing software identified all resolved dark haloes and their subhaloes in each of these outputs and then linked them together between neighbouring outputs to construct a detailed formation tree for every object present at the final time (see Fig. 2.1). Galaxy formation modelling is then carried out in post-processing on this stored data structure.

## 2.2. The semi-analytic model

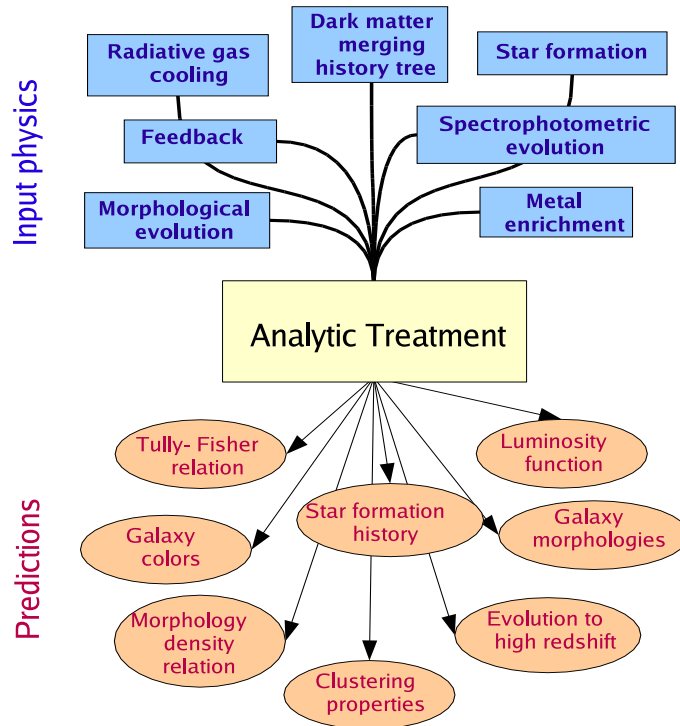


Figure 2.2.: A schematic representation of the semi-analytic recipes that are applied to model the evolution of baryons on top of the dark-matter merger trees. The lower part of the diagram gives some of the predictions that such a model can make. (By courtesy of V. Springel)

## 2.2. The semi-analytic model

The semi-analytic model applied here is that of [Croton et al. \(2006\)](#) as updated by [De Lucia & Blaizot \(2007\)](#) and [Kitzbichler & White \(2007\)](#). For the exact parameters used for all physical mechanisms incorporated in the model see Table 2.1 which is the updated version of Table 1 from [Croton et al. \(2006\)](#).

The following sections will give a very brief summary of the physical recipes incorporated in the model. A more comprehensive and more detailed description is given in [Croton et al. \(2006\)](#), who present a number of important predictions of the model in comparison to observations in the local universe.

## 2. The model

---

### 2.2.1. Gas infall and cooling

We adopt the standard paradigm set out by [White & Frenk \(1991\)](#) which was adapted for implementation on high resolution N-body simulations by [Springel et al. \(2001a\)](#) and [De Lucia et al. \(2004\)](#).

The cooling time of a gas is conventionally taken as the ratio of its specific thermal energy to the cooling rate per unit volume,

$$t_{\text{cool}} = \frac{3}{2} \frac{\bar{\mu} m_p k T}{\rho_g(r) \Lambda(T, Z)}. \quad (2.1)$$

Here  $\bar{\mu} m_p$  is the mean particle mass,  $k$  is the Boltzmann constant,  $\rho_g(r)$  is the hot gas density, and  $\Lambda(T, Z)$  is the cooling function. Furthermore we assume that the hot gas within a static atmosphere has a simple ‘isothermal’ distribution,

$$\rho_g(r) = \frac{m_{\text{hot}}}{4\pi R_{\text{vir}} r^2}, \quad (2.2)$$

where  $m_{\text{hot}}$  is the total hot gas mass associated with the halo and is assumed to extend to its virial radius  $R_{\text{vir}}$ .

Simply applying the continuity equation, and making use of Eqn. 2.2 to express it in terms of  $m_{\text{hot}}$ , we get the cooling rate as,

$$\dot{m}_{\text{cool}} = 4\pi \rho_g(r_{\text{cool}}) r_{\text{cool}}^2 \dot{r}_{\text{cool}} = \frac{m_{\text{hot}}}{R_{\text{vir}}} \dot{r}_{\text{cool}}. \quad (2.3)$$

Combining Eqn. 2.1 and Eqn. 2.2 gives us the relation  $r_{\text{cool}} \sim t_{\text{cool}}^{1/2}$  which we can differentiate logarithmically to get,

$$\dot{r}_{\text{cool}} = \frac{1}{2} \frac{r_{\text{cool}}}{t_{\text{cool}}} = \frac{1}{2} r_{\text{cool}} \frac{V_{\text{vir}}}{R_{\text{vir}}}. \quad (2.4)$$

Where we have assumed the cooling time to be equal to the dynamical time  $t_{\text{cool}} = t_{\text{dyn}} = R_{\text{vir}}/V_{\text{vir}}$ . This quantity shows a dependence on redshift  $R_{\text{vir}}/V_{\text{vir}} = 0.1 H(z)^{-1}$  given our definition of the virial quantities of a halo with a density 200 times the critical value  $3H^2/8\pi G$ ,

$$M_{\text{vir}} = \frac{100}{G} H^2(z) R_{\text{vir}}^3 = \frac{V_{\text{vir}}^3}{10 G H(z)}. \quad (2.5)$$

Thus we finally get an expression for the cooling rate in a static hot gas halo as,

$$\dot{m}_{\text{cool}} = 0.5 m_{\text{hot}} \frac{r_{\text{cool}} V_{\text{vir}}}{R_{\text{vir}}^2}. \quad (2.6)$$



## 2.2. The semi-analytic model

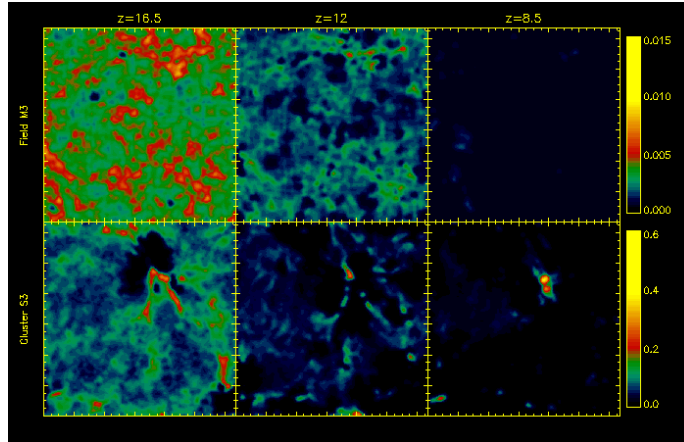


Figure 2.3.: Simulation of the reionisation of the Universe by the first stars (Ciardi et al. 2003).

This is for what we call the *hot halo regime*. However, if the nominal cooling radius would exceed the virial radius  $r_{\text{cool}} > R_{\text{vir}}$  then the halo is in the *rapid cooling regime* and we assume that the cooling rate is equal to the accretion rate of new diffuse gas onto the halo.

### 2.2.2. Reionisation

In order to reflect the decreased efficiency of gas accretion and cooling in low-mass haloes due to photoionisation at early times we follow the approach of Gnedin (2000) and introduce an effective baryon fraction which is a function of halo mass as

$$f_{\text{b}}^{\text{halo}}(z, M_{\text{vir}}) = \frac{f_{\text{b}}^{\text{cosmic}}}{(1 + 0.26 M_{\text{F}}(z)/M_{\text{vir}})^3}, \quad (2.7)$$

where  $M_{\text{F}}$  is a characteristic filtering mass below which the gas fraction  $f_{\text{b}}$  is reduced relative to the universal value.

### 2.2.3. Star formation

In our model all star formation occurs in cold disc gas, either quiescently or in a burst. We adopt a threshold surface density for the cold gas above which gas starts to collapse and form stars, and following Kauffmann (1996) approximate it by

## 2. The model

---

$$\Sigma_{\text{crit}}(R) = 120 \left( \frac{V_{\text{vir}}}{200 \text{ km s}^{-1}} \right) \left( \frac{R}{\text{kpc}} \right)^{-1} M_{\odot} \text{pc}^{-2}. \quad (2.8)$$

Under the assumption that the gas is evenly distributed over the disk we can convert this into a critical cold gas mass

$$m_{\text{crit}} = 3.8 \times 10^9 \left( \frac{V_{\text{vir}}}{200 \text{ km s}^{-1}} \right) \left( \frac{r_{\text{disk}}}{10 \text{ kpc}} \right) M_{\odot}, \quad (2.9)$$

where we assume the outer disk radius to be  $r_{\text{disk}} = 3r_s$  with  $r_s = \lambda/\sqrt{2} R_{\text{vir}}$  (Mo et al. 1998). Hence we can write the star formation rate as

$$\dot{m}_* = \alpha_{\text{SF}} (m_{\text{cold}} - m_{\text{crit}}) / t_{\text{dyn,disk}}, \quad (2.10)$$

where we take the dynamical time of the disc to be  $t_{\text{dyn,disk}} = r_{\text{disk}}/V_{\text{vir}}$  and assume a star formation efficiency  $\alpha_{\text{SF}}$  with which gas is converted into stars.

### 2.2.4. Supernova feedback

Shortly after the onset of star formation supernovae will start to go off and inject gas, metals and energy into the surrounding medium, reheating cold disk gas and even ejecting some gas from the halo. Since star formation and supernova activity come together one can relate the amount of reheated gas to the mass of newly formed stars as

$$\Delta m_{\text{reheated}} = \epsilon_{\text{disk}} \Delta m_*, \quad (2.11)$$

where we follow Martin (1999) and assume some proportionality factor  $\epsilon_{\text{disk}}$ . The reheating energy from supernovae that come along with a mass  $\Delta m_*$  of newly formed stars can be written

$$\Delta E_{\text{SN}} = 0.5 \epsilon_{\text{halo}} \Delta m_* V_{\text{SN}}^2, \quad (2.12)$$

where  $0.5 V_{\text{SN}}^2$  is the mean energy of the supernova ejecta per unit mass and  $\epsilon_{\text{halo}}$  is the reheating efficiency. Adding the reheated mass to the hot halo will increase its energy by

$$\Delta E_{\text{hot}} = 0.5 \Delta m_{\text{reheated}} V_{\text{vir}}^2. \quad (2.13)$$

Thus the *excess* energy after reheating is  $\Delta E_{\text{excess}} = \Delta E_{\text{SN}} - \Delta E_{\text{hot}}$ . This energy is available to eject gas from the halo into an external ‘reservoir’. Distributing it evenly on the hot gas mass we get

$$\Delta m_{\text{ejected}} = \frac{\Delta E_{\text{excess}}}{E_{\text{hot}}} m_{\text{hot}} = \left( \epsilon_{\text{halo}} \frac{V_{\text{SN}}^2}{V_{\text{vir}}^2} - \epsilon_{\text{disk}} \right) \Delta m_*, \quad (2.14)$$

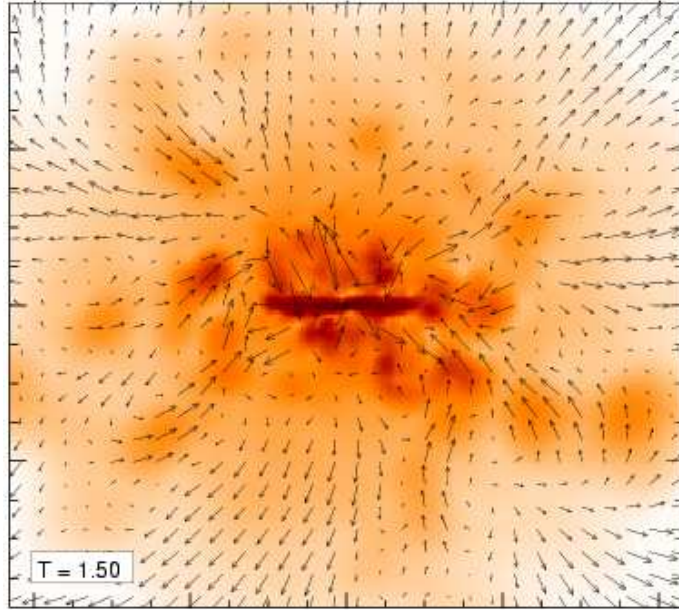


Figure 2.4.: Simulation of supernova driven winds streaming from a galaxy (Springel & Hernquist 2003).

where  $E_{\text{hot}} = 0.5 m_{\text{hot}} V_{\text{vir}}^2$  is the total thermal energy in the hot halo. This particular parametrisation has two consequences, firstly it is possible for small  $V_{\text{vir}}^2$  that the entire hot gas is ejected, i.e.  $m_{\text{ejected}}$  saturates at  $m_{\text{reheated}}$ . Secondly no gas can be ejected for massive haloes with  $V_{\text{vir}}^2 > \epsilon_{\text{halo}}/\epsilon_{\text{disk}} V_{\text{SN}}^2$ . We follow De Lucia et al. (2004) and assume that the ejected gas can fall back onto the halo and be reincorporated into the cooling cycle

$$\dot{m}_{\text{ejected}} = -\gamma_{\text{ej}} m_{\text{ejected}} / t_{\text{dyn}}, \quad (2.15)$$

on a certain timescale that is proportional to the dynamical time and controlled by the parameter  $\gamma_{\text{ej}}$ .

### 2.2.5. Black hole growth, AGN outflows, and cooling suppression

In our model black holes grow in two modes, the first one being the merging and gas accretion of BHs during mergers, which we call the ‘quasar mode’ and which is the dominant mode of growth. It is closely based on Kauffmann & Haehnelt (2000)

## 2. The model

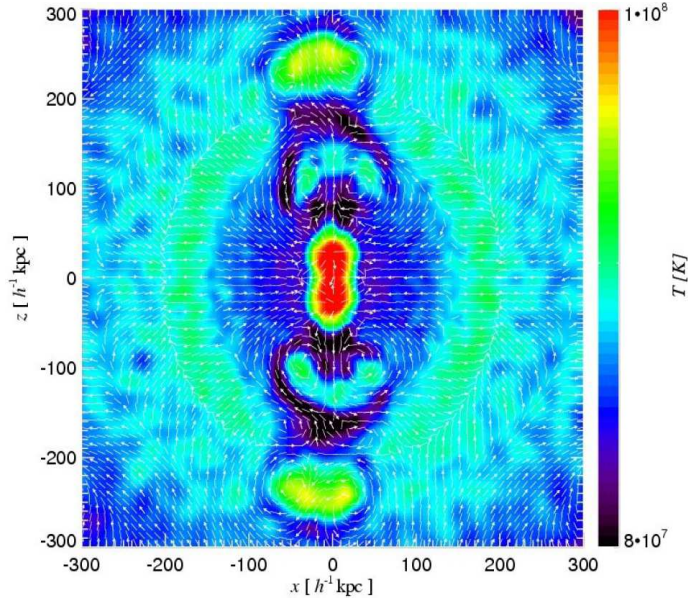


Figure 2.5.: Simulation of bubbles of hot gas produced by an AGN in “radio mode”, accreting only weakly (Sijacki & Springel 2006). The bubbles are rising buoyantly in the surrounding medium in the galaxy cluster and dissipate energy which prevents the cooling of hot gas.

where the assumed BH accretion is proportional to the cold gas mass present and has lower efficiency for lower mass haloes:

$$\Delta m_{\text{BH,Q}} = \frac{f'_{\text{BH}} m_{\text{cold}}}{1 + (280 \text{ km s}^{-1}/V_{\text{vir}})^2}. \quad (2.16)$$

We adopt this model with the modification that we consider not only major mergers but also minor mergers and change the original parametrisation to reflect this fact by making the efficiency parameter dependent on the mass ratio of the merger progenitors,

$$f'_{\text{BH}} = f_{\text{BH}} (m_{\text{sat}}/m_{\text{central}}). \quad (2.17)$$

The second mode of BH growth is assumed to be much more quiescent accretion of gas from the static hot halo of a galaxy onto its supermassive black hole. Since this is giving rise to a low energy ‘radio’ activity of this galaxy we call this mode the ‘radio mode’ and model it with a simple phenomenological model:

## 2.2. The semi-analytic model

$$\dot{m}_{\text{BH,R}} = \kappa_{\text{AGN}} \left( \frac{m_{\text{BH}}}{10^8 M_{\odot}} \right) \left( \frac{f_{\text{hot}}}{0.1} \right) \left( \frac{V_{\text{vir}}}{200 \text{ km s}^{-1}} \right)^3, \quad (2.18)$$

where  $\kappa_{\text{AGN}}$  determines the efficiency of accretion in  $M_{\odot}/\text{yr}$  and  $f_{\text{hot}}$  is the fraction of the total halo mass in the form of hot gas. The radio mode contributes on average at least an order of magnitude less than the quasar mode to the mass increase of the BH at all redshifts. However the mechanical energy it injects into the surrounding medium assumed to be (with standard BH accretion efficiency  $\eta = 0.1$ )

$$L_{\text{BH}} = \eta \dot{m}_{\text{BH}} c^2, \quad (2.19)$$

will partly compensate the radiative losses of the hot gas and thus modify the cooling rate to become

$$\dot{m}'_{\text{cool}} = \dot{m}_{\text{cool}} - \frac{L_{\text{BH}}}{\frac{1}{2} V_{\text{vir}}^2}. \quad (2.20)$$

It is interesting to note that this modification will prevent gas cooling and as a consequence star formation if the ratio

$$\frac{\dot{m}_{\text{heat}}}{\dot{m}_{\text{cool}}} \propto \frac{m_{\text{BH}}}{V_{\text{vir}}} \left( \frac{t_{\text{H}}}{f_{\text{hot}} \Lambda(V_{\text{vir}})} \right)^{1/2} \quad (2.21)$$

is larger than unity. This means that cooling prevention will be more important at later times and in galaxies with more massive black holes.

### 2.2.6. The importance of feedback

Fig. 2.6 demonstrates how important it is to incorporate all the relevant physics in the model. On the left it shows the  $B$ -band luminosity function from the full model and on the right as it would result if no reionisation and neither supernova nor AGN feedback would be taken into account. In this case there would be a very simple relation between the dark matter halo mass and the stellar mass of the galaxy and hence the LF comes out almost identical to the mass function of dark matter haloes.

The preheating of gas by reionisation prevents efficient cooling in low mass objects. It is responsible for the much flatter slope on the faint end of the LF, together with the supernova feedback which ejects cold gas from galaxies that have a low escape velocity. Both these feedback mechanisms are only little effective for massive objects where the much deeper potential well keeps the gas bound. Even though one could imagine a very strong supernova feedback, sometimes called “super-winds”, that could still eject gas and make it unavailable for star formation, this would only

## 2. The model

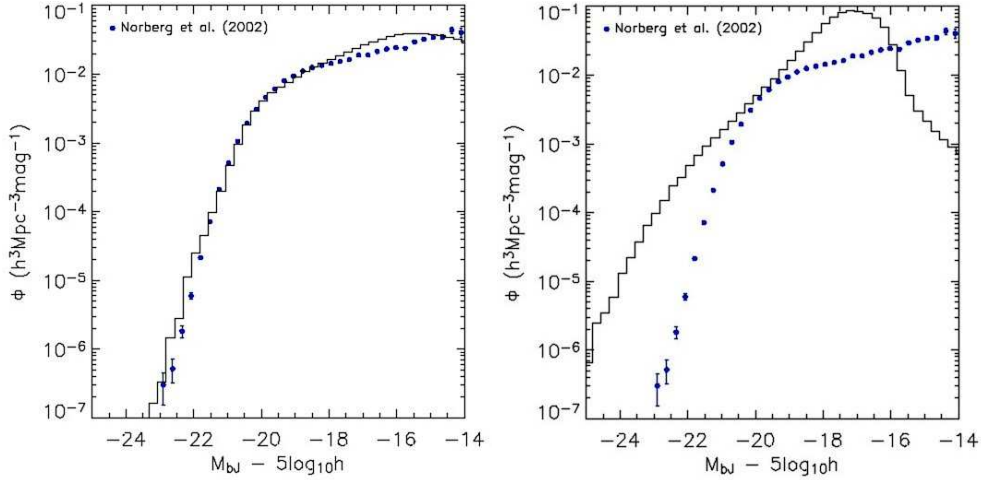


Figure 2.6.: The local  $B$ -band luminosity function compared to the model prediction from the full model (left) and from a simple model (right) where only cooling and star formation have been calculated, but no preheating through reionisation and no feedback.

be temporary since eventually it would come back and result in an even stronger burst of star formation. The only solution to the problem is thus a continuous prevention of gas cooling that doesn't depend on star formation, because such is not observed and it would result in further growth of stellar mass. The “radio mode” of AGN feedback provides such a mechanism since it requires only minimal amounts of gas being fed to the central black hole and has a very high mechanical efficiency in dissipating the energy output of the black hole into the surrounding intercluster medium.

How this feedback mechanism affects the gas in galaxies is illustrated in Fig. 2.7, which shows the evolution of the cold gas fraction with redshift as a function of stellar mass. At early times there is plenty of gas to fuel star formation over a large mass range, even though more massive galaxies contain also a larger fraction of baryons in stars. Conversely at low redshift most of the baryons are in massive objects where they have been converted into stars, and there is no more cold gas becoming available. The transition between the gas rich and the gas poor era is roughly taking place at  $z \sim 1$ , and the mass threshold above which there is absolutely no cold gas is  $M_* \sim 3 \cdot 10^{11} M_\odot/h$ .

Abundance of cold gas results in high star formation rates whereas lack of it quenches star formation immediately. These effects of the change in gas fraction can be seen in Fig. 2.8 where the evolution of the specific star formation rate (SSFR)

## 2.2. The semi-analytic model

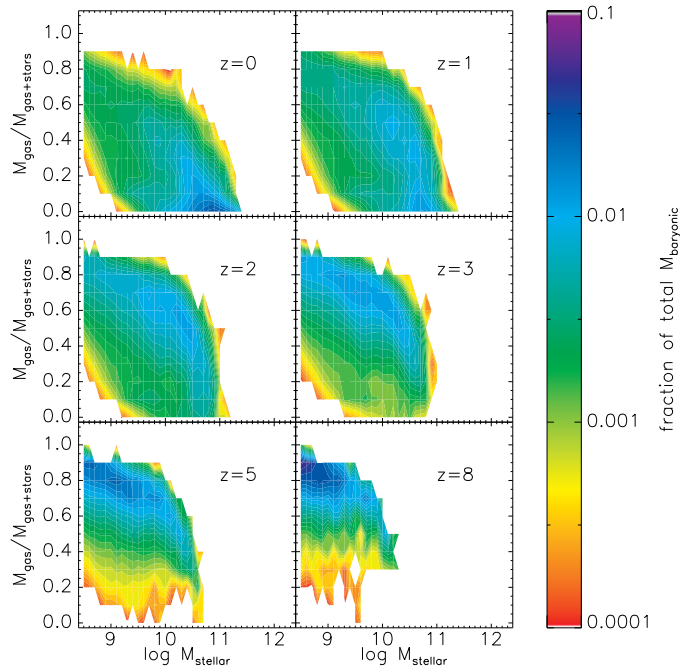


Figure 2.7.: Evolution with redshift of the cold gas fraction in galaxies as a function of stellar mass. Colours denote the fraction of total baryonic mass per bin.

with redshift is plotted in the stellar mass versus virial mass plane. At early times there is a steep increase of stellar mass with  $M_{\text{vir}}$  and the SSFR is high for all masses whereas at lower redshifts the SSFR is lower overall and there exists a threshold mass of  $M_{\text{vir}} \sim 3 \cdot 10^{12} M_{\odot}/h$  above which the SSFR drops to almost zero. This results in the side-effect that the  $M_* - M_{\text{vir}}$  relation has a break at that mass as well since those galaxies can gain more stellar mass only by merging and not by star formation anymore.

### 2.2.7. Dust treatment

A crucial ingredient especially for filter bands at short wavelengths is the dust model. For the present-day LF a simple phenomenological treatment based on the UV or  $B$ -band luminosity gave satisfactory results (Kauffmann et al. 1999). It assumes a power law for the face-on optical depth  $\tau \propto \tau_0 (L/L_*)^\beta$  where  $\beta \sim 0.5$  was calibrated from observations in the local universe and  $\tau_0$  is the extinction at the knee

## 2. The model

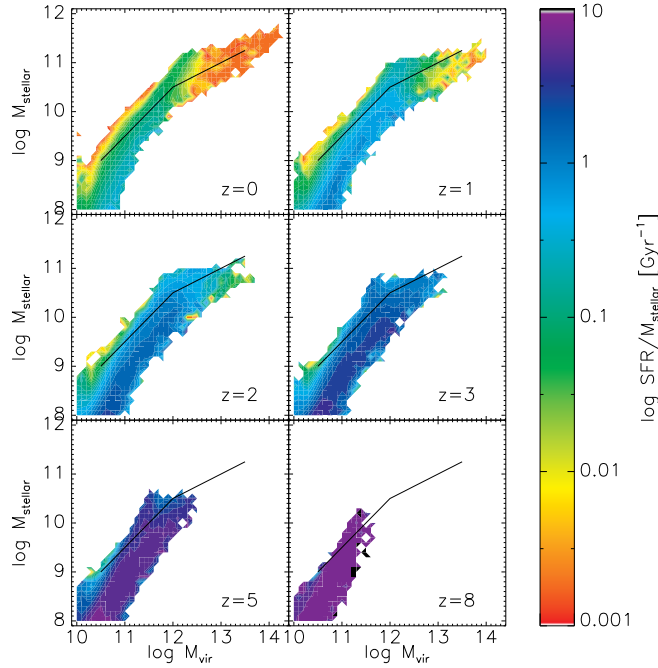


Figure 2.8.: Evolution with redshift of the specific star formation rate of galaxies plotted in the stellar mass versus virial mass plane. Colours denote average specific star formation rate per bin. The black lines have a slope of 1 and 1/2 respectively to guide the eye.

of the luminosity function.

However in order to calculate the high redshift dust attenuation in rest-frame and especially in observer frame correctly, we had to adopt a new approach. Dust in galaxies tends to be intermixed with the neutral hydrogen in the galactic disk, since that is where it is produced by the ongoing quiescent star formation, as can be seen in Fig. 2.9. Motivated by this fact [Devriendt et al. \(1999\)](#) have suggested a dust model that is based on the column density of HI in the galaxy disk. This quantity can be inferred from the cold gas mass and the disk size of a galaxy which are both available for each galaxy in the semi-analytic model. Furthermore the scaling of dust extinction with metallicity can easily be incorporated using the amount of metals given by the star formation model (cf. [Devriendt & Guiderdoni 2000](#)). Thus we get

$$\tau_{\lambda}^Z = \left( \frac{A}{A_V} \right)_{Z_{\odot}} \eta_Z \left( \frac{\langle N_H \rangle}{2.1 \times 10^{21} \text{ cm}^{-2}} \right) \quad (2.22)$$



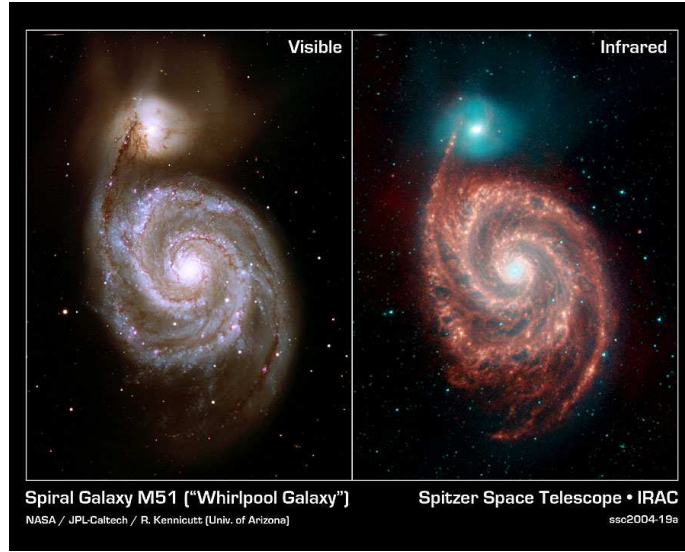


Figure 2.9.: Image of the galaxy M 51, which has an almost exact face on orientation with respect to earth. On the left an HST observation in the optical is shown, where the dark dust lanes are clearly visible against the stellar disk. The right picture was taken by the Spitzer telescope in infrared bands, where dust is not dark anymore but radiating away the energy it has absorbed as thermal emission.

with the average hydrogen column density

$$\langle N_H \rangle = \frac{M_{\text{gas}}}{1.4 \mu m_p \pi r_t^2}, \quad (2.23)$$

and  $A/A_V$  is the extinction curve from [Cardelli et al. \(1989\)](#). For the dust-to-gas ratio we assume  $\eta_Z = (1+z)^{-\frac{1}{2}} (Z_{\text{gas}}/Z_{\odot})^s$ , where  $s = 1.35$  for  $\lambda < 2000 \text{ \AA}$  and  $s = 1.6$  for  $\lambda > 2000 \text{ \AA}$ . The additional factor of  $(1+z)^{-\frac{1}{2}}$  for the dust-to-metallicity ratio calibrates the extinction law such that we get the correct results for LBGs at  $z \sim 3$ , ie.  $\langle \tau \rangle_{1600} \lesssim 2$  at rest-frame  $1600 \text{ \AA}$  taken from [Adelberger & Steidel \(2000\)](#), who find that dust obscuration at higher redshift is lower compared to the local universe for objects of the same  $L_{\text{bol}}$  (a result echoed in [Reddy et al. 2006](#)). Moreover, such a behaviour is in agreement with recent studies on the dust-to-gas/dust-to-metallicity ratio by e.g. [Inoue \(2003\)](#). Please note that the average extinction is still increasing strongly with redshift, firstly due to the ever shorter observer-frame bands we probe and secondly due to the inversely proportional scaling of disk sizes with redshift which enters squared in Eqn. 2.22 above.

## 2. The model

---

This is a sufficiently good model for most quiescently star forming galaxies. However, one has to model the dust extinction of very young stellar populations differently, since if a major star burst occurs, most of the light will come from new born massive OB associations, which are still enshrouded within their birth clouds. Thus we follow [De Lucia & Blaizot \(2007\)](#) who implemented a simple model to take into account the much stronger attenuation of young stars within these clouds, based on [Charlot & Fall \(2000\)](#). Stars younger than the finite lifetime of stellar birth clouds (assumed to be 20 Myr/h) are subject to a different attenuation with mean face-on optical depth:

$$\tau_{\lambda}^{\text{burst}} = \tau_{\text{V}}^{\text{burst}} \left( \frac{\lambda}{5500\text{\AA}} \right)^{-0.7}$$

and

$$\tau_{\text{V}}^{\text{burst}} = \tau_{\lambda}^{\text{Z}} \times \left( \frac{1}{\mu} - 1 \right),$$

where  $\mu$  is drawn randomly from a Gaussian distribution with centre 0.3 and width 0.2, truncated at 0.1 and 1 (see [Kong et al. 2004](#)).

Finally, one must also take into account the inclination of the galaxy to the line-of-sight when making an extinction correction.

For a thin disc where dust and stars are uniformly mixed, commonly called slab geometry, the total extinction in magnitudes is

$$A_{\lambda}^{\text{Z}} = -2.5 \log \left( \frac{1 - e^{-\tau_{\lambda}^{\text{Z}} \sec \theta}}{\tau_{\lambda}^{\text{Z}} \sec \theta} \right) \quad (2.24)$$

The inclination angle  $\theta$  we draw from a random distribution which is flat in  $\cos \theta$ , and we account for the fact that for very large inclination angles the above equation would lead infinite extinction whereas in reality one observes only a thin band of dust in such edge on galaxies. Therefore we limit the extinction not to exceed the universal value  $e^{-\tau_{\lambda}^{\text{Z}}}$ .

Table 2.1.: A summary of our fiducial semi-analytic model parameters, and plausible ranges.

parameter	description	best value	plausible range
$f_b$	cosmic baryon fraction	0.17	fixed
$z_0, z_r$	redshift of reionisation	8, 7	fixed
$f_{\text{BH}}$	merger cold gas BH accretion fraction	0.03	0.02 – 0.04
$\kappa_{\text{AGN}}$	quiescent hot gas BH accretion rate ( $M_{\odot}\text{yr}^{-1}$ )	$7.5 \times 10^{-6}$	$(4 - 8) \times 10^{-6}$
$\alpha_{\text{SF}}$	star formation efficiency	0.03	0.03 – 0.15
$\epsilon_{\text{disk}}$	SN feedback disk reheating efficiency	3.5	1 – 5
$\epsilon_{\text{halo}}$	SN feedback halo ejection efficiency	0.35	0.1 – 0.5
$\gamma_{\text{ej}}$	ejected gas reincorporation efficiency	0.5	0.1 – 1.0
$T_{\text{merger}}$	major merger mass ratio threshold	0.3	0.2 – 0.4
$R$	instantaneous recycled fraction of SF to the cold disk	0.3	0.2 – 0.4
$Y$	yield of metals produced per unit SF	0.03	0.02 – 0.04

## 2. The model

---

### 2.3. Lightcones

One can make mock observations of the artificial universe, constructed from the Millennium Simulation, by positioning a virtual observer at zero redshift and finding those galaxies which lie on his backward light cone. The backward light cone is defined as the set of all light-like worldlines intersecting the position of the observer at redshift zero. It is thus a three-dimensional hypersurface in four-dimensional space-time satisfying the condition that light emitted from every point is received by the observer now. Its space-like projection is the volume within the observer's current particle horizon. From this sphere, which would correspond to an all-sky observation, we cut out a wedge defined by the assumed field-of-view of our mock observation. It is common practice to use the term *light cone* for this wedge rather than for the full (all-sky) light cone, and we will follow this terminology here.

Chapter 4 contains an extensive description of the techniques used to construct lightcones from the Millennium simulation. Therefore we will restrict ourselves here to addressing only some fundamental issues of the topic.

#### 2.3.1. Spatial replication

The Millennium Simulation was carried out in a cubic region of side 500 Mpc/h whereas the comoving distance along the past light cone to redshift 1 is 2390 Mpc/h and to redshift 6 is 6130 Mpc/h. Thus deep light cones must use the underlying periodicity and traverse the fundamental simulation volume a number of times. Care is needed to minimise multiple appearances of individual objects, and to ensure that when they do occur they are at widely different redshifts and are at different positions on the virtual sky.

Taking into account these considerations we select the central angular coordinates  $\alpha_c$  and  $\beta_c$  of our line-of-sight which can then be written as a unit vector  $\mathbf{N}$  defining the tangential plane on the sky on which the cone will be projected. The local coordinate vectors along  $\alpha$  and  $\beta$  constitute the projection vectors  $\mathbf{p}_1$  and  $\mathbf{p}_2$  in this plane such that we get a well defined orthonormal coordinate basis

$$\begin{aligned}\mathbf{N}(\alpha_c, \beta_c) &= (\cos \beta_c \sin \alpha_c, \sin \beta_c, \cos \beta_c \cos \alpha_c) \\ \mathbf{p}_1(\alpha_c, \beta_c) &= \frac{1}{\cos \beta_c} \frac{\partial \mathbf{N}(\alpha_c, \beta_c)}{\partial \alpha_c} \\ \mathbf{p}_2(\alpha_c, \beta_c) &= \frac{\partial \mathbf{N}(\alpha_c, \beta_c)}{\partial \beta_c}\end{aligned}$$

which satisfies  $\mathbf{N} = \mathbf{p}_1 \times \mathbf{p}_2$  and  $\mathbf{N} \perp \mathbf{p}_1 \perp \mathbf{p}_2$ . At this point we can formulate the criterion for any position vector  $\mathbf{x}$  in space to be part of the cone. To this end we

calculate the tangential coordinates in the projection plane

$$\xi = \frac{\mathbf{x} \cdot \mathbf{p}_1}{\mathbf{x} \cdot \mathbf{N}}, \quad \eta = \frac{\mathbf{x} \cdot \mathbf{p}_2}{\mathbf{x} \cdot \mathbf{N}}$$

and require them to satisfy

$$\xi^2 < \tan^2 \frac{\Delta\alpha}{2}, \quad \frac{\eta^2}{1 + \xi^2} < \tan^2 \frac{\Delta\beta}{2}. \quad (2.25)$$

Since now survey geometry, observer position and line-of-sight are determined, we proceed with filling the four-dimensional Euclidian space-time with a grid of simulation boxes. In the three spatial coordinates we make use of the periodicity of the simulation whereas the time coordinate is given by the 64 snapshot output times corresponding to their respective output redshifts. In practice only those cells in the space-time grid are populated with galaxies which actually intersect the backward lightcone in the field-of-view that we are observing. In particular for the redshift coordinate this means that simulation snapshot  $i$  produced at redshift  $z_i$  occupies only those grid cells which cover comoving distances  $D(z)$  to the observer in the interval  $D(z_{i+1}) < D(z) < D(z_i)$ , where

$$D(z) = \int_0^z \frac{cdz'}{H_0 \sqrt{\Omega_M(1+z')^3 + \Omega_\Lambda}}, \quad (2.26)$$

assuming a flat universe with  $\Omega_M + \Omega_\Lambda = 1$  consistent with the cosmological parameters adopted in Section 4.2.1.

After coarsely filling the volume around the observed lightcone with simulation boxes in this way one can simply chisel off the protruding material, this means we drop all galaxies which do not lie in the field-of-view according to the condition in Eqn. 2.25 or which don't satisfy  $D_{i+1} < |\mathbf{x}| < D_i$  (where  $D(z_i) \equiv D_i$ ). The latter condition raises an additional difficulty since galaxies move between snapshot times and thus it can happen that a galaxy traverses the imaginary snapshot boundary. This will lead to this galaxy being observed either twice or not at all, depending on the direction of its motion. One way to overcome this problem would be to interpolate galaxy positions between snapshots in a consistent way such that every galaxy is observed at position  $\mathbf{x}(t)$  at time  $t$  which in turn reflects the lookback time  $t = t(|\mathbf{x}|)$  as function of its comoving distance. In order to achieve this we introduce the interpolation parameter  $\alpha$  according to  $\mathbf{x} = \mathbf{x}_i + \alpha\Delta\mathbf{x}$  with  $\Delta\mathbf{x} = \mathbf{x}_{i+1} - \mathbf{x}_i$ . Defining  $\Delta r = D_i - D_{i+1}$  and hence requiring  $|\mathbf{x}|^2 \stackrel{!}{=} |D_i - \alpha\Delta r|^2$  leads to the approximate solution

$$\alpha \simeq \frac{D_i^2 - x_i^2}{2[\mathbf{x}_i \cdot \Delta\mathbf{x} + D_i\Delta r]}. \quad (2.27)$$

## 2. The model

---

We don't employ this interpolation though, since our snapshot intervals are too widely spaced, so we would get interpolated dynamical states which are not physical, especially in the centres of clusters where the dynamical times are short. However the interpolation parameter tells us whether a galaxy will cross the snapshot boundary in one direction or the other. For  $\alpha < 0$  the galaxy cannot be observed in the redshift interval  $[z_i, z_{i+1}]$  and we discard it. The case  $\alpha > 1$  is more troublesome since it would create artificial close pairs of galaxies which correspond to the same galaxy observed twice on both sides of the snapshot boundary that it crossed between snapshots  $i$  and  $i + 1$ . We make sure that a galaxy is not duplicated in this way, even though the number of such cases is very small, since for an individual galaxy the probability of boundary crossing is proportional to  $v_r/c$ , where  $v_r$  is the velocity along the line-of-sight and  $c$  is the speed of light. Assuming a Gaussian velocity distribution with velocity dispersion  $\sigma$  the total fraction is of the order  $\sigma/\sqrt{2\pi c^2}$  of the galaxy population. Hence less than 1/1000 of galaxies will be doubled. For 0th-order statistics this is certainly negligible, but also for the statistics of galaxy pairs it turns out that the relative contribution from artificial pairs per radial distance bin never exceeds  $\sim 1\%$  of the total signal. Their spatial distribution is not spherically symmetric though, so for the sake of correct higher order statistics it is still worthwhile to account for artificial pairs.

An alternative would be to consider only FOF groups as a whole and perform the interpolation derived above on the complete object. Hence the internal dynamical states would still be correct but with the advantage that the snapshot boundaries would be guaranteed not to cut through clusters where they could produce discontinuities.

### 2.3.2. Magnitudes

The observed properties of a galaxy depend not only on its intrinsic physical properties but also on the redshift at which it is observed. In particular, the apparent magnitudes of galaxies are usually measured through a filter with fixed transmission curve in the observer's frame. This transmission curve must be blue-shifted to each galaxy's redshift and then convolved with the galaxy's spectral energy distribution in order to obtain an absolute luminosity (inverse k-corrections):

$$E_F(z) = -2.5 \log \frac{\int f_\lambda[t_G(z)]F[(1+z)\lambda]d\lambda}{\int f_\lambda[t_G(0)]F[\lambda]d\lambda} \quad (2.28)$$

This equation traces the aging of the stellar population through  $f_\lambda[t_G(z)]$  and at the same time the "blue-shifting" of the effective filter transmission curves through  $F[(1+z)\lambda]$ .

Then, including the distance modulus, the relation between the observer-frame apparent magnitude and the rest-frame absolute magnitude of the galaxy is simply given by

$$m_F - M_F = 5 \log \frac{D_L(z)}{10\text{pc}} + E_F(z) \quad (2.29)$$

where  $D_L$  is the luminosity distance which is related to the co-moving distance from Eqn. 2.26 with  $D_L = (1 + z) D$ .

### 2.3.3. Geometry in curved space-time

In the following we will demonstrate briefly that only for comoving coordinates within a flat universe do we have the luxury of cutting out light cones from our (replicated) simulation volume simply as we would in Euclidian geometry. In general this is a much less trivial endeavour that requires accounting for the curvature of the universe as well as its expansion with time. (In addition, second-order effects like gravitational lensing should, in principle, be taken into account for any geometry.)

The cosmological line element is

$$ds^2 = dt^2 - a^2(t) \left( \frac{dr^2}{1 + r^2/R^2} + r^2 (d\theta^2 + \sin^2\theta d\phi^2) \right) \quad (2.30)$$

or, if we apply a change of variable

$$r \equiv R \sinh \chi \quad (2.31)$$

this takes on the more elegant form

$$ds^2 = dt^2 - a^2(t) R^2 (d\chi^2 + \sinh^2\chi (d\theta^2 + \sin^2\theta d\phi^2)) \quad (2.32)$$

where all spatial elements are now expressed in terms of angles in a 3-dimensional hyperspace. For a light ray  $ds^2 = 0$  and thus, with setting  $d\chi^2 = d\phi^2 = 0$ , the (time-like) radial distance element becomes

$$dt = a(t) R d\chi \quad (2.33)$$

Integrating it would give the lookback time. Analogously we can get the (space-like) angular distance from the derivative of the angular diameter by setting  $dt^2 = d\chi^2 = d\phi^2 = 0$ :

$$D_A \equiv \frac{ds}{d\theta} = ar = aR \sinh \chi \quad (2.34)$$

On the other hand the comoving distance of an object at a given redshift is defined as the physical distance it has to us at the present when  $a = a_0$ . Therefore we can write

$$dD_M = \frac{a_0 dr}{\sqrt{1 + r^2/R^2}} = a_0 R d\chi \quad (2.35)$$

## 2. The model

---

thus

$$D_M \equiv a_0 R \chi \quad (2.36)$$

Both  $D_A$  and  $D_M$  depend on the coordinate distance  $\chi$  which can be calculated by integrating Eqn. 2.33 divided by  $aR$ :

$$\chi(z) = \int \frac{dt}{aR} = \int \frac{da}{\dot{a}aR} = \int \frac{adz}{\dot{a}a_0R} = \frac{1}{H_0 a_0 R} \int_0^{z_e} \frac{dz}{E(z)} \quad (2.37)$$

where we have used

$$\frac{\dot{a}}{a} = H_0 E(z) \quad (2.38)$$

with

$$E(z) = \sqrt{\Omega_M(1+z)^3 + \Omega_R(1+z)^2 + \Omega_\Lambda} \quad (2.39)$$

Now we show that in a flat universe angular diameter distance and comoving distance are trivially connected. If one starts with Eqn. 2.30 imposing  $R \rightarrow \infty$  and repeating the derivation of angular and comoving distance one arrives straightforwardly at

$$D_A = ar, \quad (2.40)$$

the angular distance in flat space-time and

$$D_M = a_0 r, \quad (2.41)$$

the comoving distance in flat space-time. Hence we get the simple relation

$$D_A = \frac{a}{a_0} D_M = \frac{D_M}{1+z} \quad (2.42)$$

The two distance measures are still different by a factor  $1+z$  but if we consider that the angular diameter is defined in physical units

$$s = D_A \theta \quad (2.43)$$

whereas diameters in the simulation are in comoving units

$$s_{\text{cm}} \equiv \frac{a_0}{a} s \quad (2.44)$$

then we arrive at the final result that in a flat universe and with all distances expressed in comoving units the simple Euclidian relation is recovered:

$$s_{\text{cm}} = \frac{a_0}{a} D_A \theta = D_M \theta \quad (2.45)$$

Finally we conclude this chapter by presenting in Fig. 2.10 an illustrative example, the simulated light cone of a wide survey (to  $I(AB) < 22$ ) of a  $75^\circ \times 9^\circ$  field out to  $z = 0.3$ . Here intensity corresponds to the logarithmic density and the colour encodes morphology in terms of bulge-to-total ratio. The large-scale structure of filaments and voids is evident.



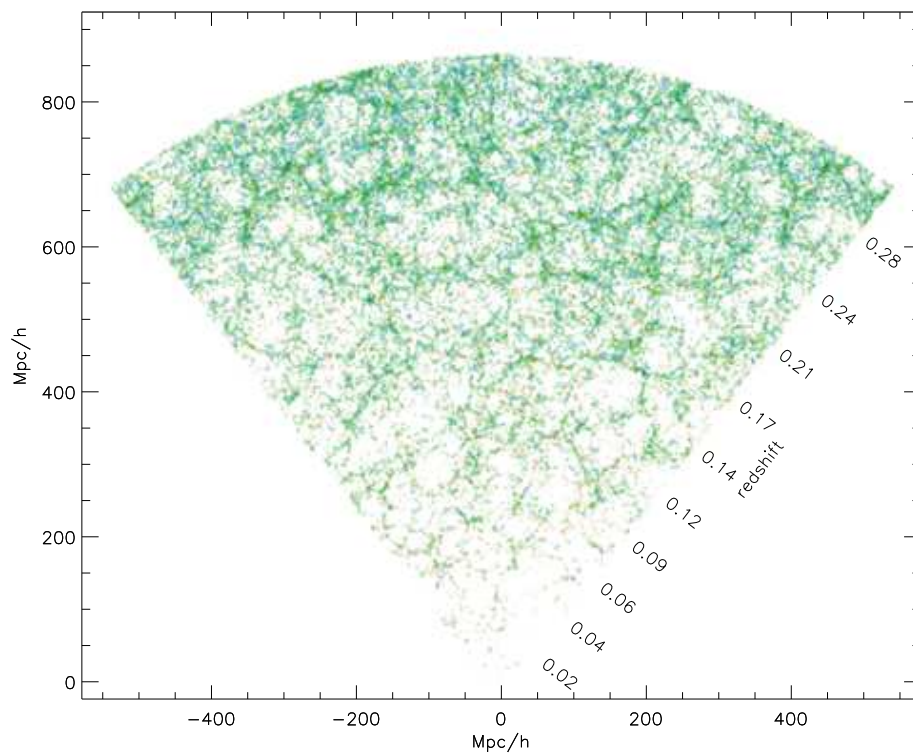


Figure 2.10.: Lightcone with an area of  $75^\circ \times 9^\circ$  out to  $z = 0.3$  at a magnitude limit of  $I(AB) < 22$ . Colours denote average bulge-to-total ratio.

## 2. The model

---

*Essentially, all models are wrong, but some are useful.*

— George E. P. Box

# 3

## Pure Luminosity Evolution Models: Too Few Massive Galaxies at Intermediate and High Redshift

M. G. Kitzbichler & S. D. M. White

*Max-Planck Institut für Astrophysik, Karl-Schwarzschild-Straße 1, D-85748 Garching  
b. München, Germany*

### Abstract

We compare recent galaxy data at low and high redshift to pure luminosity evolution (PLE) models which assume that massive galaxies were assembled and formed most of their stars at high redshift ( $z > 3$ ) and have evolved without merging or substantial dust obscuration since then. Previous studies, typically comparing to only one or a few different PLE parametrisations, painted a diverse picture of whether or not the evolution of bright early-type galaxies is consistent with such models. Here we attempt to gain further insight by exploring a wider parameter space. Our models span the full range of plausible metallicities, initial mass functions (IMF's) and star formation histories. We require them to reproduce the abundance of galaxies by colour and luminosity in the Sloan Digital Sky Survey and we investigate whether they can simultaneously fit (i) the observed galaxy counts as a function of redshift in magnitude limited surveys with  $K < 20$ , and (ii) the colour and  $M/L$  ratio evolution of red sequence galaxies in clusters. All models that are consistent with (ii) predict galaxy counts at  $1.5 < z < 3$  which lie above the observations. This finding does not change with the incorporation of moderate dust extinction,

### 3. PLE: Missing Bright Galaxies at High Redshift

---

confirming previous studies which concluded that for an IMF slope similar to the Salpeter value such models lie far above the data. The progenitors of most present-day massive galaxies must be much more heavily extinguished than currently known galaxies at  $z \geq 1.5$  to match the observed counts at these redshifts. Alternatively the majority of massive galaxies may have assembled at later redshifts as suggested by some hierarchical formation models.

**Key words:** galaxies: general – galaxies: formation – galaxies: evolution – galaxies: luminosity function, mass function – galaxies: elliptical and lenticular, cD

#### 3.1. Introduction

A very wide range of evolutionary histories appear consistent with the observed properties of the present-day population of galaxies. The simplest and most conservative assumption may be that most galaxies were assembled at some early time and their differing stellar populations reflect differing subsequent star formation histories. Massive galaxies – big ellipticals, SO's and early-type spirals – appear to be dominated by old stellar populations, so their star formation rates (SFR) must have been high at early times and must thereafter have declined steeply. Many less massive galaxies – late-type spirals and irregulars – show evidence for substantial recent star formation, so their SFR's may have varied much less. The light of some is clearly dominated by stars from a recent burst.

The recent evolution of the galaxy population in such a scenario can be modelled adopting the backwards-in-time technique first introduced by Tinsley (see [Tinsley 1980](#)). This requires three main ingredients: the present-day luminosity function (LF) of galaxies divided by morphological type (or better by colour); a parametrisation of the mean star formation history (SFH) for each type (or colour class); and a global cosmological model to relate times, distances and redshifts. The SFH is fed into stellar population synthesis models which determine how the luminosities and colours of each type evolve with time. These can then be combined with the cosmological model to predict counts of galaxies as a function of apparent magnitude, observed colour and redshift.

[Kauffmann & Charlot \(1998, KC98 hereafter\)](#) compared available data to the redshift distribution predicted for complete  $K$ -band-limited galaxy samples by such pure luminosity evolution (PLE) models assuming an Einstein–de Sitter cosmology. They found the models to overpredict counts at redshifts  $z > 1$  by a large factor. Since then a number of similar studies have updated the cosmological model to the current concordance cosmology and have presented new observational samples which cover wider areas or go significantly deeper. While the improved observations have reduced the statistical uncertainties, they have not substantially changed the

redshift distributions from those used by KC98. The change to  $\Lambda$ CDM significantly reduced the discrepancy, however, by bringing down the number of high-redshift objects predicted at a given  $K$  magnitude.

Fontana et al. (1999) published a study based on photometric redshifts for a  $K \leq 21$  sample of 319 galaxies in several small fields. Despite using a  $\Lambda$ CDM model their conclusion agreed with KC98; the observed redshift distribution disagreed with their PLE model. Rudnick et al. (2001) found the same result when comparing a range of published PLE models with their photometric redshifts for 95  $K_{s,AB} \leq 22$  galaxies in the Hubble Deep Field South. In part II of a series of papers on the Las Campanas Infrared (LCIR) Survey Firth et al. (2002) present photometric redshifts for 3177 galaxies down to  $H \leq 20$ . They compare these to a number of different PLE models and again find the abundance of high redshift objects to be overpredicted. All these studies echoed the KC98 conclusion that the data suggest that many present-day massive galaxies were assembled at relatively low redshift.

Other recent work based on similar data disagrees with this conclusion. Kashikawa et al. (2003) and Cimatti et al. (2002c) both compare to a modified ‘‘PLE’’ model by Totani et al. (2001). This incorporates a metallicity-dependent dust treatment and high- $z$  selection effects, as well as a simplified parametrisation of mergers (so it is not strictly a PLE model). The galactic-wind model adopted for the formation of ellipticals (Arimoto & Yoshii 1987) assumes an initial star-burst phase with a dust optical depth of  $\tau = 10$  in  $B$ -band. This corresponds to an extinction of 5 mag at  $1.1\mu$  (observer-frame  $K$ -band at  $z = 1$ ) even after 1 Gyr (Fig. 1 in Totani & Yoshii 2000). This model is able to fit the observed redshift distributions because its large assumed dust extinction hides most massive galaxies at redshifts beyond around  $z = 1.5$ , even in observed  $K$ -band.

In this article we are primarily concerned with traditional PLE models in which mergers are neglected and extinction is assumed weak, in particular for massive galaxies after their initial burst of star formation is complete. We will, however, comment briefly on the effects of dust in later sections.

One of the most recent studies comparing PLE predictions to the redshift distributions of  $K$ -selected samples is that of Somerville et al. (2004) who found that although such models overproduce the counts at high redshift, the discrepancy is quite modest. They took advantage of the newly acquired K20 and GOODS survey data, which we also use here, together with other recent high quality survey data, for comparison to our own PLE models. As we will see, our conclusions do not agree with those of Somerville et al. (2004) even for similar models.

More involved studies of number density evolution as a function of galaxy type yield similarly controversial results. Im et al. (2002) found that DEEP survey observations in the Groth strip are consistent with PLE and also with a minor merger scenario out to  $z = 1$ , as long as major star-forming bursts in this redshift interval are excluded. Using LCIR data, Chen et al. (2003) performed a study of the number den-

### 3. PLE: Missing Bright Galaxies at High Redshift

---

sity evolution of galaxies by comparing the LF in  $R$ -band at four different redshifts. They give estimates for the evolution of the comoving luminosity density  $l_R$  in the interval  $0.3 < z < 1.5$  of at the most  $\times 3$  for  $L^*$  galaxies and  $\times 6$  for  $1.6 L^*$  galaxies. Pozzetti et al. (2003) based their work on the  $K20$  survey, which is also used in this paper, finding that out to intermediate redshifts of about 1-1.5, PLE models are consistent with the observations, and that in this redshift range the number density of E/S0 galaxy types decreases at the most by 30%. In the most comprehensive number density evolution study performed recently, Bell et al. (2004) took advantage of the wide area covered by the COMBO-17 survey. They conclude that the colour of red galaxies at a given rest-frame magnitude becomes bluer with redshift, consistent with passive aging of stellar populations, but that the stellar mass on the red sequence has increased at least by a factor of two since  $z = 1$ . This appears consistent with a hierarchical buildup of stellar mass by mergers in a  $\Lambda$ CDM universe. Most recently Saracco et al. (2005) identified 7 bright massive galaxies in the MUNICS survey at redshifts beyond 1.2 which look already evolved. This is consistent with no evolution of the number density of E/S0 galaxies out to a redshift of  $z = 1.7$ , at the same time putting the formation of these galaxies to redshifts well beyond  $z_f = 2$ . Despite their relatively poor statistics these authors conclude that massive ellipticals did not form recently and argue that this finding contradicts the hierarchical model of galaxy formation. Other papers testing this hypothesis are Cimatti et al. (2004) and Glazebrook et al. (2004), the latter finding that only 1/3 of present-day massive galaxies were present at  $z = 1.8$ . Although many hierarchical models of galaxy formation predict even fewer galaxies at this redshift, this is not an intrinsic problem of hierarchical growth but rather a reflection of the specific star-formation recipes adopted.

In this paper we investigate a number of traditional PLE models spanning the full plausible range of metallicity, initial mass function (IMF) and star formation history. The following Section 3.2 describes how our models are set up to reproduce the present-day LF's as a function of colour in the Sloan Digital Sky Survey (SDSS) (§3.2.1) and how various different SFR's and metallicities are assigned to the different colour classes (§3.2.1) in order to follow their luminosity evolution backwards in time. We establish the range of allowed parameters and present five models to illustrate the resulting range of evolutionary predictions. We check that our models reproduce the local  $K$ -band LF, as observed by the 2MASS survey (§3.2.2) as well as the passive evolution of colour and M/L ratio observed for cluster elliptical galaxies. In Section 3.3 we compare the predictions of these models with counts as a function of redshift in recent deep  $K$ -selected surveys.

Finally in the concluding Section 3.4 we discuss possible interpretations of our primary result, that there are fewer luminous galaxies observed at  $z \gtrsim 1.2$  than are expected on the basis of traditional PLE models. One possibility is that much more dust obscures the majority of massive high-redshift galaxies than is present in the

Table 3.1.: Definition of the different galaxy types according to their colour. Also the parameters of the Schechter function fits to the respective LF's are given here.

TYPE	COLOUR $^{0.1}(g-r)$		LF – SCHECHTER FIT		
	MEAN	RANGE	$\Phi[\text{Mpc}/h]^{-3}$	$\alpha$	$_{0.1}M_*$
1....	1.01	0.96 . 1.19	$2.377 \cdot 10^{-3}$	-0.11	-20.96
2....	0.87	0.73 . 0.96	$8.406 \cdot 10^{-3}$	-0.60	-20.61
3....	0.61	0.49 . 0.73	$5.169 \cdot 10^{-3}$	-0.89	-20.49
4....	0.40	0.26 . 0.49	$4.382 \cdot 10^{-3}$	-1.29	-19.84
5....	0.20	0.03 . 0.26	$9.596 \cdot 10^{-4}$	-1.51	-19.11

galaxies that have so far been observed. Alternatively, many present-day massive galaxies simply were not yet assembled by  $z \sim 2$ .

## 3.2. The Models

As mentioned above traditional PLE models require knowledge of the present-day LF's of galaxies as a function of their colour. For each colour class a star formation history (SFH) model is assumed which reproduces its  $z = 0$  colour, and this SFH is then used to predict the LF and the spectral energy distribution (SED) of galaxies of this class at all earlier times. Combining the different classes, galaxy counts can then be predicted as a function of observed magnitude, colour and redshift in any observed photometric band for any assumed cosmological model. In the following we adopt the cosmological parameters of the present standard concordance cosmology:  $\Omega_M = 0.3$ ,  $\Omega_\Lambda = 0.7$ , and  $H_0 = 70 \text{ km s}^{-1} \text{ Mpc}^{-1}$ .

### 3.2.1. From the local LF to the models

Our PLE models are normalised to the luminosity functions at redshift  $z_{\text{LF}} = 0.1$  recently obtained by [Blanton et al. \(2003\)](#) from the data of the SDSS survey ([York et al. 2000](#)). For practical reasons they give the LF in blue-shifted SDSS magnitudes corresponding to the filter wavebands at redshift  $z = 0.1$ , denoted  $^{0.1}u$ ,  $^{0.1}g$  etc. For our purposes the great advantages of these data are their high quality, their superb statistical precision and the fact that they are given in colour-luminosity space (see Fig. 3.1). We separate the data distribution into five colour ranges and calculate the parameters (see Table 3.1) for a Schechter function fit to the LF of each colour bin independently. These parametrised LF's are shown in Fig. 3.2.

### 3. PLE: Missing Bright Galaxies at High Redshift

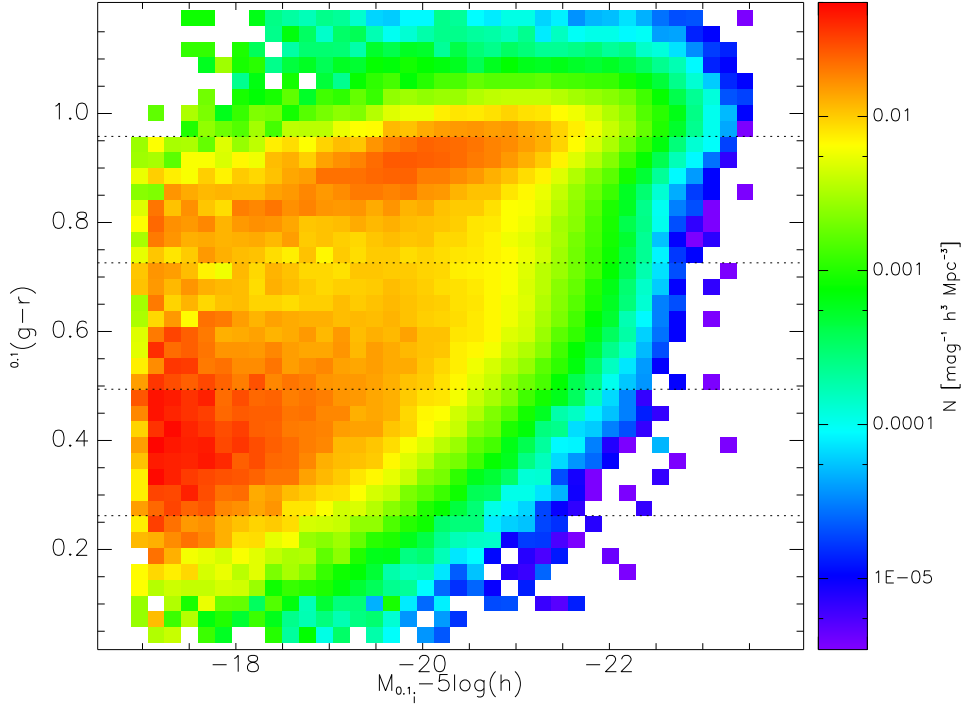


Figure 3.1.: Two dimensional luminosity functions by colour and absolute magnitude taken from [Blanton et al. \(2003\)](#). Black dotted lines indicate the colours separating our different colour classes.

We use the fits of Fig. 3.2 to construct PLE models as described in [Gardner \(1998\)](#) – except for the slight complication that  $z_{\text{LF}} = 0.1$ . The five colour classes are identified with five SFH’s which reproduce their broad-band colours according to the stellar population synthesis models of [Bruzual & Charlot \(2003\)](#). For each galaxy type the spectrum and the LF can then be evolved backwards in time in order to predict the properties of the galaxy population at earlier redshifts.

The assignment of SFH to present-day colour is far from unique, so we construct a variety of possible models differing in their IMF, metallicity, formation redshift  $z_f$  (defined as the redshift when stars start to form) and e-folding timescale  $\tau$  for an assumed exponentially declining SFR. We assume all colour classes to have the same  $z_f$ , except for the bluest one, which often cannot be fit by any exponentially declining SFR. This is a particular problem for models with a steep IMF. In such cases we assume a SFH with constant SFR seen at a fixed age, implying *no* evolution with



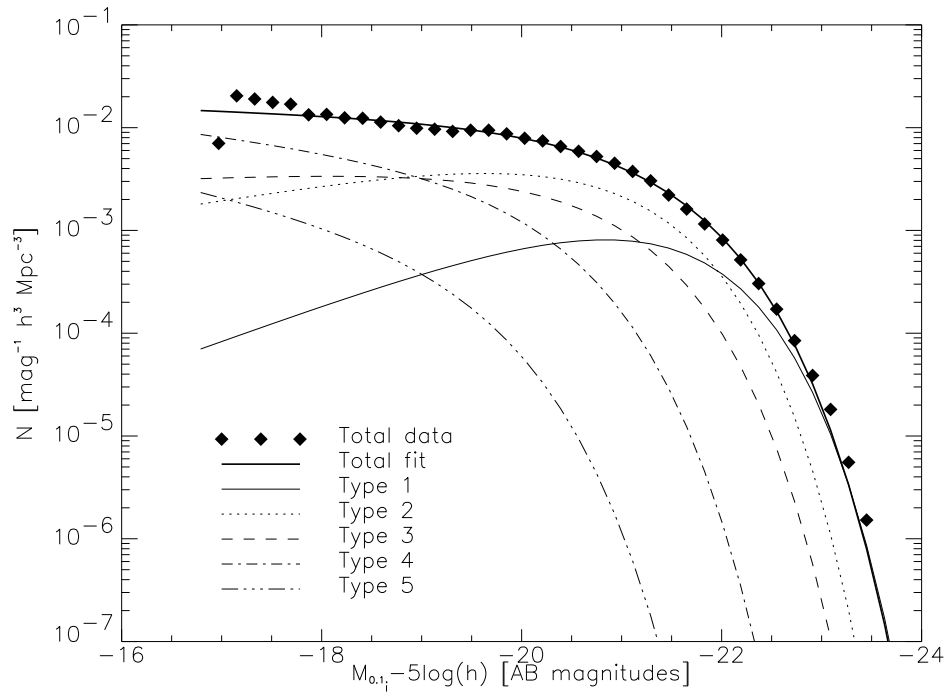


Figure 3.2.: Schechter function fits to the luminosity functions of SDSS galaxies in our five different colour classes (see also Table 3.1).

redshift. This is the standard fix for this problem, which is, in any case, irrelevant for the questions we study here.

We limit the range of allowed parameters in our PLE models by requiring consistency with the observed, apparently passive evolution of bright early-type galaxies in clusters. We require the  $B$ -band mass-to-light ratio of our reddest colour classes to evolve similarly to the measurements of [van Dokkum & Stanford \(2003\)](#). As the left three panels in Fig. 3.3 show, this mainly constrains the slope of the IMF, given that one has considerable freedom in the choice of the formation redshift  $z_f$ . IMF's with a power law exponent of  $x = 2.0$  (where the Salpeter exponent is  $x = 1.35$ ) are excluded, except possibly for the lowest formation redshifts. We nevertheless adopt this slope for Model 4 below in order to study its implications. We note that recent work on IMF's at high redshift have tended to argue for  $x < 1.35$  ("top-heavy IMF's") in order to explain the high luminosities of sub-millimeter luminous galaxies and the apparently high aggregate metal yields of early generations of stars (see [Nagashima et al. 2004](#)).

### 3. PLE: Missing Bright Galaxies at High Redshift

Table 3.2.: Definition of the different models. The given parameters are: slope of the IMF –  $x$ , formation redshift –  $z_{\text{form}}$ , and exponential fall-off time of the SFR –  $\tau$  (where  $\infty$  means constant star formation rate).

MODEL	0	1	2	3	4
IMF $x$	1.35	1.5	1.35	1.5	2.0
$z_{\text{form}}$	15	15	3.5	3.5	3.5
$\tau_1 \dots$	1.5	2.0	1.5	1.5	1.5
$\tau_2 \dots$	3.0	3.0	2.5	2.5	3.0
$\tau_3 \dots$	6.0	10.0	5.0	7.0	30.0
$\tau_4 \dots$	$\infty$	* $\infty$	$\infty$	* $\infty$	* $\infty$
$\tau_5 \dots$	* $\infty$	* $\infty$	* $\infty$	* $\infty$	* $\infty$

The \* denotes galaxy types without evolution.

We also require the rest-frame  $U$ - $B$  colours of the reddest colour class to match those of bright ellipticals in two clusters, the Coma cluster at  $z = 0.023$  and MS 1054-03 at  $z = 0.87$  (Gavazzi et al. 1991; van Dokkum et al. 1999). This allows only a narrow range of metallicities for these bright early-types, namely approximately solar, as can be seen from the three right-hand panels in Fig. 3.3 which show the evolution in rest-frame colour for stellar populations of given metallicity formed with a Salpeter IMF in a single burst at a variety of redshifts. IMF variations have very little effect on this colour since it is dominated by main sequence turn-off stars (as explained by Bruzual & Charlot 2003).

We present results for five representative models that are at least marginally consistent with all these constraints. Their parameters are summarised in Table 3.2 and were selected to cover the whole range of permitted values.

#### 3.2.2. The $K$ -band LF as a consistency test

The LF's used here were measured in the rest frame  $^{0.1}i$ -band. We can check the reliability of our stellar population models for the five colour classes by using them to predict the  $K$ -band ( $2.2 \mu\text{m}$ ) luminosity function of local galaxies. This is of particular interest because near-IR light is a relatively good tracer of stellar mass, depending only weakly on dust content and SFH. We therefore compare the present-day  $K$ -band LF produced by our models to the observed function as given by Kochanek et al. (2001). As can be seen in Fig. 3.4, models and data agree reasonably well apart from a slight magnitude offset, perhaps  $\sim 0.15^m$ , at the bright end. This is likely due to the rather bright isophotal magnitudes used by Kochanek et al. in contrast to the surface-brightness independent Petrosian magnitudes of the SDSS survey. The difference is most pronounced for elliptical galaxies with de Vaucouleur-type sur-

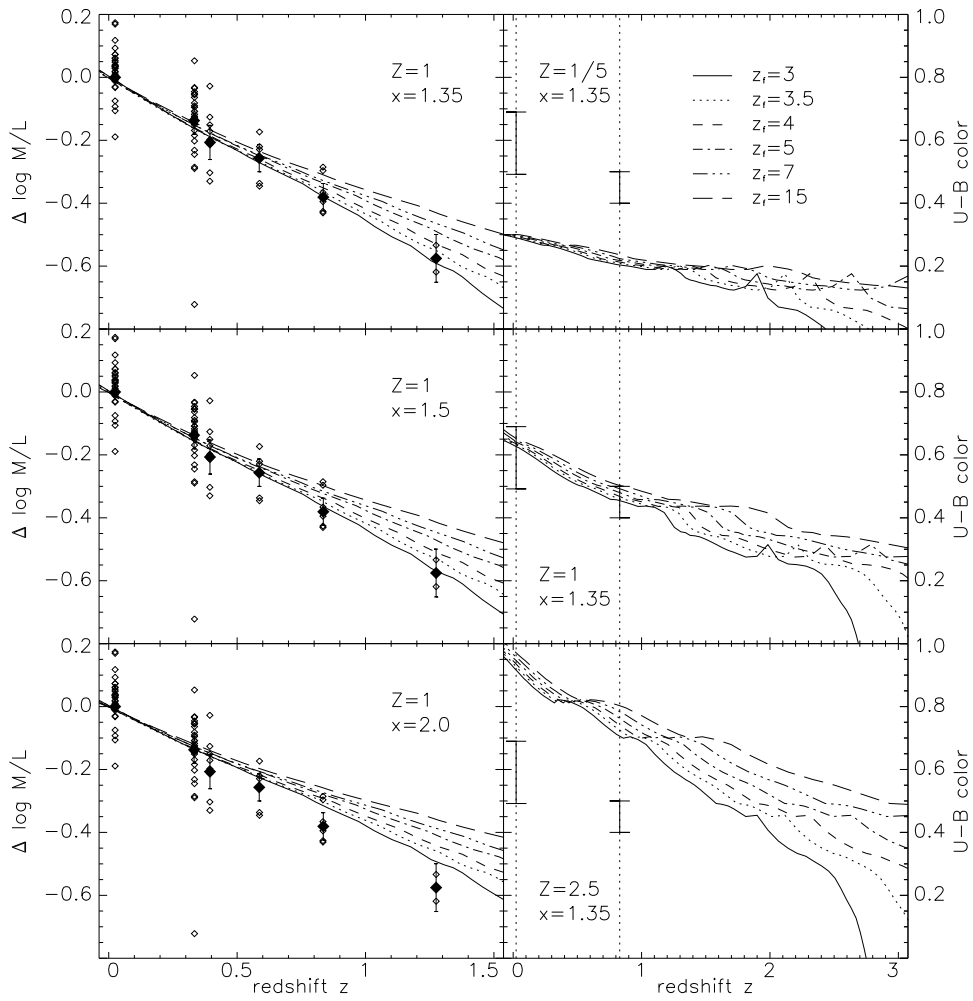


Figure 3.3.: *Left*: Evolution of the mass-to-light ratio of cluster ellipticals in the  $B$ -band as given by [van Dokkum & Stanford \(2003\)](#). Small open symbols denote individual galaxies while big filled symbols stand for data averaged over a number of massive galaxies in a cluster. The model predictions are shown for different  $z_f$  and IMF slopes ranging from  $x = 1.35$  at the top to  $x = 2$  at the bottom. *Right*: Rest-frame  $U-B$  evolution of model early-type galaxies compared to the rest-frame  $U-B$  colours of cluster ellipticals at  $z = 0.87$  (MS 1054-03) and at  $z = 0.023$  (Coma). Model predictions are shown for different  $z_f$  and for three metallicities,  $0.2Z_\odot$ ,  $Z_\odot$  and  $2.5Z_\odot$  from top to bottom.

### 3. PLE: Missing Bright Galaxies at High Redshift

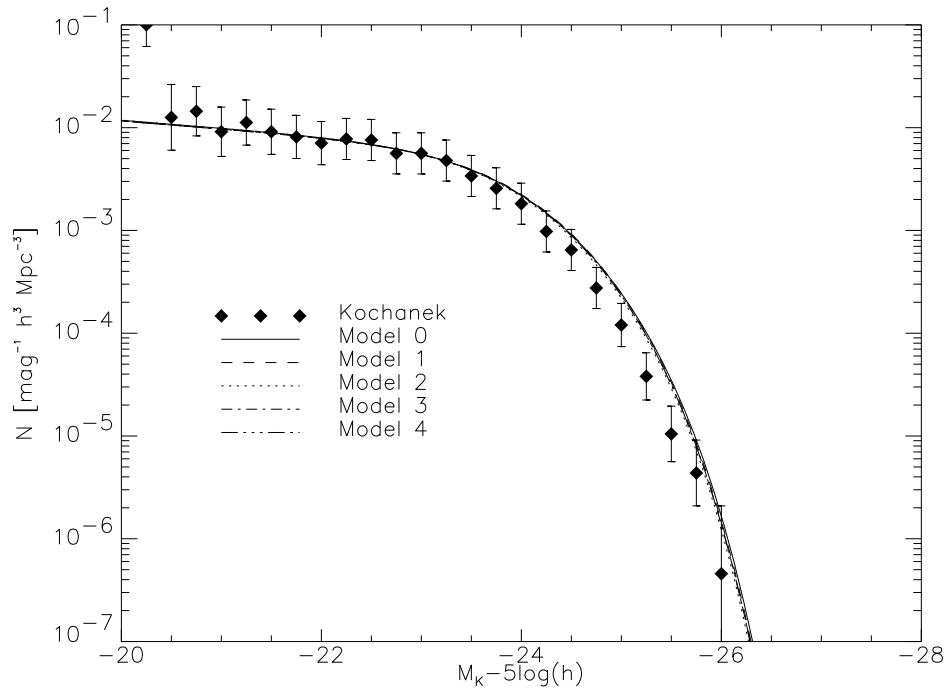


Figure 3.4.: Comparison of our model  $K$ -band LF's with the one that Kochanek et al. (2001) derived from 2MASS data. The slight offset at bright magnitudes can be accounted for by differing magnitude definitions in the SDSS and 2MASS surveys.

face brightness profiles. These dominate the bright end of the LF (see also Andreon 2002).

### 3.3. Comparison of $K$ -band Selected Redshift Distributions

In this paper we compare to the same deep surveys as Somerville et al. (2004), namely GOODS CDF-S covering about  $160 \text{ arcmin}^2$  with photometric redshifts obtained by Mobasher et al. (2004), and K20 carried out in a smaller area of the same field covering  $52 \text{ arcmin}^2$  but providing spectroscopic redshifts rather than photometric ones (Cimatti et al. 2002b). The differential distribution of galaxies per  $\text{arcmin}^2$  and per unit redshift interval is shown in Fig. 3.5 for both datasets, binned to  $\Delta z = 0.15$  and with Poisson errorbars. Clearly there is some substructure in these

### 3.3. Comparison of *K*-band Selected Redshift Distributions

---

distributions due to the relatively small fields surveyed. In particular at  $z \sim 0.7$  there is a prominent peak in the K20 data. This feature is still visible in Fig. 3.6, the cumulative redshift distribution of galaxies. In a larger comoving volume such fluctuations should average out consistent with the smoother curves obtained for the somewhat larger GOODS survey.

Superposed on the observational data in Figs 3.5 and 3.6 we show the differential and cumulative redshift distributions predicted by the various models specified in Table 3.2. In addition three extensions to these models are presented, incorporating dust extinction or complete obscuration of populations.

The first, which we refer to as a “moderate dust model”, is the treatment advocated by Gardner (1998) whose number-count model we adopted. For more details see his paper and references therein. Secondly we insert a redshift-dependent dust optical-depth in Gardner’s slab model for extinction in massive galaxies (assuming that dust and young stars are intermingled), with  $\tau_B$  scaling as  $(z - 1)^n$  for  $z \geq 1$ , mimicking perhaps the case in which this population was born in a very dusty starburst. Thirdly, as a slight variation, we assume that only a redshift-dependent fraction  $f \sim z^{-s}$  for  $z \geq 1$  of the progenitors of present-day ellipticals is visible, the remainder being completely obscured by dust. These two models are loosely based on the results of Totani et al. (2001), whose modified “PLE” model seems to be able to match observations (see Introduction).

It should be noted here that all dust treatments have a significant effect only at higher redshifts, in particular in the observed *K*-band which becomes seriously affected by dust extinction only at redshifts beyond  $z \sim 1 - 1.5$  when it starts to enter rest-frame optical wavelengths.

Figs 3.5 and 3.6 show differential and cumulative counts per arcmin<sup>2</sup>. In the inset of Fig. 3.6, we additionally show cumulative plots normalised to unity, demonstrating that the predicted redshift distributions differ in shape as well as in amplitude.

In order to quantify the obvious discrepancy between observations and models, Table 3.3 presents expected and measured counts integrated over various redshift ranges. The standard Salpeter model, Model 0, overpredicts the observed counts beyond  $z = 1$  by a factor of almost 3, beyond  $z = 1.5$  by more than a factor of 5, and beyond  $z = 2$  by nearly an order of magnitude. The assumption of “moderate dust extinction” barely affects this problem, since even at  $z = 3$  the differential counts are only lowered by about 20% for all models.

By construction, the models with substantial high- $z$  dust extinction can bring the counts down to the right numbers. The required slab model extinction in the first case is  $\tau_B = 7(z - 1)^{1/2}$  for  $z > 1$ , resulting in an equivalent foreground screen extinction in the rest-frame *B*-band of 2.11 magnitudes at  $z = 2$ . In the second model the dependence of the fraction of visible galaxies is  $f = z^{-5/2}$  for  $z > 1$ , which hides about 80% of the massive galaxy population at  $z = 2$ . It should be emphasized that these are just toy models, which help to indicate the required magnitude of extinction

### 3. PLE: Missing Bright Galaxies at High Redshift

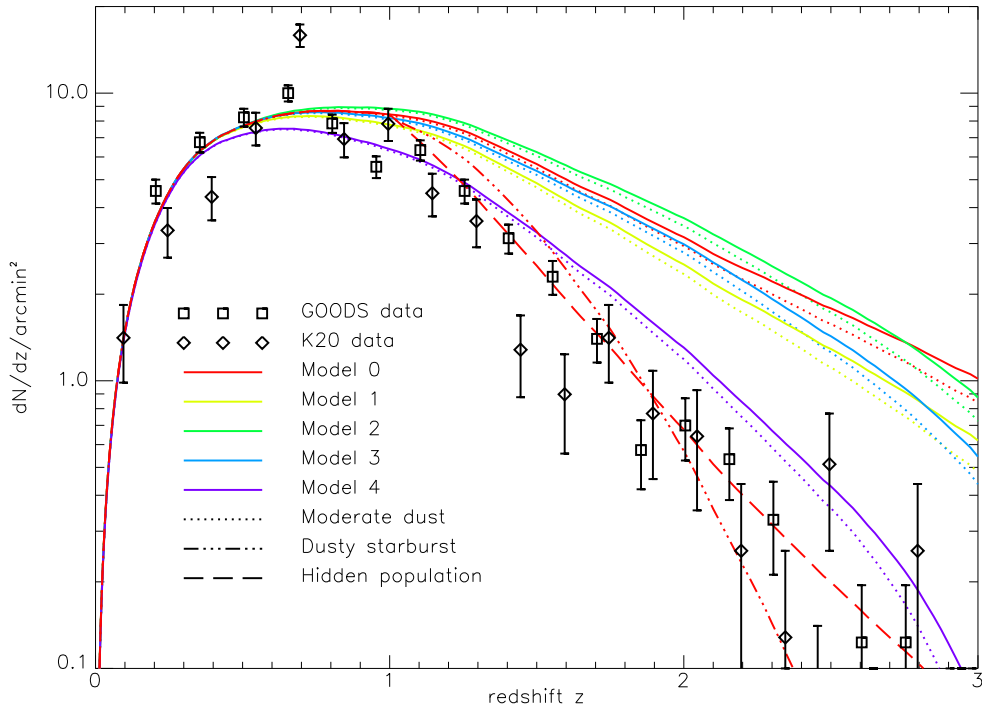


Figure 3.5.: Differential redshift distributions for  $K < 20$  galaxies. The errors plotted on the observational data points are approximate Poisson errors. Our 5 PLE models without dust are shown as continuous curves of different colours as indicated in the figure. Dotted lines denote the same models with moderate dust extinction. The effects of much more substantial extinction are illustrated for model 0 only, denoted by the dot-dashed curve (dusty starburst) and the dashed curve (hidden population). See text for details.

effects.

### 3.4. Discussion and Conclusions

The problem we study in this paper is whether the available observational data are consistent with the idea that present-day luminous galaxies assembled the bulk of their stars at high redshift. If so, it should be possible to find a set of parameters such that traditional PLE models can simultaneously reproduce: (i) the present-day

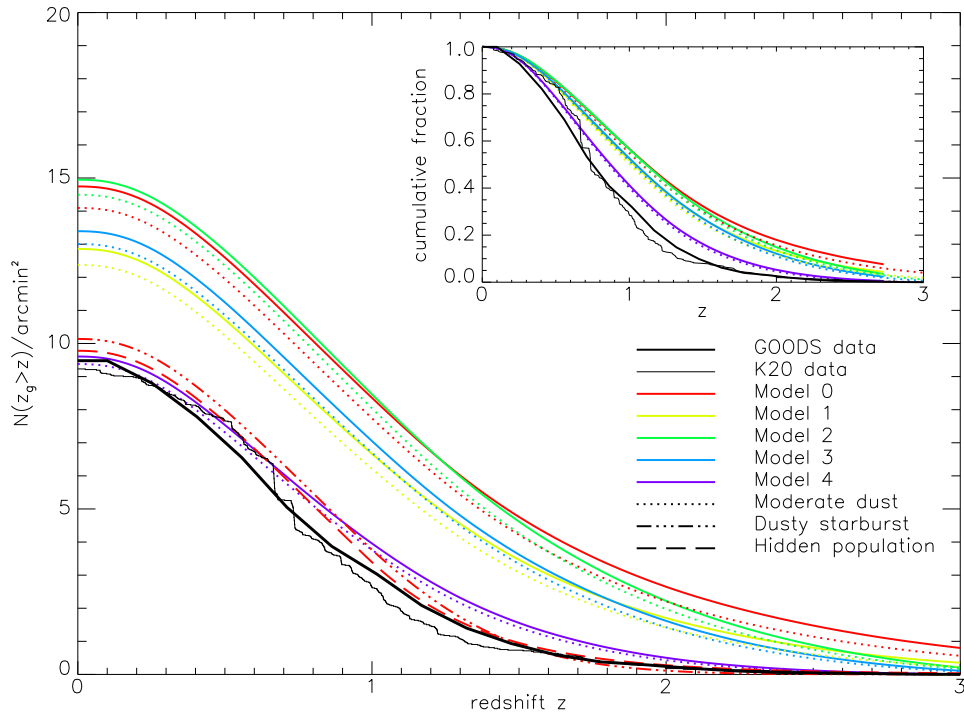


Figure 3.6.: Cumulative redshift distributions corresponding to the differential distributions of Fig. 3.5. Colours and line styles have the same meaning as in Fig. 3.5. The inset shows the same distributions normalised to 1.0 at  $z = 0$  rather than the absolute counts per arcmin<sup>2</sup>.

luminosity and colour distributions of massive galaxies; (ii) the passive evolution in colour and M/L ratio observed for massive early-type galaxies in clusters; and (iii) the observed galaxy counts as a function of redshift in deep surveys. Near-IR limited surveys are best suited for this purpose since the observed magnitudes are then a fair indicator of stellar mass and are only weakly affected by dust. We therefore chose *K*-band data from the K20 and GOODS CDF-S surveys for comparison with our models.

Out to redshift  $z \sim 1$  our model predictions are very similar to each other and also fit the data reasonably well, given their error bars. At higher redshifts all models predict too many galaxies. Only Model 4, with  $x = 2$ , comes close to the data. Obviously the assumed IMF slope has the largest impact on the predicted number of galaxies at high redshift; the second and third best models are the two with  $x = 1.5$ .

### 3. PLE: Missing Bright Galaxies at High Redshift

Table 3.3.: Predicted and observed galaxy counts per arcmin<sup>2</sup> in the redshift range  $1 < z < 3$  for a magnitude limit in  $K$ -band of  $K < 20$ .

MODEL	COUNTS [arcmin <sup>-2</sup> ]				
	$z \geq 1$	$z \geq 1.5$	$z \geq 2$	$z \geq 2.5$	$z \geq 3$
0 .....	8.36	4.76	2.65	1.48	0.80
1 .....	6.66	3.46	1.70	0.81	0.35
2 .....	8.47	4.62	2.22	0.88	0.21
3 .....	7.05	3.62	1.62	0.58	0.11
4 .....	3.96	1.56	0.50	0.12	0.01
0 (moderate dust)	7.74	4.21	2.21	1.14	0.56
1 (moderate dust)	6.21	3.08	1.41	0.61	0.23
2 (moderate dust)	8.04	4.27	1.97	0.75	0.16
3 (moderate dust)	6.70	3.34	1.43	0.48	0.08
4 (moderate dust)	3.76	1.42	0.43	0.09	0.00
Dusty starburst . . .	3.77	0.90	0.11	0.01	0.00
Hidden population	3.39	0.95	0.28	0.09	0.03
K20 .....	2.63	0.73	0.17	0.06	0.00
GOODS .....	3.04	0.93	0.29	0.04	0.00

Changing the formation redshift only mildly influences the shape of the distributions at  $z < 2.5$ . The more conventional standard Model 0, using a Salpeter IMF, and its low  $z_f$  pendant, Model 1, produce the predictions most inconsistent with the data. This may be understood by recalling that the light of old stellar populations is dominated by stars with masses near the main sequence turn-off. For younger populations this turn-off is at higher masses. Hence a shallower IMF implies brighter galaxies at early times, and so more high-redshift galaxies above any apparent magnitude limit. The  $B$ -band M/L ratio evolution of the brightest and reddest galaxies is an important constraint on our models because it is also sensitive to the IMF for the same reasons. As already noted in Section 3.2.1 models with  $x = 2$  are inconsistent with observation, except possibly for very low formation redshifts. Finally, since most models for the light output and metal production of high-redshift galaxies require IMF's with substantially *more* high mass stars than Salpeter (e.g. [Nagashima et al. 2004](#)), an IMF as steep as  $x = 2$  appears very unlikely as an explanation of the apparent lack of high-redshift massive galaxies. This is an important result since many observational publications still compare their data to PLE models with rather steep Scalo IMF's, finding reasonably good agreement (e.g. [Cimatti et al. 2002c](#), and references therein).



### 3.4. Discussion and Conclusions

---

Our Model 0 is very similar to the PLE model used by Somerville et al. (2004) but whereas we find it to be badly inconsistent with the data, they concluded that any problem is marginal. There are two reasons for this discrepancy. Looking at their Figure 1 there is clearly a problem in going from their differential redshift distribution, which is very similar to our own, to the cumulative distribution, which predicts substantially fewer high-redshift galaxies than does ours. In addition, they compare the cumulative distribution to the data after normalising both to unity (as in the inset to Fig. 3.6) which then misses the fact that the total predicted galaxy count at  $K < 20$  is substantially larger than observed.

All of our unobscured models with  $x \leq 1.5$  overpredict the counts at redshifts  $z > 1$  by a large factor as can be seen in Table 3.3. In the interval  $1 < z < 2$  these models all predict more than twice the number of galaxies observed and in the interval  $2 < z < 3$  they are off by factors between 4 and 11. Could cosmic variance or dust account for this? The clustering of galaxies has the greatest effect at low redshift, where the observed volume is comparatively small and clear evidence of large fluctuations is seen in Fig. 3.5 at  $z = 0.7$  in the K20 data. However in this range the models still agree quite well with the data. Only at higher redshifts do they deviate. Also the model predictions are obviously systematically too high at all  $z$  which is not what one would expect if the effect was due to cosmic variance. Finally, models and data also disagree in the normalised version of the diagram (inset in Fig. 3.6).

Extinction by dust, on the other hand, might indeed be important. From looking at Figs 3.5 and 3.6 as well as Table 3.3 it becomes clear that the simple dust treatment conventionally applied to PLE models (e.g. Gardner 1998) is not sufficient. A more extreme assumption about the amount of extinction at high redshift like that of Totani et al. (2001) is needed.

To assess how much dust is required to bring our PLE models into agreement with the data, consider placing a foreground screen in front of all galaxies at  $z = 1.5$ , thereby translating their apparent luminosity function fainter by some fixed amount. We find that to lower the count for Model 0 in Fig. 3.5 by the factor of 2.1 needed to bring it into agreement with the GOODS data at this redshift requires 0.7 magnitudes of extinction at observed  $K$  (i.e. at rest-frame  $z$ ). Carrying out a similar calculation at  $z = 2$  we find that 1.0 magnitudes of extinction is required at observed  $K$  (now rest-frame  $r$ ) to reduce the abundance by the required factor of 5.1. These numbers are consistent with the slightly more detailed models of Figs 3.5 and 3.6. For comparison, Kauffmann et al. (2003) analysed dust attenuation in a sample of 122808 low-redshift galaxies drawn from the SDSS, finding a typical (median) attenuation of 0.2 – 0.3 magnitudes in the  $z$ -band for massive galaxies. We thus need more dust in high-redshift massive galaxies than is seen in local galaxies to reconcile our PLE models with the data.

Note that these toy dust models substantially *under*predict the amount of dust

### 3. PLE: Missing Bright Galaxies at High Redshift

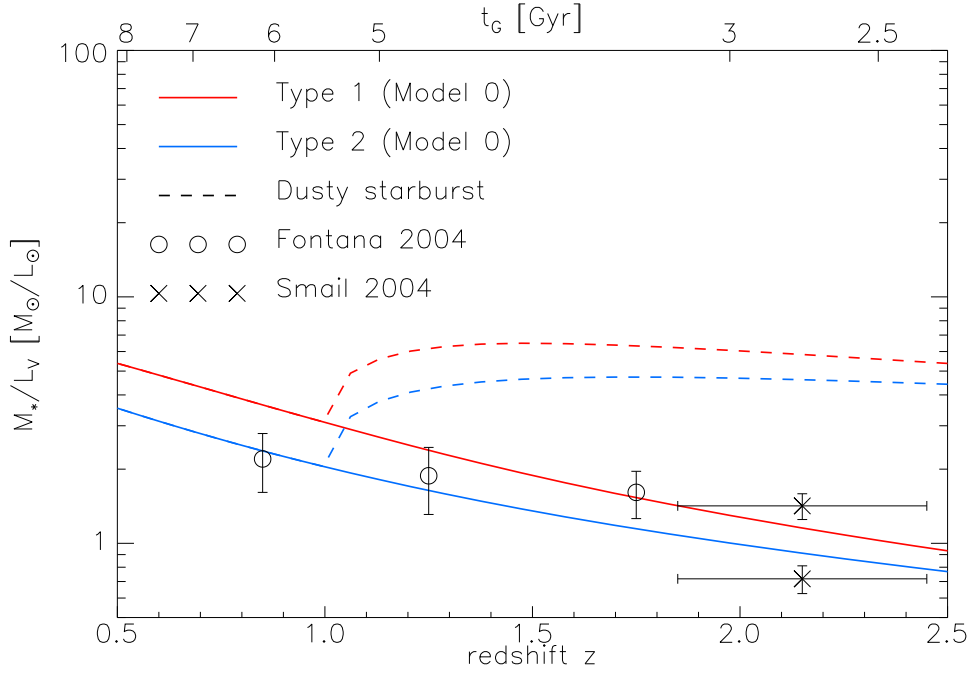


Figure 3.7.:  $M_*/L_V$  ratios of early-type galaxies as function of redshift taken from the literature compared to Colour Types 1 and 2 from our Model 0. Solid lines correspond to the unobscured model while dashed lines show the “dusty starburst” model (see Figs 3.5 and 3.6). The data points from [Smail et al. \(2004\)](#) are the mean for a sample of submillimetre-galaxies at  $\langle z \rangle = 2.2$  for two different assumed SFHs, a single burst (lower value) and a constant SFR (upper value) model. The data from the K20 sample of [Fontana et al. \(2004\)](#) are combined into 3 redshift bins.

needed to get agreement since they assume the stellar populations of the dusty galaxies to be just as old as in the unobscured models which are no longer rapidly forming stars in Type 1 galaxies at  $z < 2$ . In the nearby universe younger stellar populations are almost always present in dusty galaxies, and the enhanced luminosity due to the young stars cancels almost exactly the attenuation effects of the dust, resulting in a mean apparent  $M/L$  ratio for red galaxies which depends weakly on dust content at red optical wavelength ([Bell & de Jong 2001](#); [Kauffmann et al. 2003](#)). If high-redshift galaxies behave similarly, then dust will *not* help reconcile our PLE models with the data.

### 3.4. Discussion and Conclusions

---

Recent data do, in fact, indicate such behaviour, as illustrated in Fig. 3.7. Here we compare the evolution of rest-frame  $M/L_V$  predicted by our Model 0 and by its “dusty starburst” variant with observational estimates for two classes of high-redshift galaxy. Fontana et al. (2004) provide estimates for  $\sim 140$   $K$ -selected early-type galaxies from the K20 survey. This sample contains both unobscured “passive” systems and dusty, star-forming galaxies. We plot mean values with their uncertainties for bins centered at  $z = 0.85, 1.25$  and  $1.75$ . Smail et al. (2004) provide estimates from optical follow-up of a sample of 96 submillimeter-selected galaxies. These are all highly obscured, strongly star-forming galaxies. We plot mean  $M/L_V$  estimates with their quoted uncertainties for the two star-formation histories considered by Smail et al., namely a single short burst (the lower value) and a constant SFR (the upper value). The theoretical curves correspond to Colour Types 1 and 2 which contribute 48% and 47%, respectively, of all galaxies at  $z > 1.5$  and  $K < 20$  in our Model 0.

Figure 3.7 demonstrates that the  $M/L_V$  values assumed in our standard PLE model with no or moderate obscuration are very similar to those measured in real high-redshift galaxies, even though the observed systems are both dusty and star-forming. On the other hand, when we fit our *ad hoc* “dusty starburst” model to the observed redshift counts, it predicts  $M/L_V$  values well above those estimated for high-redshift galaxies, even those selected specifically for the strength of their dust emission. Thus PLE models with moderate obscuration match the observed mass-to-light ratios at high redshift but overpredict abundances, while models with sufficient obscuration to fit the observed abundances substantially overpredict high-redshift mass-to-light ratios.

Our main conclusion is thus that “traditional” PLE models, as originally introduced by Tinsley, cannot reconcile the relatively small number of high-redshift galaxies found in deep  $K$ -selected redshift surveys with the abundance of massive galaxies seen in the local Universe. The counterparts of nearby luminous red galaxies just do not seem to be present in sufficient numbers at redshifts of 1.5 to 2. The areas of current deep surveys are quite small, so there may still be significant uncertainties as a result of cosmic variance. Substantial amounts of dust may also cause many distant massive galaxies to be missed, but only if dust attenuation is not compensated by emission from young stars in the way observed in low-redshift galaxies and if the  $M/L$  values estimated for current samples of high-redshift galaxies are atypically small. Observation of the relevant galaxy populations over larger areas and at longer wavelengths will help to get a better understanding of this question.

**Acknowledgements:** We would like to thank the anonymous referee for his comments which helped to improve this paper. MGK acknowledges a PhD fellowship from the International Max Planck Research School in Astrophysics, and support from a Marie Curie Host Fellowship for Early Stage Research Training.

### 3. PLE: Missing Bright Galaxies at High Redshift

---

*Study the past if you would divine the future.*

— Confucius

# 4

## The high redshift galaxy population in hierarchical galaxy formation models

M. G. Kitzbichler & S. D. M. White

*Max-Planck Institut für Astrophysik, Karl-Schwarzschild-Straße 1, D-85748 Garching  
b. München, Germany*

### Abstract

We compare observations of the high redshift galaxy population to the predictions of the galaxy formation model of [Croton et al.](#) and [De Lucia & Blaizot](#). This model, implemented on the Millennium Simulation of the concordance  $\Lambda$ CDM cosmogony, introduces “radio mode” feedback from the central galaxies of groups and clusters in order to obtain quantitative agreement with the luminosity, colour, morphology and clustering properties of the present-day galaxy population. Here we construct deep light cone surveys in order to compare model predictions to the observed counts and redshift distributions of distant galaxies, as well as to their inferred luminosity and mass functions out to redshift 5. With the exception of the mass functions, all these properties are sensitive to modelling of dust obscuration. A simple but plausible treatment agrees moderately well with most of the data. The predicted abundance of relatively massive ( $\sim M_*$ ) galaxies appears systematically high at high redshift, suggesting that such galaxies assemble earlier in this model than in the real Universe. An independent galaxy formation model implemented on the same simulation matches the observed mass functions slightly better, so

## 4. High redshift galaxies

---

the discrepancy probably reflects incomplete or inaccurate galaxy formation physics rather than problems with the underlying cosmogony.

**Key words:** galaxies: general – galaxies: formation – galaxies: evolution – galaxies: luminosity function, mass function

### 4.1. Introduction

Recent work has used the very large Millennium Simulation to follow the evolution of the galaxy population throughout a large volume of the concordance  $\Lambda$ CDM cosmogony (Springel et al. 2005; Croton et al. 2006; Bower et al. 2006; De Lucia et al. 2006; De Lucia & Blaizot 2007). By implementing “semi-analytic” treatments of baryonic processes on the stored merger trees of all halos and subhalos, the formation and evolution of about  $10^7$  galaxies can be simulated in some detail. The inclusion of “radio mode” feedback from the central galaxies in groups and clusters allowed these authors to obtain good fits to the local galaxy population and to cure several problems which had plagued earlier galaxy formation modelling of this type. In particular, they were able to produce galaxy luminosity functions with the observed exponential cut-off, dominated at bright magnitudes by passively evolving, predominantly elliptical galaxies. At the same time, this new ingredient provided an energetically plausible explanation for the failure of “cooling flows” to produce extremely massive galaxies in cluster cores. Most of this work compared model predictions to the systematic properties and clustering of the observed low redshift galaxy population, or studied the predicted formation paths of massive galaxies. Only Bower et al. (2006) compared their model in detail to some of the currently available data at high redshift. In the present paper we compare these same data and others to the galaxy formation model of Croton et al. (2006) as updated by De Lucia & Blaizot (2007) and made publicly available through the Millennium Simulation data site.<sup>1</sup> A number of example mock lightcones providing apparent magnitudes in Johnson and SDSS filters as well as other observed properties can also be found there. These lightcones are linked to the main simulation output which provides the full set of galaxy properties that our model calculates.

Many recent observational studies have emphasised their detection of substantial populations of massive galaxies out to at least redshift 2 and have seen this as conflicting with expectations from hierarchical formation models in the  $\Lambda$ CDM cosmogony (e.g. Cimatti et al. 2002c; Im et al. 2002; Pozzetti et al. 2003; Kashikawa et al. 2003; Chen et al. 2003; Somerville et al. 2004). This notion reflects in part the fact that early hierarchical models assumed an Einstein-de-Sitter cosmogony in which recent evolution is stronger than for  $\Lambda$ CDM (e.g. Fontana et al. 1999). In

---

<sup>1</sup><http://www.mpa-garching.mpg.de/millennium>; see Lemson et al. (2006)

part it is due to an underassessment of the predictions of the contrasting toy model, typically assumed to be pure luminosity evolution (PLE), in which massive galaxies assemble at high redshift and thereafter evolve in luminosity alone. In [Kitzbichler & White \(2006\)](#) we have shown that these models tend to overpredict the number of galaxies at redshifts beyond  $z = 1.5$  by large factors, unless one invokes an uncomfortably steep IMF or much stronger dust extinction than observed at this redshift.

[Bower et al. \(2006\)](#) find their model to be in good agreement with current observational estimates of the abundance of massive galaxies at high redshift, while our comparisons below suggest that the model of [Croton et al. \(2006\)](#) and [De Lucia & Blaizot \(2007\)](#) appears, if anything, to *overpredict* this abundance. As shown by these authors and particularly by [De Lucia et al. \(2006\)](#) both models predict “anti-hierarchical” behaviour, in that star formation completes earlier in more massive galaxies. This behaviour clearly does not conflict with the underlying hierarchical growth of structure in a  $\Lambda$ CDM cosmogony. A fact which also shows how important it is to include all relevant physics in order to get a realistic galaxy population and explains why significant differences have been found between different semi-analytic models in the past, even though they were built on very similar cosmogonies. Our model and the one of [Bower et al.](#) however, both based on the Millennium simulation, give quite similar results, as may be seen in detail using the above mentioned database which contains both catalogues.

The current paper is organised as follows. In Section 4.2 we briefly describe the Millennium Simulation and the fiducial galaxy formation model we are adopting. Where we have made modifications, most significantly in the dust treatment, these are described in detail. We also give a detailed account of how we construct mock catalogues of galaxies along the backward lightcone of a particular simulated field of observation. Many of our methods resemble those which [Blaizot et al. \(2005\)](#) implemented in their MOMAF facility in order to enable mock observations of simulated galaxy catalogues of the same type as (though smaller than) the Millennium Run catalogues we use here. Our results are summarised in Section 4.3 where we compare number counts as a function of apparent magnitude and redshift with the currently available observational data. We also compare the predicted evolution of the luminosity and stellar mass functions to results derived from recent observational surveys, and we illustrate how the population of galaxies is predicted to shift in the colour-absolute magnitude plane. Finally in Section 4.4 we interpret our findings and present our conclusions.

## 4. High redshift galaxies

---

### 4.2. The Model

#### 4.2.1. The Millennium dark matter simulation

We make use of the Millennium Run, a very large simulation which follows the hierarchical growth of dark matter structures from redshift  $z = 127$  to the present. The simulation assumes the concordance  $\Lambda$ CDM cosmology and follows the trajectories of  $2160^3 \simeq 1.0078 \times 10^{10}$  particles in a periodic box  $500 \text{ Mpc}/h$  on a side. A full description is given by [Springel et al. \(2005\)](#); here we summarise the main simulation characteristics as follows:

The adopted cosmological parameter values are consistent with a combined analysis of the 2dFGRS ([Colless et al. 2001](#)) and the first-year WMAP data ([Spergel et al. 2003](#); [Seljak et al. 2005](#)). Specifically, the simulation takes  $\Omega_{\text{m}} = \Omega_{\text{dm}} + \Omega_{\text{b}} = 0.25$ ,  $\Omega_{\text{b}} = 0.045$ ,  $h = 0.73$ ,  $\Omega_{\Lambda} = 0.75$ ,  $n = 1$ , and  $\sigma_8 = 0.9$  where all parameters are defined in the standard way. The adopted particle number and simulation volume imply a particle mass of  $8.6 \times 10^8 h^{-1} M_{\odot}$ . This mass resolution is sufficient to resolve the haloes hosting galaxies as faint as  $0.1 L_{\star}$  with at least  $\sim 100$  particles. The initial conditions at  $z = 127$  were created by displacing particles from a homogeneous, ‘glass-like’ distribution using a Gaussian random field with the  $\Lambda$ CDM linear power spectrum.

In order to perform such a large simulation on the available hardware, a special version of the GADGET-2 code ([Springel et al. 2001b](#); [Springel 2005](#)) was created with very low memory consumption. The computational algorithm combines a hierarchical multipole expansion, or ‘tree’ method ([Barnes & Hut 1986](#)), with a Fourier transform particle-mesh method ([Hockney & Eastwood 1981](#)). The short-range gravitational force law is softened on comoving scale  $5 h^{-1} \text{ kpc}$  which may be taken as the spatial resolution limit of the calculation, thus achieving a dynamic range of  $10^5$  in 3D. Data from the simulation were stored at 63 epochs spaced approximately logarithmically in time at early times and approximately linearly in time at late times (with  $\Delta t \sim 300 \text{ Myr}$ ). Post-processing software identified all resolved dark haloes and their subhaloes in each of these outputs and then linked them together between neighbouring outputs to construct a detailed formation tree for every object present at the final time. Galaxy formation modelling is then carried out in post-processing on this stored data structure.

#### 4.2.2. The basic semi-analytic model

Our semi-analytic model is that of [Croton et al. \(2006\)](#) as updated by [De Lucia & Blaizot \(2007\)](#) and made public on the Millennium Simulation data download site (see [Lemson et al. 2006](#)). These models include the physical processes and modelling techniques originally introduced by [White & Frenk \(1991\)](#); [Kauffmann](#)



et al. (1993); Kauffmann & Charlot (1998); Kauffmann et al. (1999); Kauffmann & Haehnelt (2000); Springel et al. (2001a) and De Lucia et al. (2004), principally gas cooling, star formation, chemical and hydrodynamic feedback from supernovae, stellar population synthesis modelling of photometric evolution and growth of supermassive black holes by accretion and merging. They also include a treatment (based on that of Kravtsov et al. 2004) of the suppression of infall onto dwarf galaxies as consequence of reionisation heating. More importantly, they include an entirely new treatment of “radio mode” feedback from galaxies at the centres of groups and clusters containing a static hot gas atmosphere. The equations specifying the various aspects of the model and the specific parameter choices made are listed in Croton et al. (2006) and De Lucia & Blaizot (2007). The only change made here is in the dust model as described in the next section.

### 4.2.3. Improved dust treatment for the fiducial model

Even at low redshifts, a crucial ingredient in estimating appropriate magnitudes for model galaxies, particularly in the  $B$ -band, is the dust model. Previously our dust model had been calibrated using observations in the local universe by Wang & Heckman (1996) who found the simple relationship between face on optical depth and intrinsic luminosity  $\tau \propto \tau_0 (L/L_*)^\beta$ , where  $\beta \sim 0.5$ . For the present-day luminosity function (LF) this phenomenological treatment has traditionally given satisfactory results (Kauffmann et al. 1999). However, the situation at high redshift is more delicate because of the much higher predicted gas (and thus dust) columns, the highly variable predicted metallicities, and the shorter emitted wavelengths corresponding to typical observed photometric bands. We found we had to adopt a new approach in order to be consistent with current data on extinction in high redshift galaxies. Devriendt et al. (1999) advocate a dust model based on the HI column density in the galaxy disk, a quantity that can be estimated from the cold gas mass and the disk size of a galaxy, both of which are available for each galaxy in our semi-analytic model. A plausible scaling of dust-to-gas ratio with metallicity can easily be incorporated using the metal content given by a chemical evolution model (cf. Devriendt & Guiderdoni 2000). Based on this we get

$$\tau_\lambda^Z = \left( \frac{A}{A_V} \right)_{Z_\odot} \eta_Z \left( \frac{\langle N_H \rangle}{2.1 \times 10^{21} \text{cm}^{-2}} \right) \quad (4.1)$$

with the average hydrogen column density obtained from

$$\langle N_H \rangle = \frac{M_{\text{gas}}}{1.4 \mu m_p \pi r_t^2}. \quad (4.2)$$

$A/A_V$  here is the extinction curve from Cardelli et al. (1989). We assume the dust-to-gas ratio to scale with metallicity and redshift as  $\eta_Z = (1+z)^{-\frac{1}{2}} (Z_{\text{gas}}/Z_\odot)^s$ ,

## 4. High redshift galaxies

---

where  $s = 1.35$  for  $\lambda < 2000 \text{ \AA}$  and  $s = 1.6$  for  $\lambda > 2000 \text{ \AA}$ . The factor of  $(1+z)^{-\frac{1}{2}}$  in this formula is adopted in order to reproduce results for Lyman-break galaxies at  $z \sim 3$ . [Adelberger & Steidel \(2000\)](#) find  $\langle \tau \rangle_{1600} \lesssim 2$  at rest-frame  $1600 \text{ \AA}$ , showing that dust-to-gas ratios are lower at this redshift compared to the local universe for objects of the same  $L_{\text{bol}}$  and metallicity (a result echoed in [Reddy et al. 2006](#)). This behaviour also agrees with a recent study of the dust-to-gas/dust-to-metallicity ratio by [Inoue \(2003\)](#). Please note that the average extinction of our model galaxies still increases strongly with redshift due both to the ever shorter rest-frame bands we probe and to the smaller disk sizes we predict at higher redshift (see equations 4.1 and 4.2 above).

Finally, one must also take into account the inclination of the galaxy to the line-of-sight when making an extinction correction. For a thin disc where dust and stars are uniformly mixed, commonly called slab geometry, the total extinction in magnitudes is

$$A_{\lambda}^Z = -2.5 \log \left( \frac{1 - e^{-\tau_{\lambda}^Z \sec \theta}}{\tau_{\lambda}^Z \sec \theta} \right) \quad (4.3)$$

The inclination angle  $\theta$  we draw from a random distribution which is flat in  $\cos \theta$ , and we account for the fact that for very large inclination angles the above equation would lead infinite extinction whereas in reality one observes only a thin band of dust in such edge on galaxies. Hence we limit the extinction not to exceed the universal value  $e^{-\tau_{\lambda}^Z}$ .

It is worth noting that other authors have used similar dust models in their semi-analytic treatment, some of them more sophisticated than ours. [Cole et al. \(2000\)](#) determine the optical depth in a similar way as in Eqn. 4.1, but assume a more realistic 3D distribution of the dust involving an independent disc scale-height and a more accurate derivation of the disc scale-length (however using a Monte-Carlo algorithm rather than an N-body simulation). Overall they get very similar values to ours, in particular the same strength of extinction in  $B$ -band at redshift  $z = 0$  of  $0.5 \text{ mag}$  on the bright end of the LF, where it is most important. The dust model of [Hatton et al. \(2003\)](#) also uses Eqn. 4.1 for the optical depth and adopts the same method for determining the disk scale length as we do. Additionally they take into account the contribution from the bulge and they also define a starburst component of recently formed stars which they treat differently. Most importantly however they include scattering and thermal reemission by the dust, allowing them to extend the predictions of their model into the mid- and far-IR regime, albeit subject to the assumption that the dust properties do not evolve with time.

#### 4.2.4. Making mock observations: lightcones

From a theoretical point of view it would be most convenient to compare predictions for the basic physical properties of galaxies directly with observation, but in practice this is rarely possible. For faint and distant object the most observationally accessible properties are usually fluxes in specific observer-defined bands. Quantities such as stellar mass or star-formation rate (often even redshift) must be derived from these quantities and are subject to substantial uncertainties stemming primarily from the assumptions on which the conversion is based. Moreover which galaxies can be observed at all (and so are included in observational samples) is typically controlled by observational selection effects on apparent magnitude, colour, surface brightness, proximity to other images and so on.

In order to minimise these uncertainties when drawing astrophysical conclusions about the galaxy population, it is beneficial to have a simulated set of galaxies with known intrinsic properties from which “observational” properties can be calculated, and to apply the same conversions and selection effects to this mock sample as to the real data. One can then assess the accuracy with which the underlying physical properties can be inferred. In this approach the uncertain relations between fundamental and observable quantities become part of the model, and their influence on any conclusions drawn can be assessed by varying the corresponding assumptions throughout their physically plausible range. A disadvantage is that shortcomings in, for example, the galaxy formation model are convolved with many other effects (for example the conversion from mass to luminosity) and separation of these effects can be difficult. In particular, it may become difficult to identify why a particular model disagrees with the data, since effects from many different sources may be degenerate.

We make mock observations of our artificial universe, constructed from the Millennium Simulation, by positioning a virtual observer at zero redshift and finding those galaxies which lie on his backward light cone. The backward light cone is defined as the set of all light-like worldlines intersecting the position of the observer at redshift zero. It is thus a three-dimensional hypersurface in four-dimensional space-time satisfying the condition that light emitted from every point is received by the observer now. Its space-like projection is the volume within the observer’s current particle horizon. From this sphere, which would correspond to an all-sky observation, we cut out a wedge defined by the assumed field-of-view of our mock observation. It is common practice to use the term *light cone* for this wedge rather than for the full (all-sky) light cone, and we will follow this terminology here.

The issues which arise in constructing such light cones have been addressed in considerable detail by [Blaizot et al. \(2005\)](#). In the following we adopt their proposed solutions in some cases (for example, when interpolating the photometric properties of galaxies to redshifts for which the data were not stored) and alternative solutions in others (for example when dealing with the limitations arising from the finite extent

## 4. High redshift galaxies

---

of the simulation). We refer readers to their paper for further discussion and for illustration of the size of the artifacts which can result from the limitations of this construction process.

There are two major problems to address when constructing a light cone from the numerical data. The first arises because the Millennium Simulation was carried out in a cubic region of side 500 Mpc/h whereas the comoving distance along the past light cone to redshift 1 is 2390 Mpc/h and to redshift 6 is 6130 Mpc/h. Thus deep light cones must use the underlying periodicity and traverse the fundamental simulation volume a number of times. Care is needed to minimise multiple appearances of individual objects, and to ensure that when they do occur they are at widely different redshifts and are at different positions on the virtual sky. The second problem arises because redshift varies continuously along the past light cone whereas we have stored the positions, velocities and properties of our galaxies (and of the associated dark matter) only at a finite set of redshifts spaced at approximately 300 Myr intervals out to  $z = 1$  and progressively closer at higher redshift. We now present our adopted solutions to each of these problems in turn.

### 4.2.4.1. How to avoid making a kaleidoscope

The underlying scale of the Millennium Simulation 500 Mpc/h, corresponds to the comoving distance to  $z \sim 0.17$ . However, we want to produce galaxy catalogues which are at least as deep as the current observations, and, in practice, to be one or two generations in advance. Although the periodicity of the simulation allows us to fill space with any required number of replications of the fundamental volume, this leads to obvious artifacts if the simulation is viewed along one of its preferred axes. We can avoid this kaleidoscopic effect by orienting the survey field appropriately on the virtual sky with respect to the three directions defined by the sides of the fundamental cube. The “best” choice depends both on the shape and depth of the survey being simulated, and on the criteria adopted to judge the seriousness of the artifacts to be minimised. Here we do not give an optimal solution to the general problem, but rather a solution which works acceptably well for deep surveys of relatively small fields.

Consider a Cartesian coordinate system with origin at one corner of the fundamental cube and with axes parallel to its sides. Consider the line-of-sight from this origin passing through the point  $(L/m, L/n, L)$  where  $m$  and  $n$  are integers with no common factor and  $L$  is the side of the cube. This line-of-sight will first pass through a periodic image of the origin at the point  $(nL, mL, nmL)$ , i.e. after passing through  $nm$  replications of the simulation. If we take the observational field to be defined by the lines-of sight to the four points  $((n \pm 0.5/m)L, (m \pm 0.5/n)L, nmL)$ , it will be almost rectangular and it will have total volume  $L^3/3$  out to distance  $(n^2 + m^2 + n^2m^2)^{0.5}L$ . Furthermore no point of the fundamental cube is imaged

more than once. This geometry thus gives a mock light cone for a near-rectangular survey of size  $1/m^2n \times 1/n^2m$  (in radians) with the first duplicate point at distance  $\sim mnL$ . For example, if we take  $m = 2$  and  $n = 3$  we can make a mock light cone for a  $4.8^\circ \times 3.2^\circ$  field out to  $z = 1.37$  without any duplications. For  $m = 3$  and  $n = 4$  we can do the same for a  $1.6^\circ \times 1.2^\circ$  area out to  $z = 5.6$ . Choosing  $m = 1$  and  $n = 5$  results in a  $11.5^\circ \times 2.3^\circ$  survey with no duplications out to  $z = 1.06$ .

If we wish to construct a mock survey for a larger field or to a greater distance than these numbers allow, then we have to live with some replication of structure. Choosing the central line-of-sight to be in a ‘‘slanted’’ direction of the kind just described with  $m$  and  $n$  values matched roughly to the shape of the desired field usually results in large separations of duplicates in angle and/or in redshift. Careful optimisation is needed for any specific survey geometry in order to get the best possible results. Note that any point within the fundamental cube can be chosen as the origin of a mock survey, and that, in addition, there are four equivalent central lines-of sight around each of the three principal directions of the simulation. It is thus possible to make quite a number of equivalent mock surveys of a given geometry and so to ensure that the full statistical power of the Millennium Run is harnessed when estimating statistics from these mock surveys.

Taking into account the above considerations, we select the central line-of sight to be in the direction of the unit vector  $\mathbf{u}_3$  defined by

$$(m^2 + n^2 + m^2n^2)^{1/2}\mathbf{u}_3 = (n, m, mn), \quad (4.4)$$

we define a second unit vector  $\mathbf{u}_1$  to be perpendicular both to  $\mathbf{u}_3$  and to the unit vector along the coordinate direction associated with the smaller of  $m$  and  $n$  (the  $x$ -axis in the above examples) and we take a third unit vector  $\mathbf{u}_2$  to be perpendicular to the first two so as to define a right-handed Cartesian system. If we define  $\alpha$  and  $\delta$  as local angular coordinates on the sky in the directions of  $\mathbf{u}_1$  and  $\mathbf{u}_2$  respectively, with origin in our chosen central direction, then a particular 3-dimensional position  $\mathbf{x}$  corresponds to

$$\begin{aligned} \tan \alpha &= \mathbf{x} \cdot \mathbf{u}_1 / \mathbf{x} \cdot \mathbf{u}_3 \\ \tan \delta &= \mathbf{x} \cdot \mathbf{u}_2 / \mathbf{x} \cdot \mathbf{u}_3 \end{aligned}$$

The position  $\mathbf{x}$  lies within our target rectangular field provided

$$\begin{aligned} |\tan \alpha| &\leq \tan \Delta\alpha/2 \\ |\tan \delta| &\leq \tan \Delta\delta/2, \end{aligned}$$

Where  $\Delta\alpha$  and  $\Delta\delta$  give desired angular extent of the field in the two orthogonal directions (with  $\Delta\alpha \geq \Delta\delta$  assumed here). Note that this formulation of the condition to be within the light cone does not require any transcendental functions to be applied

## 4. High redshift galaxies

---

to the galaxy positions, allowing membership to be evaluated efficiently. This can be a significant computational advantage when one is required to loop over many replications of the (already large) Millennium galaxy catalogues.

We point out in passing that only for comoving coordinates within a flat universe do we have the luxury of cutting out light cones from our (replicated) simulation volume simply as we would in Euclidian geometry. In general this is a much less trivial endeavour that requires accounting for the curvature of the universe as well as its expansion with time. (In addition, second-order effects like gravitational lensing should, in principle, be taken into account for any geometry.)

### 4.2.4.2. How to get seamless transitions between snapshots

After determining the observer position and survey geometry we fill three-dimensional Euclidian space-time with a periodically replicated grid of simulation boxes, keeping only those which intersect our survey. In practice, since the Millennium Simulation data at each time are stored in a set of 512 spatially disjoint cells, we keep only those cells which intersect the survey. In principle, a galaxy within our survey at comoving distance  $D$  from the observer should be seen as it was at redshift  $z$  where

$$D(z) = \int_0^z \frac{cdz'}{H_0 \sqrt{\Omega_M(1+z')^3 + \Omega_\Lambda}}. \quad (4.5)$$

A problem arises, however, because the positions, velocities and physical properties of our galaxies are stored only at a discrete set of redshifts  $z_i$  corresponding to a discrete set of distances  $D_i$ . (For definiteness we adopt  $z_1 = D_1 = 0$  and  $z_i > z_{i-1}, D_i > D_{i-1}$ .) The comoving distance between outputs is 80 to 240 Mpc/h, corresponding to 100 to 380 Myr, depending on redshift.

One way to deal with this problem would be to interpolate the positions, velocities and physical properties of the galaxies at each distance  $D$  from the output redshifts which bracket it, e.g.  $z_i$  and  $z_{i+1}$  where  $D_{i+1} > D > D_i$ . We decided against this procedure for several reasons. In the first place, the Millennium Simulation appears to give dynamically consistent results for the galaxy distribution down to scales of 10kpc or so (see, for example, the 2-point correlation functions in [Springel et al. 2006](#)). On such scales characteristic orbital timescales are smaller than the spacing between our outputs, so interpolation would produce dynamically incorrect velocities and would diffuse structures. In addition, the physical properties of the galaxies are not easily interpolated because of impulsive processes such as mergers and starbursts. Rather than interpolating, we have chosen to assign the positions, velocities and physical properties stored at redshift  $z_i$  to all survey galaxies with distances from the observer in the range  $(D_i + D_{i+1})/2 > D > (D_i + D_{i-1})/2$ . Individual small scale structures are then dynamically consistent throughout this range, and the phys-

ical properties of the galaxies are offset in time from the correct values by at most half of the time spacing between outputs.

After coarsely filling the volume around the observed light cone with simulation cells in this way one can simply chisel off the protruding material, i.e. drop all galaxies which do not lie in the field according to the condition in Eqn. 4.5 or which don't satisfy  $(D_i + D_{i+1})/2 > D > (D_i + D_{i-1})/2$ . The latter condition causes an additional difficulty since galaxies move between snapshots and thus it can happen that a galaxy traverses the imaginary boundary  $(D_i + D_{i+1})/2$  between the times corresponding to  $z_{i+1}$  and  $z_i$ . This results in this galaxy being observed either twice or not at all, depending on the direction of its motion. We overcome this problem for galaxies close to the boundary by linearly interpolating their positions between  $z_{i+1}$  and  $z_i$  in order to get estimated positions at the redshift corresponding to  $(D_i + D_{i+1})/2$ . Those galaxies whose estimated positions are on the low redshift side of the boundary are assigned properties corresponding to  $z_i$ , those on the high redshift side properties corresponding to  $z_{i+1}$ .

### 4.2.4.3. Getting the right magnitudes

The observed properties of a galaxy depend not only on its intrinsic physical properties but also on the redshift at which it is observed. In particular, the apparent magnitudes of galaxies are usually measured through a filter with fixed transmission curve in the observer's frame. This transmission curve must be blue-shifted to each galaxy's redshift and then convolved with the galaxy's spectral energy distribution in order to obtain an absolute luminosity which can be divided by the square of the luminosity distance to obtain the observed flux. A difficulty arises because quantities like absolute luminosities are accumulated, based on the prior star formation history of each object, at the time the semi-analytic simulation is carried out, and they are stored in files which give the properties of every galaxy at each output redshift  $z_i$ . At this stage the light cone surveys are not yet defined, so we do not know the *exact* redshift at which any particular galaxy will be observed in a particular mock survey. We are thus unable to define the filter function through which its luminosity should be accumulated in order to reproduce properly the desired observer-frame band.

We deal with this problem in the way suggested by [Blaizot et al. \(2005\)](#) by defining ahead of time the observer frame magnitudes we wish to predict, for example, Johnson  $B$ . When carrying out the semi-analytic simulation we then accumulate for all galaxies at redshift  $z_i$  not only the absolute magnitude through the  $B$ -filter blue-shifted to  $z_i$  but also those for the same filter shifted to the frequency bands corresponding to  $z_{i-1}$  and  $z_{i+1}$ . For galaxies in our mock survey whose physical properties correspond to  $z_i$  but which appear on the light cone at  $z > z_i$  we linearly interpolate an estimate for the observer-frame  $B$  absolute magnitude (at redshift  $z$ ) between the values stored for filters blue-shifted to  $z_i$  and  $z_{i+1}$ . Similarly, for those

## 4. High redshift galaxies

---

similar galaxies which appear at  $z < z_i$  we interpolate the absolute magnitude between the values stored for filters blue-shifted to  $z_i$  and  $z_{i-1}$ . It turns out that this interpolation is quite important. Without it, discontinuities in density are readily apparent in the distribution of simulated galaxies in the observed colour-apparent magnitude plane. On the other hand, the total amplitude of the correction between two snapshots is  $\Delta m < 0.1$  out to  $z = 2$  in  $B$ -band and  $\Delta m < 0.05$  in  $K$  out to  $z = 3$ ; also we never interpolate more than half-way to a neighbouring snapshot. Assuming that the inaccuracy arising from the linear interpolation is of the order 10% yields an error estimate of  $\Delta m_B < 5 \cdot 10^{-3}$  and  $\Delta m_K < 2.5 \cdot 10^{-3}$  in the redshift ranges quoted above.

As a general remark it should be mentioned here, that it may seem more obvious to define the mock lightcone first and then run the semi-analytic treatment only on the galaxies that are found to lie in the cone. This way one would know the exact redshift of observation for every galaxy and could refrain from any interpolation. However in practice this approach turns out to be less efficient for at least two reasons. Firstly one would still have to calculate all the physics not only for the members of the mock catalogue but also for all their progenitors since without knowing their history one cannot determine their present properties. This means for every lightcone that covers a significant part of the simulated volume we have to essentially calculate everything for all galaxies anyway. Secondly, even in the case of a very thin pencil beam we want to make as good use as possible of our simulation, producing up to 24 quasi-independent mocks with different observer positions and lines-of-sight, again trying to maximise the fraction of simulation volume examined. The method we have adopted allows us to run the computationally expensive semi-analytic treatment only once, rather than for every single mock we produce. Therefore it provides much more flexibility, as we can consecutively cut out as many lightcones with different geometries from the simulated catalogue as we wish with very little computational overhead.

We conclude this chapter by presenting in Fig.4.1 an illustrative example, the simulated light cone of a deep survey (to  $K_s(AB) < 24$ ) of a  $1.4^\circ \times 1.4^\circ$  field out to  $z = 3.2$ . Here intensity corresponds to the logarithmic density and the colour encodes the offset from the evolving red sequence at the redshift of observation (assuming passive evolution after a single burst at  $z = 6$ ). Large-scale structure is evident and is well sampled out to redshifts of at least  $z \simeq 3$  and it is interesting that at  $z > 2$  the reddest galaxies are predicted to be in the densest regions even though, as we see below, many of them are predicted to be dusty strongly star forming objects. Individual bright galaxies are predicted to be visible out to  $z \simeq 5$  in the full light cone.



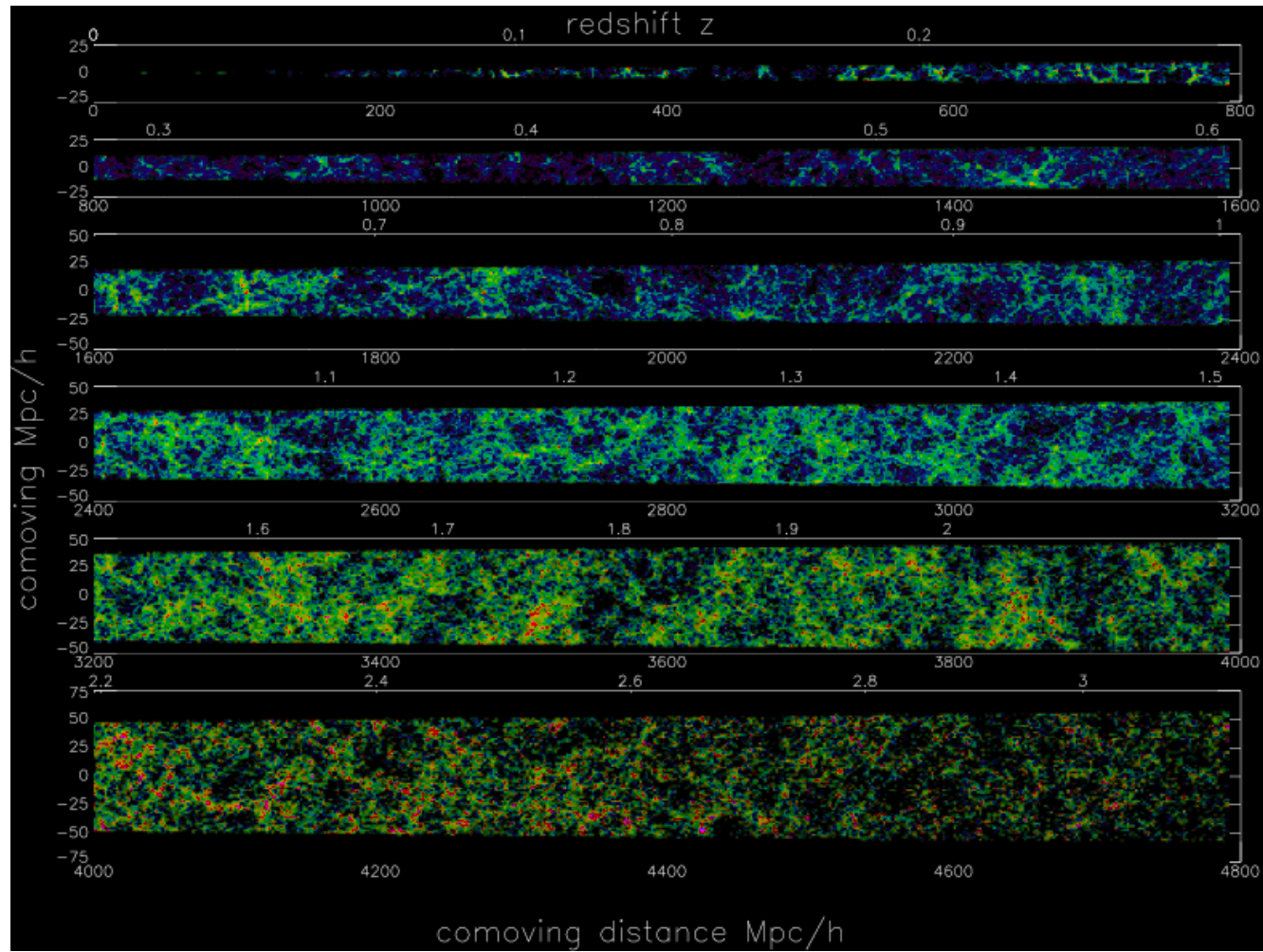


Figure 4.1.: Light cone for a  $1.4^\circ \times 1.4^\circ$  field out to  $z = 3.2$ . All galaxies above an apparent magnitude limit  $K_s(AB) < 24$  are shown, where intensity corresponds to the logarithmic density and the colour denotes the offset from the evolving red sequence.

## 4. High redshift galaxies

---

### 4.3. Results

In this section we first compare our model to directly measured properties of real samples such as their distribution in apparent magnitude and redshift. We then consider derived properties which require an increasing number of additional assumptions, moving from the evolution of rest-frame luminosity functions to that of stellar mass distributions. Finally we illustrate the large changes predicted for the distribution of galaxies in rest-frame colour and absolute magnitude over the redshift range  $0 < z < 3$ . This gives a good impression of the interplay between the various mechanisms that determine the luminosity and colour of galaxies in our model.

All magnitudes are in the  $AB$  system (rather than Vega) unless stated otherwise.

#### 4.3.1. Number Counts

In Fig. 4.2 we compare predicted galaxy counts obtained from a mock survey of a  $2 \square^\circ$  area to observational counts from a number of different surveys. In the  $BRI$  bands we use counts over a  $0.2 \square^\circ$  area in the HDF-N direction by [Capak et al. \(2004\)](#). In the  $K_s$  band we use both the “wide” area ( $320 \text{ arcmin}^2$  distributed over various fields) counts of [Kong et al. \(2006\)](#) and the deeper, but smaller area counts in the CDF and HDF-S directions ( $6$  and  $7.5 \text{ arcmin}^2$  respectively) by [Saracco et al. \(2001\)](#). It is worth noting that for the  $BRI$  bands we were able to use the filter transmission curves appropriate for the *Subaru* survey, whereas for the  $K$  band different effective transmission curves apply for the different surveys and we have not taken this into account. In order to quantify the effect of “cosmic variance” (the fact that large statistical fluctuations are expected in surveys of this size not only from counting statistics but also from large-scale structure along the line-of-sight) we split up our  $2 \square^\circ$  mock survey into 72 fields of size  $100 \text{ arcmin}^2$ . The  $1\sigma$  scatter among counts in these different areas is shown as a grey shaded area surrounding the predicted means for  $BRI$  and for the brighter  $K$  magnitudes. For the fainter  $K$  magnitudes we split our mock survey into smaller subfields, each with an area of  $\sim 11 \text{ arcmin}^2$ . The  $1\sigma$  variations among these subfields are shown by the hatched band surrounding the predicted  $K$  counts at fainter magnitudes. Note that this procedure may still somewhat underestimate the cosmic variance since the different subfields are not truly independent, but all lie within a single  $1.4^\circ \times 1.4^\circ$  mock survey.

In the light of this limitation, and keeping in mind that our dust-model is still rather simple, it is quite surprising to see the excellent agreement of the data with our predictions in all three optical bands. Agreement at  $K$  is less good, and there appears to be a significant discrepancy faintward of  $K_{AB} \sim 21$ . The model predicts almost twice as many galaxies as are observed at  $K_{AB} \sim 23$ , although the agreement is again acceptable at  $K_{AB} \sim 24.5$ . This disagreement appears well outside the statistical errors, but it should be borne in mind that  $K$  magnitudes are extremely

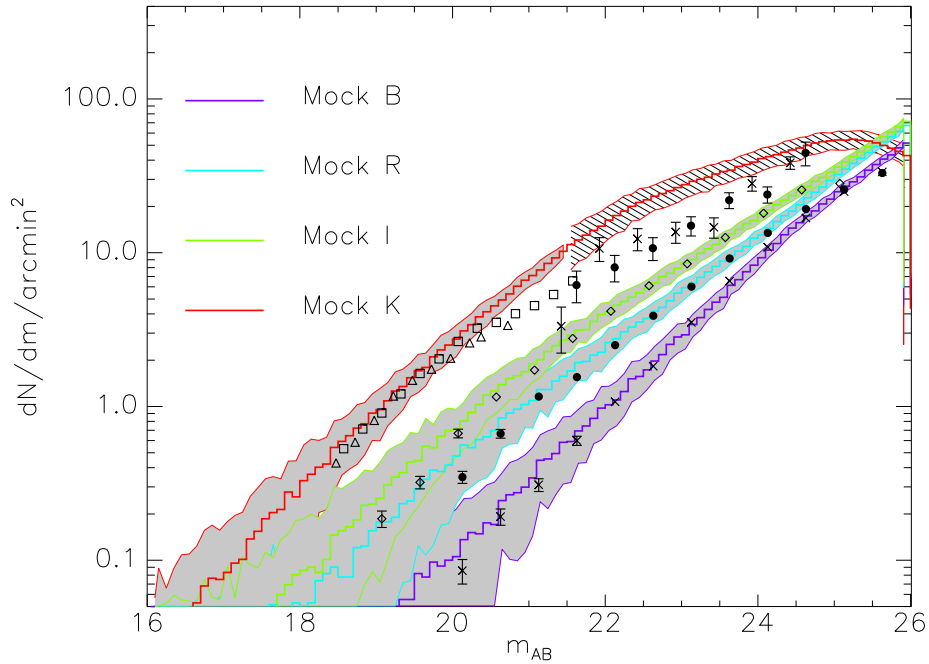


Figure 4.2.: Predicted galaxy counts per unit area in four bands compared to a survey in the HDF-N direction ( $0.2 \square^\circ$ ) in *BRI* and to a number of “wide field” surveys at  $K_s$  (total of  $320 \text{ arcmin}^2$ ), as well as to deep observations at  $K_s$  in the CDF and HDF-S directions ( $6$  and  $7.5 \text{ arcmin}^2$  respectively). The grey shaded error bands show  $1\sigma$  field-to-field variations assuming an area of  $100 \text{ arcmin}^2$ , whereas the hatched error bands show the expected variations for a smaller square field of area  $\sim 11 \text{ arcmin}^2$ .

difficult to measure at such faint levels, and it is possible that the measured quantity does not correspond to the total magnitude assumed in our modelling.

### 4.3.2. Redshift Distributions for *K*-selected samples

In Fig. 4.3 we give the redshift distributions predicted for apparent magnitude limited galaxy samples complete for  $K \leq 21.8$ ,  $K \leq 23.3$ , and  $K \leq 25.8$ . We compare the first of these to data for a  $52 \text{ arcmin}^2$  field from K20 (Cimatti et al. 2002c) and for a  $160 \text{ arcmin}^2$  overlapping field from GOODS (Mobasher et al. 2004). (Note that the name K20 comes from the survey limit in the Vega system. The two systems are approximately related by  $K_{AB} = K_{\text{Vega}} + 1.83$ .) At the intermediate depth we

## 4. High redshift galaxies

---

compare to the photometric redshift distribution obtained by [Caputi et al. \(2006\)](#) for a  $131 \text{ arcmin}^2$  field in the direction of the Chandra Deep Field South (CDF-S). For the faintest magnitude limit we compare to the photo- $z$  distribution of a much smaller  $4 \text{ arcmin}^2$  area in the Subaru Deep Field, as obtained by [Kashikawa et al. \(2003\)](#). Again we split up our simulated field into sub-fields of size  $100 \text{ arcmin}^2$  ( $4 \text{ arcmin}^2$  for  $K \leq 24$ ) in order to get an estimate of the expected  $1\sigma$  scatter, which we indicate by grey shaded areas. For these small fields cosmic variance is quite substantial and the counts can be influenced significantly by individual galaxy clusters. This effect is clearly visible in the K20 and GOODS data, where a pronounced spike is present at  $z \simeq 0.7$ . In addition, systematic problems with the photometric redshift determinations might distort the redshift distributions in some ranges.

Despite these uncertainties, our model predictions appear somewhat high over the redshift range  $0.5 < z < 1.5$  for the K20 and GOODS samples. The deeper  $K \leq 23.3$  observations are overpredicted by a factor of 2 to 3 over the range  $1 < z < 3$ . For the faintest sample there is an apparent overprediction by a somewhat smaller factor over this same redshift range. Comparing with Fig. 4.2, we see that the total overprediction at each of these magnitudes is consistent with that seen in the counts themselves, although it should be borne in mind that the CDF-S field is common to both datasets. The differences we find are larger than the predicted cosmic variance, so they presumably indicate problems with the model (incorrect or inaccurate physics?), with the observational data (systematics in the magnitudes or photo- $z$ 's) or both.

### 4.3.3. Luminosity Function evolution

[Croton et al. \(2006\)](#) demonstrated that at  $z = 0$  the luminosity function (LF) for our model agrees well with observation both in  $b_J$  and in  $K$ . Splitting galaxies according to their intrinsic colours, these authors also found quite good fits to the LF's for red and blue galaxies separately, with some discrepancies for faint red galaxies. Here we compare the evolution of the LF predicted by our model in *rest-frame*  $B$  and  $K$  band with recent observational results.

#### 4.3.3.1. The $B$ -band Luminosity Function

In Fig. 4.4 we compare the evolution of the rest frame  $B$ -band LF predicted by our simulation to results from the DEEP2 survey ([Willmer et al. 2006](#)). As a  $z = 0$  standard we use the local LF from the 2dF survey [Norberg et al. \(2002\)](#). This is compared with our model in the top-left panel and is repeated as a thin red line in each of the other panels, where the high redshift data are indicated by points with error bars. Our predicted LF is shown in each panel as a solid line with a grey area indicating the  $1\sigma$  scatter to be expected for an estimate from a survey

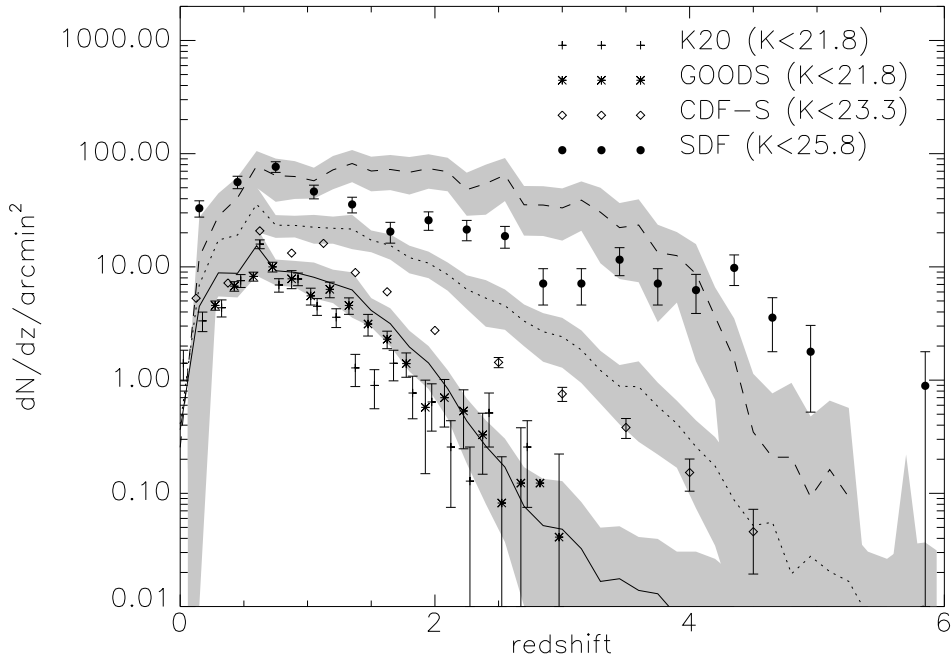


Figure 4.3.: Predicted redshift distributions for galaxies to a magnitude limit of  $K \leq 21.8$  (solid), 23.3 (dotted), and 25.8 (dashed). These are compared to observational results from K20 and GOODS ( $K \leq 21.8$ ), from CDF-S ( $K \leq 23.3$ ) and from SDF ( $K \leq 25.8$ ). The latter two are derived purely from photometric redshift estimates. Error bars on the observational points are based on counting statistics only. Grey shaded areas indicate the  $1\sigma$  field-to-field scatter assuming an area of  $100 \text{ arcmin}^2$  for the two brighter magnitude limits and  $4 \text{ arcmin}^2$  for  $K \leq 25.8$ .

similar in effective volume to the observational survey. (Note that in all cases the Millennium Simulation is much larger than this effective volume, so that counting noise uncertainties in the prediction are negligible.)

At  $z = 0$  the agreement between model and observation is excellent. This is a consequence of the fact that [Croton et al. \(2006\)](#) and [De Lucia et al. \(2006\)](#) adjusted model parameters in order to optimise this agreement. However, over the full redshift range from  $z = 0.2$  to 1.2 the predicted LF's agree with the DEEP2 data at the  $1\sigma$  level or better. On closer examination, it appears that the model somewhat overpredicts the observational abundance fainter than the knee of the luminosity function,

#### 4. High redshift galaxies

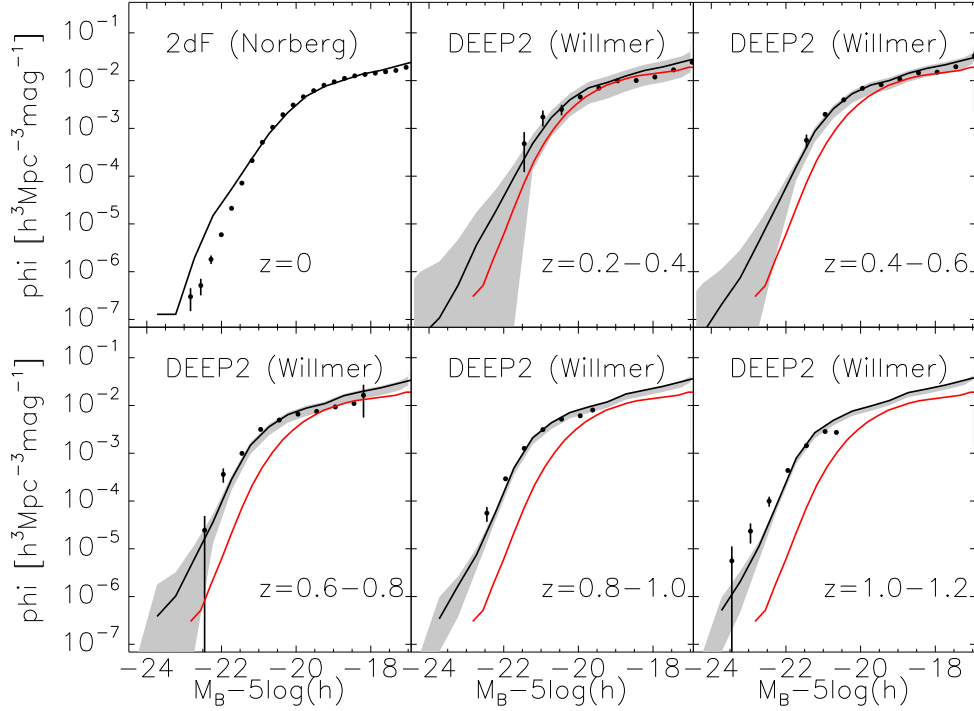


Figure 4.4.: Comparison of the rest-frame  $B$ -band LF predicted by our simulation for redshifts in the range  $0 < z < 1.2$  to observational estimates from [Norberg et al. \(2002\)](#) at  $z = 0$  and from [Willmer et al. \(2006\)](#) at higher redshifts. The local LF of the upper left panel is repeated as a thin red line in each of the other panels. A grey shaded region surrounding each model prediction shows the  $1\sigma$  scatter expected in observational estimates based on samples similar in size to the corresponding observational sample.

by a factor  $\sim 1.5$  depending on redshift. On the other hand, at the higher redshifts very luminous galaxies appear slightly more abundant in the real data than in the model. It is important to keep in mind that our dust model has a strong influence here, the average extinction for galaxies brighter than the knee is  $A_B \simeq 0.8$  at  $z = 1$  compared to  $A_K \lesssim 0.2$  in  $K$ -band. Plausible modifications to it might account for either or both of these minor discrepancies. In general, the agreement with the data seems quite impressive, at least in this band and over this redshift range.

### 4.3.3.2. The $K$ -band Luminosity Function

Model predictions for the rest-frame  $K$ -band LF should, in principle, be more robust than predictions for the rest-frame  $B$ -band, because the effects of our uncertain dust modelling are then much weaker. On the other hand, observational determinations of the LF at rest-frame  $K$  are more uncertain than at rest-frame  $B$ , because the magnitudes of high redshift galaxies must then be inferred by extrapolation beyond the wavelength region directly measured, rather than interpolated between the observed bands. This situation is improving rapidly as deep data at wavelengths beyond  $2\mu$  become available from *Spitzer*.

As can be seen in Fig. 4.5, our predictions for the evolution of the rest-frame  $K$ -band LF show the same behaviour as for the  $B$ -band. The local result from [Cole et al. \(2001\)](#) is reproduced well, as illustrated in the upper left panel and already demonstrated in [Croton et al. \(2006\)](#). The observed  $z = 0$  function is reproduced as a thin red line in the other panels in order to make the amount of evolution more apparent. At higher redshifts we compare with observational determinations from [Pozzetti et al. \(2003\)](#) for the 52 arcmin<sup>2</sup> of the K20 survey, from [Feulner et al. \(2003\)](#) for the 600 arcmin<sup>2</sup> of the MUNICS sample and from [Saracco et al. \(2006\)](#) for a 5.5 arcmin<sup>2</sup> area in the HDF-S. In these plots we give error bars as quoted by the original papers, but we note that these are based on counting statistics only and additional uncertainties are expected due to clustering, particularly for the smaller fields. Furthermore, photo- $z$ 's are used for a significant number of galaxies in these determinations which may lead to additional systematic uncertainties in the results. Given the scatter between the various observational determinations, the disagreements between model and data do not look particularly serious. The models do appear to overpredict the abundance of galaxies near the knee of the luminosity function, perhaps by a factor of 2 at the highest redshift, echoing the discrepancies found above when comparing with  $K$ -band galaxy counts and redshift distributions.

### 4.3.3.3. Evolution of Luminosity Function parameters

In order to display the evolution of the luminosity function in our models more effectively, we have fit Schechter (1976) functions to the simulation data for the rest-frame  $B$  and  $K$ -bands at every stored output time. In most cases these functions are a good enough fit to give a fair representation of the numerical results. In Fig. 4.6 we plot the evolution with redshift of the parameters  $\Phi^*$  and  $M^*$  and of the volume luminosity density,  $j = \Phi^* L^* \Gamma(\alpha + 2)$  using thick solid lines, and we compare with fits to observational data. For each observational point in the  $K$ -band panels we indicate the (often broad) redshift range to which it refers by a horizontal bar. The vertical bar indicates the uncertainty quoted by the original authors.

Not surprisingly, the results of the last section are confirmed. For the model  $\Phi^*$

#### 4. High redshift galaxies

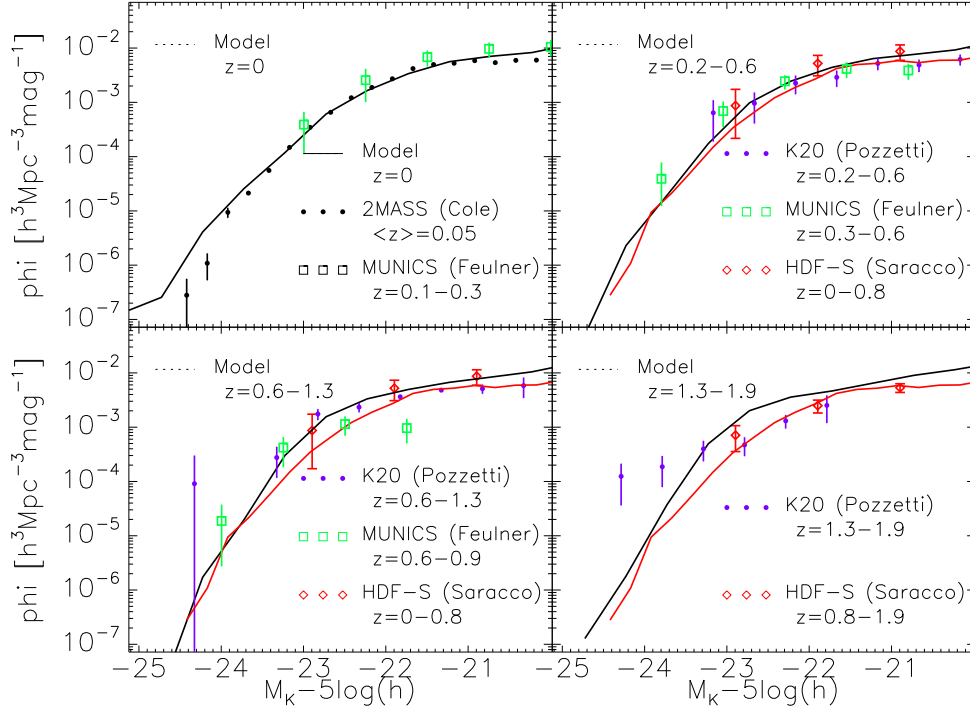


Figure 4.5.: Comparison of the evolution predicted for the rest-frame  $K$ -band LF to observational determinations from [Cole et al. \(2001\)](#) at low  $z$  (upper left panel, repeated as a thin red line in the other panels) and from [Pozzetti et al. \(2003\)](#), [Feulner et al. \(2003\)](#) and [Saracco et al. \(2006\)](#) at higher redshifts.

increases slightly with redshift out to about  $z = 1.5$ , whereas the observations imply a relatively steep decline over this same redshift range. This holds for both photometric bands. For  $M^*$  we see brightening both in the models and in the observations, but the effect is more pronounced in the latter. In  $K$  the models predict  $M^*$  to be almost independent of redshift. Derivations of  $\Phi^*$  and  $M^*$  from observational data using maximum likelihood techniques usually give results where the errors in the two quantities correlate in a direction almost parallel to lines of constant luminosity density. For this reason we expect  $j$  to be more robustly determined from the data than either  $\Phi^*$  or  $M^*$  individually. It is interesting that the apparent deviations between data and model for  $\Phi^*$  and  $M^*$  largely compensate, so that the model predicts an evolution of  $j$  which is quite similar to that inferred from the observations. This is particularly striking at rest-frame  $B$ . At rest-frame  $K$  the observational error



bars are still too large to draw firm conclusions, but a non-evolving luminosity density represents the data somewhat better than does our model, again confirming the conclusions we drew in earlier sections.

#### 4.3.4. The evolution of the stellar mass function

The evolution of the abundance of galaxies as a function of their stellar mass is one of the most direct predictions of galaxy formation models. It depends on the treatment of gas cooling, star-formation and feedback, but not directly on the luminous properties of the stars or on the dust modelling. (There remains an indirect dependence on the latter since observations of galaxy luminosities are typically used to set uncertain efficiency parameters in the modelling.) The stellar masses of galaxies can also be inferred relatively robustly from observational data provided sufficient observational information is available (e.g. [Bell & de Jong 2001](#); [Kauffmann et al. 2003](#)). At high redshift, however, such inferences become very uncertain unless data at wavelengths beyond  $2\mu$  are available (e.g. from *Spitzer*). The observationally inferred masses also depend systematically on the assumed Initial Mass Function for star formation (usually taken to be universal) and it is important to ensure that consistent assumptions about the IMF are made when comparing observation and theory.

Bearing in mind these caveats, Fig. 4.7 compares the mass functions predicted by our model to local data from [Cole et al. \(2001\)](#) as well as to high-redshift estimates from [Drory et al. \(2005\)](#), based on the MUNICS survey, and from [Fontana et al. \(2006\)](#) based on the MUSIC-GOODS data. The latter study uses data in the  $3.6$  to  $8\mu$  bands from *Spitzer* to constrain the spectral energy distributions of the galaxies and so should give substantially more reliable results at high redshift than the former. In Fig. 4.7 the model mass functions at  $z > 0$  are shown both before and after convolution with a Gaussian in  $\log M_*$  with standard deviation  $0.25$ . This is intended to represent the uncertainty in the observational determinations of stellar mass. This error may be appropriate for the MUSIC-GOODS sample at all redshifts, but it is certainly too small to represent uncertainties in the MUNICS mass estimates at high redshift. We note that such errors weaken the apparent strength of the quasi-exponential cut-off at high masses. We neglect their effects at  $z = 0$ .

Our model is nicely consistent with the observed mass function in the local Universe, but it clearly overpredicts the abundance of galaxies at redshifts between 1 and 3. The observed evolution relative to the  $z = 0$  function (indicated by the dashed line in each of the higher redshift panels) is strong, while the model prediction is rather more modest. In the stellar mass range  $10^{10}$  to  $10^{11} M_\odot$  where the observational estimates appear most reliable the overprediction reaches a factor of about 2 at  $z = 2$ . This is nicely consistent with the conclusions we reached in earlier sections based on number counts, redshift distributions and luminosity functions, but unfortunately the scatter between the various observational determinations is large enough to prevent

## 4. High redshift galaxies

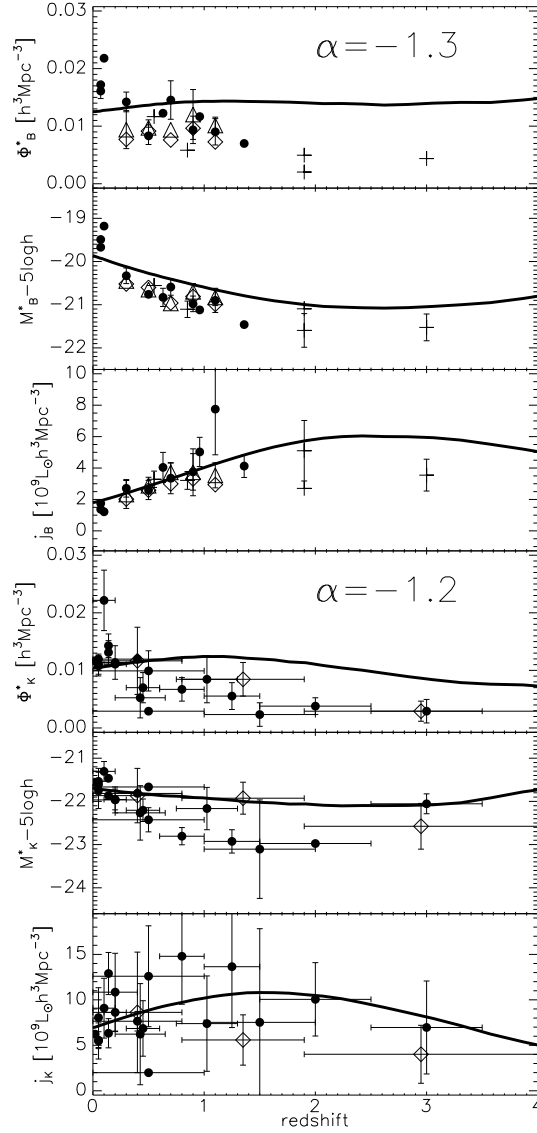


Figure 4.6.: The evolution of the  $\Phi^*$  and  $M^*$  parameters of Schechter (1976) fits to luminosity functions in rest-frame  $B$  and  $K$  (with  $\alpha$  held constant at the values indicated). We also show the evolution of the total luminosity density  $j$  inferred from these parameters. In each panel the solid line denotes the model prediction and the symbols are data from different sources (with potentially different  $\alpha$ ). The  $B$  band data comprises observations from Poli et al. (2003, + symbols) and Faber et al. (2005, diamonds), who also provide a compilation from the literature (filled circles), whereas the  $K$  band data are observations (diamonds) and a literature compilation (filled circles) from Saracco et al. (2006).

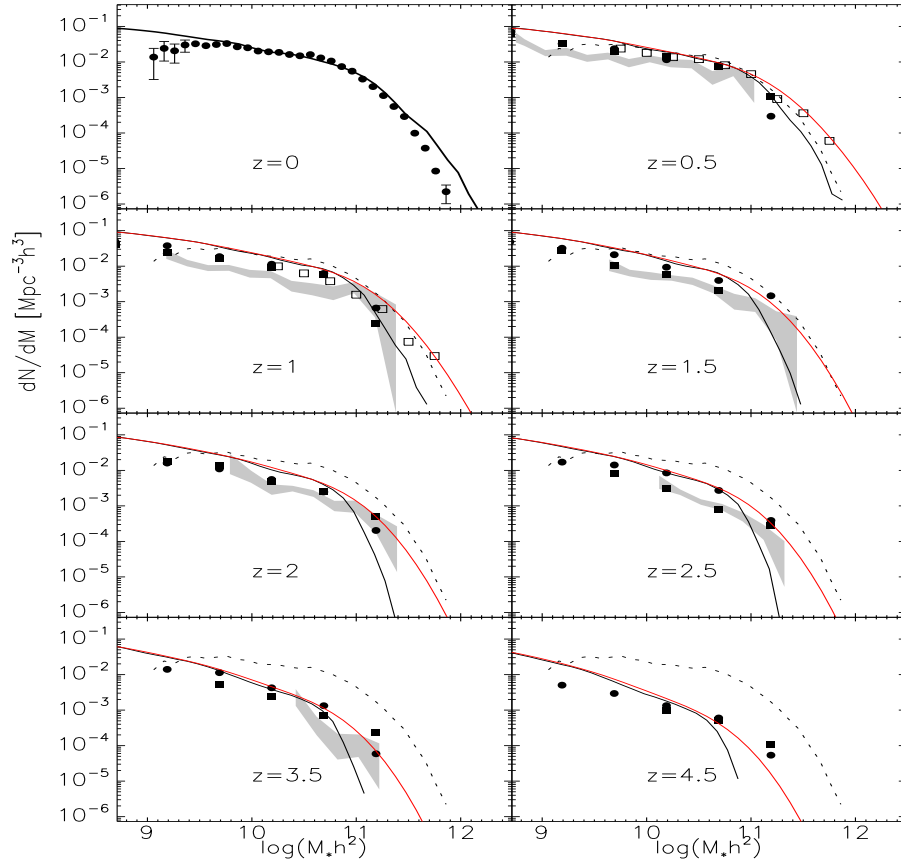


Figure 4.7.: Evolution of the stellar mass function in the redshift range  $z = 0 - 4.5$ . Local data are from [Cole et al. \(2001\)](#) and are repeated as a black dashed line in the higher redshift panels. High redshift data are taken from [Drory et al. \(2005, symbols\)](#) and [Fontana et al. \(2006, grey shaded areas\)](#). Model predictions are shown both with (red) and without (black) convolution with a normal distribution of standard deviation 0.25 representing measurement errors in  $\log M_*$ . At  $z = 0$  we consider the mass determinations precise enough to neglect this effect.

any firm conclusion.

## 4. High redshift galaxies

---

### 4.3.5. The evolution of the colour-magnitude relation

Recent studies of the high redshift galaxy population have often stressed the presence of massive objects with colours similar to those expected for fully formed and passively evolving ellipticals (e.g. [Renzi 2006](#), and references therein). This is usually presented as a potential problem for “hierarchical” models of galaxy formation where star formation and merging continue to play a major role in the build up of galaxies even at recent times. In order to illustrate how these processes are reflected in the colours and magnitudes of galaxies in our simulation, we show in Fig. 4.8 the colour-magnitude diagram for 10000 galaxies randomly sampled from a  $2.5 \times 10^5 h^{-3} \text{Mpc}^3$  volume at redshifts  $z = 0, 1, 2$  and  $3$ . At  $z = 0$  the well-known bi-modal distribution of colours is very evident. A tight red-sequence of passively evolving objects is present with a slope reflecting a relation between mass and metallicity. There is also a “blue cloud” of star-forming systems. A success of the model emphasised by [Croton et al. \(2006\)](#) is the fact that the brightest galaxies all lie on the red sequence at  $z = 0$ . This is a consequence of including a treatment of “radio feedback” from AGN.

To allow better appreciation of the evolution to high redshift, we also show logarithmically spaced contours of the colour-magnitude distribution of all galaxies in a  $1.5 \times 10^7 h^{-3} \text{Mpc}^3$  volume as black contours in the panels of Fig. 4.8. The bluing of the upper envelope with increasing redshift is very clear and is consistent with passive evolution of the red sequence. We illustrate this by fitting a population synthesis model to the ridge line of the  $z = 0$  red sequence, assuming a single burst of star formation at  $z = 6$  and a metallicity which varies with stellar mass. This model is shown as a red line not only at  $z = 0$  (where it was fit) but also at the earlier redshifts. Notice that although there are galaxies with red sequence colours at all redshifts, the sequence becomes less and less well-defined at earlier times, with a substantial number of objects appearing *redder* than the passively evolving systems. These are compact, gas- and metal-rich galaxies where our model predicts very substantial amounts of reddening. Recent surveys of distant Extremely Red Objects have found substantial numbers of such systems ([Cimatti et al. 2002a, 2003](#); [Le Fèvre et al. 2005](#); [Kong et al. 2006](#)), but it remains to be seen if our model can account quantitatively for their properties.

The colours of galaxies in the blue cloud also become bluer at high redshift. This is a consequence of an increase in the typical ratio of current to past average star formation rate in these galaxies. The difference between star-forming systems and “true” red-sequence galaxies becomes blurred at high redshift in our model because of the increasingly important effects of dust.

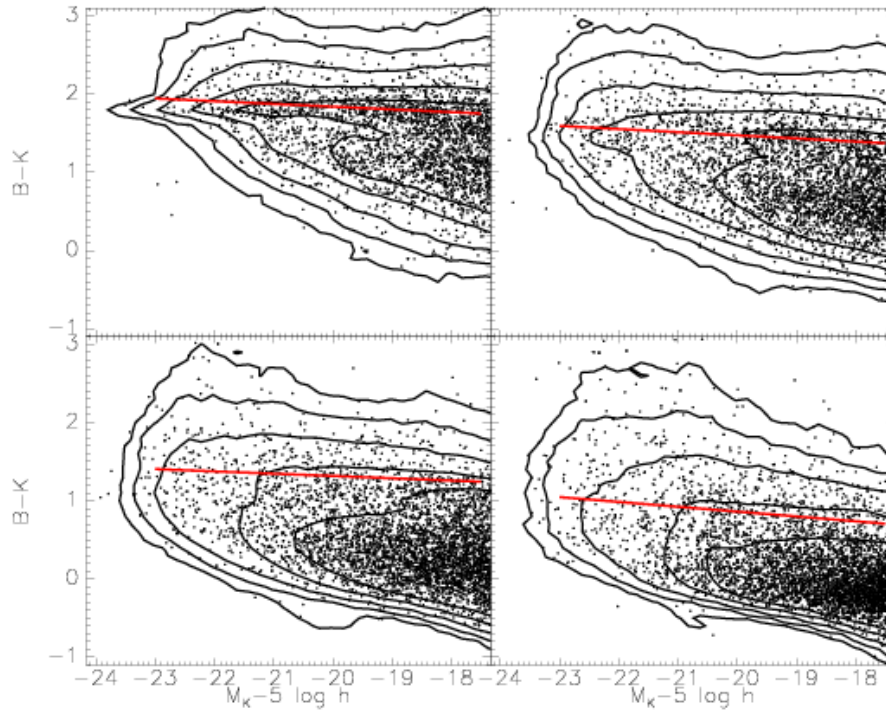


Figure 4.8.: Evolution of the colour-magnitude distribution of galaxies in rest-frame  $B$  and  $K$  over the redshift range  $z = [0, 3]$ . Randomly selected 10000 galaxies in a  $2.5 \times 10^5 h^{-3} \text{Mpc}^3$  volume of the simulation are plotted in each panel. For comparison purposes the distribution of a much larger sample in a  $1.5 \times 10^7 h^{-3} \text{Mpc}^3$  volume is indicated as logarithmically spaced contours. The red solid line indicates the colour magnitude relation predicted for stellar populations formed in a single burst at  $z = 6$  and evolving passively thereafter. The metallicity of the populations has been adjusted as a function of stellar mass to fit the ridge line of the  $z = 0$  red sequence.

## 4.4. Discussion and Conclusions

The model we have used in this paper is that of [Springel et al. \(2005\)](#) and [Croton et al. \(2006\)](#) and as updated by [De Lucia & Blaizot \(2007\)](#) and made public through the Millennium Simulation download site (see [Lemson et al. 2006](#)). Earlier work has compared this model to a wide range of properties of low redshift galaxies: their luminosity functions, their bi-modal luminosity-colour-morphology distribution and

## 4. High redshift galaxies

---

their Tully-Fisher relation (Croton et al. 2006); their spatial clustering as inferred from two-point correlations (Springel et al. 2005; Li et al. 2006; Meyer et al. 2007) and from fits to halo occupation distribution models (Wang et al. 2006; Weinmann et al. 2006); their HI gas content (Meyer et al. 2007); and their assembly histories within clusters (De Lucia et al. 2006; De Lucia & Blaizot 2007). Although Croton et al. (2006) compared the evolution of the global star formation rate and the global black hole accretion rate of the model to observation, the current paper is the first to compare its predictions in detail with observations of high redshift galaxies.

Our comparison to galaxy counts, to redshift distributions and to observational estimates of luminosity and mass functions at high redshift paints a consistent picture despite large statistical uncertainties and some significant technical issues. Our model appears to have too many relatively massive galaxies at high redshift and these galaxies appear to be too red. Thus, while we fit optical galaxy counts well up to densities of 30 gal/mag/arcmin<sup>2</sup>, we start to overpredict numbers in the  $K$  band at densities above about 3 gal/mag/arcmin<sup>2</sup>. This overabundance of apparently red galaxies shows up in the redshift distributions as an overprediction of the number of galaxies with  $K \sim 23$  to 25 at redshift between about 1 and 3. These correspond to moderately massive systems near the knee of the luminosity function, and indeed, while our rest-frame  $B$  luminosity functions appear compatible with observation out to  $z \sim 1$ , at rest-frame  $K$  our luminosity functions are noticeably high beyond  $z = 0.5$  except possibly for the brightest objects. The problem shows up most clearly in our mass functions which overpredict observationally estimated abundances by about a factor of 2 at  $z = 2$ . Apparently the mass function of galaxies evolved more strongly in the real Universe than in our simulation.

A galaxy formation model with similar basic ingredients to ours, but with important differences of detail has been independently implemented on the Millennium Simulation by Bower et al. (2006). This model is also publicly available at the download site. It fits low redshift galaxy luminosity functions as well as our model, but the comparisons which Bower et al. (2006) show to high-redshift luminosity and mass function data (essentially the same datasets we use here) demonstrate somewhat better agreement than we find in this paper. In the mass range  $10^{10} < h^2 M_*/M_\odot < 10^{11}$  the abundances predicted by their model are lower than ours by about 20% at  $z = 1$  and by about 30% at both  $z = 2$  and  $z = 3.5$ , despite the fact that at  $z = 0$  the two models agree very well. This is consistent with the fact that their model forms 20% of all its stars by  $z = 3.2$  and 50% by  $z = 1.65$  whereas the corresponding redshifts for our model are  $z = 3.6$  and  $z = 1.9$ . These differences arise from details of the star formation and feedback models adopted in the two cases.

In summary, both the Bower et al. (2006) simulation and our own are consistent with most current faint galaxy data. Thus there seems no difficulty in reconciling the observed properties of distant objects with hierarchical galaxy formation.

#### 4.4. Discussion and Conclusions

---

The fact that predictions from the two simulations differ at a level which can be marginally separated by the observations, means that currently accessible properties of distant galaxies can significantly constrain models of this type, and hence the detailed physics which controls the formation and the observable properties of galaxies. The fact that the model we test here apparently *overpredicts* the abundance of moderately massive galaxies at high redshift, despite the fact that late merging plays a major role in the build-up of its more massive galaxies (e.g. De Lucia et al. 2006; De Lucia & Blaizot 2007), demonstrates that current data are still far from constraining the importance of this process. As the data improve, the models will have to improve also to remain consistent with them. This interplay between theory and observation should eventually lead to a more convincing and more complete picture of how galaxies came to take their present forms.

**Acknowledgements:** We thank Jeremy Blaizot, Darren Croton and Gabriella De Lucia for useful discussions of a number of technical issues which arose during this project. Moreover we thank the anonymous referee whose comments helped to improve this paper. MGK acknowledges a PhD fellowship from the International Max Planck Research School in Astrophysics, and support from a Marie Curie Host Fellowship for Early Stage Research Training.

#### 4. High redshift galaxies

---



*There is a theory which states that if anybody ever discovers exactly what the Universe is for and why it is here, it will instantly disappear and be replaced by something even more bizarre and inexplicable.*

— The Hitchhiker’s Guide to the Galaxy

# 5

## Deriving the cosmic history of galaxy mergers from observing close galaxy pairs – a semi-analytic study

M. G. Kitzbichler & S. D. M. White

*Max-Planck Institut für Astrophysik, Karl-Schwarzschild-Straße 1, D-85748 Garching b. München, Germany*

### Abstract

We make use of the Millennium run, a very large N-body simulation of dark-matter evolution in a cosmological volume, in combination with a semi-analytic model for galaxy formation to explore the relationship between the evolution of the galaxy merger rate and observed close pairs of galaxies. First we show that galaxy merger rate evolution is different from the DM halo merger rate evolution which has an intrinsic slope of  $\sim (1+z)^{3/2}$  for all masses whereas for galaxies it is rather flat and depends on mass. We give an explanation for this discrepancy also found by other authors, and we follow their conclusion that the study of galaxy merger rates is more suitable as a means to understand galaxy physics than as a probe of cosmic structure formation. Subsequently we utilise the available semi-analytic catalogue in the full simulation box to produce a mock observation of our simulated galaxies, which is done by tracing the backward lightcone along the line-of-sight of an imaginary observer through the box out to high redshifts. This allows us to test our pair identification method on realistically selected galaxy pairs on the plane of the sky, subject to an apparent magnitude cut, and including accurate k-corrections, lu-

## 5. Galaxy pairs

---

minosity evolution, and peculiar velocities. Additionally we explore the effect of large redshift uncertainties that are inherent in photometric redshift catalogues, and show that after applying a simple correction for random pairs, these can still be used for close pair studies, albeit with larger error bars.

As the most important result of this work we derive a calibrating average timescale  $\langle T_{\text{Merge}} \rangle$  on which the binary galaxies can be assumed to merge, by comparing the intrinsic merger rate to the pair counts in our simulation, where we take into account mass and redshift dependence as well as different pair selection criteria. We find that  $\langle T_{\text{Merge}} \rangle$  is considerably larger for all masses and redshifts than what has been typically assumed in the majority of pair studies to date. Finally we demonstrate that our average merging timescale  $\langle T_{\text{Merge}} \rangle$  is consistent with the distribution of intrinsic merging times of individual galaxies in the mock catalogue, and establish that it can be used as an accurate calibration, allowing a simple and straightforward calculation of the instantaneous galaxy merger rate from the number of observed galaxy pairs at a given redshift.

**Key words:** galaxies: general – galaxies: formation – galaxies: evolution  
galaxies: interactions – galaxies: statistics

### 5.1. Introduction

Ever since the pioneering work of [Holmberg \(1937\)](#) the study of close pairs of galaxies was considered to be a promising tool to understand galaxy properties. Where at first the interest was primarily directed at finding possible differences in the average properties such as luminosity, colour, and morphology, it was also recognised that such a dynamical system can give important clues of galaxy masses (e.g. [Page 1952](#)). Even more importantly they were the natural key to understanding the back then speculative merging of galaxies, first simulated as the coalescence of two spiral galaxies in the now famous work of [Toomre & Toomre \(1972\)](#). Subsequently when it became clear that galaxy mergers are real and in fact quite common (as already advocated by [Toomre 1977](#)), they were in turn seen as an important means to understand cosmological structure formation. Evidence for a bottom up scenario was mounting in the second half of the 1980's when the CDM model started to gain wider acceptance and the merging of two small galaxies into a bigger one was a cornerstone of the hierarchical picture. Therefore the evolution of galaxy mergers with redshift was also on the top of the list of properties that a possible cosmological model would have to predict correctly in order to be accepted. However it turned out that a quantitative determination of the merger rate as a function of redshift is a difficult task subject to a range of systematic uncertainties.

There have been a number of studies in which close pairs of galaxies have been used to measure evolution in the galaxy merger rate ([Zepf & Koo 1989](#); [Burkey](#)

et al. 1994; Woods et al. 1995; Patton et al. 1997; Le Fèvre et al. 2000). The usual assumption is that a given observed pair of galaxies will merge on a rather short timescale, if it satisfies certain conditions that indicate that it is a true physical pair and dynamically bound. Unfortunately studies using this method have yielded a wide variety of results. Some of the diversity has been attributed to differences in pair definitions and techniques, and in most cases, the error bars have been quite large, therefore significant discrepancies remain.

Another technique having become popular more recently is the identification of mergers a posteriori through the typical morphological perturbation of merger remnants. The obvious advantage is that here one doesn't have to make any assumption about the future merger of an observed galaxy pair, instead the merger can be taken as a fact. On the other hand one still has to assume a timescale on which the disturbed morphology will be visible. Also this method requires very high resolution high signal-to-noise observations of the non-local universe and has therefore become possible only in the last decade with the advent of the age of space-borne observatories.

Interestingly the most recent attempts to determine the merger rate with either of these methods (Lin et al. 2004; Lotz et al. 2006; Bell et al. 2006) are indicating that the evolution with redshift is much shallower than was previously assumed on the basis of theoretical models of dark-matter halo mergers, using both analytical and numerical techniques (e.g. Lacey & Cole 1993; Khochfar & Burkert 2001). Berrier et al. (2006) gave an explanation for this apparent discrepancy based on halo-occupation-distribution (HOD) models of galaxy formation and evolution and conclude that the galaxy merger rate is not a good probe of the dark-matter halo merger rate but rather of the mechanisms shaping galaxies.

Independent of these many aspects of the topic, in this work we aim mainly at investigating whether the intrinsic galaxy merger rate as we derive it from a semi-analytic galaxy formation model can be recovered reliably from counting close pairs in a realistic mock observation of this simulation. The crucial parameter required for such a conversion is the average timescale on which galaxy pairs merge. This timescale has been one of the main sources of the large uncertainties in most previous pair studies because it was either simply estimated to be around 500 Myr or based on the numerical simulation of a small number of individual systems. Here we make use of the enormous statistical power of the Millennium Simulation comprising 800 million DM haloes and even more galaxies at all redshifts to get a reliable average result for this important calibrating timescale.

This paper is organised as follows. In Section 5.2 we briefly describe the Millennium Run N-body simulation and the semi-analytic model we are adopting here which is based on the fiducial model of Croton et al. (2006) as modified by De Lucia & Blaizot (2007) and extended by Kitzbichler & White (2007). We describe the treatment of galaxy mergers in the simulation and the connection between close galaxy

## 5. Galaxy pairs

---

pairs and mergers. Furthermore we contrast the evolution of the fiducial dark-matter merger rate to the galaxy merger rate. Subsequently Section 5.3 will explain the techniques used to find the sample of close pairs and to correct for the contribution from random pairs. In Section 5.4 we find a calibrating average timescale to convert the pair counts from the mock catalogue to a merger rate. Finally the results are briefly summarised in Section 5.5.

### 5.2. Model

#### 5.2.1. The Millennium N-body simulation

We make use of the Millennium Run, a very large simulation which follows the hierarchical growth of dark matter structures from redshift  $z = 127$  to the present. The simulation assumes the concordance  $\Lambda$ CDM cosmology and follows the trajectories of  $2160^3 \simeq 1.0078 \times 10^{10}$  particles in a periodic box  $500 \text{ Mpc}/h$  on a side which could be achieved using a special version of the GADGET-2 code (Springel et al. 2001b; Springel 2005). A full description is given by Springel et al. (2005); here we summarise the main simulation characteristics as follows:

The adopted cosmological parameter values are consistent with a combined analysis of the 2dFGRS (Colless et al. 2001) and the first-year WMAP data (Spergel et al. 2003; Seljak et al. 2005). Specifically, the simulation takes  $\Omega_m = \Omega_{\text{dm}} + \Omega_b = 0.25$ ,  $\Omega_b = 0.045$ ,  $h = 0.73$ ,  $\Omega_\Lambda = 0.75$ ,  $n = 1$ , and  $\sigma_8 = 0.9$  where all parameters are defined in the standard way. The adopted particle number and simulation volume imply a particle mass of  $8.6 \times 10^8 h^{-1} M_\odot$ . This mass resolution is sufficient to resolve the haloes hosting galaxies as faint as  $0.1 L_\star$  with at least  $\sim 100$  particles. The short-range gravitational force law is softened on a comoving scale of  $5 h^{-1} \text{ kpc}$  which may be taken as the spatial resolution limit of the calculation, thus achieving a dynamic range of  $10^5$  in 3D. Data from the simulation were stored at 63 epochs spaced approximately logarithmically in time at early times and approximately linearly in time at late times (with  $\Delta t \sim 300 \text{ Myr}$ ). Post-processing software identified all resolved dark haloes and their subhaloes in each of these outputs and then linked them together between neighbouring outputs to construct a detailed formation tree for every object present at the final time. In principle one could already study the merger rate evolution of dark matter haloes of a given mass solely based on this halo merger tree. However since we want to compare to the observed merger rates of galaxies subject to properties of the visible matter we have to carry our model at least one step further and assign stellar masses and luminosities to the haloes. This galaxy formation modelling is carried out in post-processing on the stored halo merger tree by applying semi-analytic recipes as described in the following section.

### 5.2.2. The semi-analytic model

Our semi-analytic model is that of [Croton et al. \(2006\)](#) as updated by [De Lucia & Blaizot \(2007\)](#) and made public on the Millennium Simulation data download site<sup>1</sup>. These models include the physical processes and modelling techniques originally introduced by [White & Frenk \(1991\)](#); [Kauffmann et al. \(1993\)](#); [Kauffmann & Charlot \(1998\)](#); [Kauffmann et al. \(1999\)](#); [Kauffmann & Haehnelt \(2000\)](#); [Springel et al. \(2001a\)](#) and [De Lucia et al. \(2004\)](#), principally gas cooling, star formation, chemical and hydrodynamic feedback from supernovae, stellar population synthesis modelling of photometric evolution and growth of supermassive black holes by accretion and merging. They also include a treatment (based on that of [Kravtsov et al. 2004](#)) of the suppression of infall onto dwarf galaxies as consequence of reionisation heating. More importantly, they include an entirely new treatment of “radio mode” feedback from galaxies at the centres of groups and clusters containing a static hot gas atmosphere. The equations specifying the various aspects of the model and the specific parameter choices made are listed in [Croton et al. \(2006\)](#) and [De Lucia & Blaizot \(2007\)](#). The only change made here is in the dust model as described in [Kitzbichler & White \(2007\)](#).

It should be pointed out here that most of the assumptions made for the semi-analytic model enter only in an indirect way into the merger rate study we present here, by the virtue of selection effects. The underlying merger rate of dark matter haloes, which is the principal quantity governing the galaxy merger rate, is not changed in any way by semi-analytic recipes. The fate of its host dark matter halo in the halo merger tree determines for every galaxy the central galaxy it is ultimately going to merge with. Only the merger doesn’t occur instantaneously, but the timescale for the two galaxies to spiral in to each other is derived from a dynamical friction argument ([Binney & Tremaine 1987](#)), and thus assumed to be:

$$t_{\text{friction}} = 1.17 \frac{V_{\text{vir}} r_{\text{sat}}^2}{G m_{\text{sat}} \ln \Lambda}, \quad (5.1)$$

where  $m_{\text{sat}}$  and  $r_{\text{sat}}$  are the satellite halo mass and cluster centric radial distance respectively and the Coulomb logarithm is approximated by  $\ln \Lambda = \ln(1 + M_{\text{vir}}/m_{\text{sat}})$ . This modification to the merger tree of galaxies with respect to the merger tree of haloes is necessary since we can identify dark-matter haloes only down to a certain mass threshold. A limitation that becomes particularly important for sub-haloes, i.e. satellites, within larger host haloes, because they have to be found as a density excess against the background density of their host halo. Depending on the masses of the host and the satellite at a certain radius with respect to the host halo centre the sub-halo finding algorithm will lose track of a sub-halo because its density profile becomes too shallow compared to the one of the background halo and thus it will be

<sup>1</sup><http://www.mpa-garching.mpg.de/millennium>; see [Lemson et al. \(2006\)](#)

## 5. Galaxy pairs

---

counted as having been disrupted. However, this radius is typically  $R \geq 1/10 R_{\text{vir}}$  even for very massive satellites and thus much further out than the radius at which the actual merger of the galaxies (i.e. the baryonic component) sitting in the centres of their halos will finally occur. Therefore in the semi-analytic model we do not merge the galaxies at that time but count down the merging time starting at  $t_{\text{friction}}$ . During this period in which the satellite galaxy has neither a dark matter halo nor sub-halo associated with it we assign it the position and velocity of the most bound particle from the last identified sub-halo it had.

Further justification for this treatment can be found by comparing the correlation functions of galaxies in the simulation to the observed ones at small scales  $r_p < 100 \text{ kpc}/h$ . Such a test is presented in Fig. 5.1, which shows the projected 2-point correlation function  $w_p(r_p)$  in different stellar mass bins compared to the observed one derived from the SDSS survey by Li et al. (2006). The solid black lines denote results from the simulation including all galaxies whereas the dotted line includes only galaxies that have an actual dark-matter halo, which is equivalent to a model with instantaneous merging where  $t_{\text{fric}} = 0$ . Clearly the observations could not be fitted with this assumption, especially for low-mass galaxies, where  $w_p(r_p)$  would be underpredicted by at least a factor of 5 at scales below  $r_p < 100 \text{ kpc}/h$ . We can now be confident that the pair counts we are getting from our simulation are realistic since  $n_{\text{Pairs}}$ , the spatial pair density corrected for random pairs, is straightforwardly connected to  $w_p(r_p)$  through the integral

$$n_{\text{Pairs}}(r_p) = 2\pi n^2 \int_0^{r_p} w_p(r) r dr \quad (5.2)$$

where  $n$  is the overall mean galaxy density and  $r_p$  is the limiting radius out to which we are counting pairs.

### 5.2.3. Merger rates and pair counts

Clearly an accurate treatment of galaxy merging is crucial for the study performed in this work since it relies on the assumption that merging galaxies are spatially and kinematically close to each other. On the other hand, it should be emphasised once more that the overall merger rate evolution found for the galaxies is still dominantly governed by the underlying merger tree of the dark matter halos which is directly determined from the Millennium N-body simulation. The semi-analytic treatment of the final stages of the merger applying Eqn. 5.1 is in effect only a convolution of this dark-matter merger rate with the characteristic merging time distribution of galaxy pairs of different masses:

$$\dot{N}_{\text{Galaxies}}(t) = \int_0^\infty \dot{N}_{\text{DM}}(t - t_{\text{fric}}) P(t_{\text{fric}}) dt_{\text{fric}}, \quad (5.3)$$

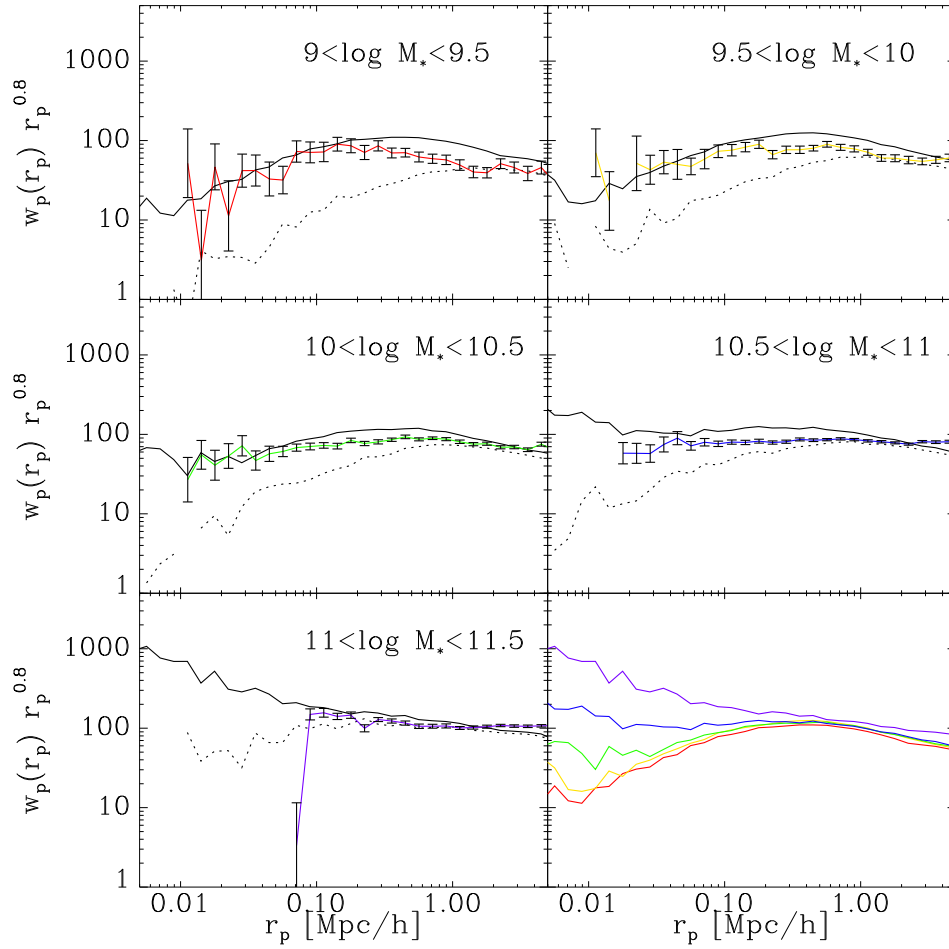


Figure 5.1.: Projected 2-point correlation function  $w_p(r_p)$  for different mass ranges with (solid) and without (dashed) galaxies that have no DM halo. The curves have been normalised to a fiducial of  $w_p(r_p) \propto r_p^{0.8}$ . In the bottom right panel all mass ranges are plotted on top of each other with masses increasing with colour from red to purple. The symbols with error bars are data from the SDSS survey taken from [Li et al. \(2006\)](#).

where  $\dot{N}$  denotes the respective merger rates,  $t_{\text{fric}}$  is the dynamical friction timescale from Eqn. 5.1, and  $P(t_{\text{fric}})$  is the intrinsic distribution of merging times. Furthermore the population of galaxy pairs is growing from halo mergers and depopulated by

## 5. Galaxy pairs

---

galaxy mergers, hence we can write:

$$\dot{N}_{\text{Pairs}}(t) = \dot{N}_{\text{DM}}(t) - \dot{N}_{\text{Galaxies}}(t). \quad (5.4)$$

Choosing the most simple merger time distribution, a fixed value  $T$  for all galaxies, we can write  $P(t_{\text{fric}}) = \delta(t_{\text{fric}} - T)$  such that Eqn. 5.3 becomes

$$\dot{N}_{\text{Galaxies}}(t) = \dot{N}_{\text{DM}}(t - T) \quad (5.5)$$

which translates to a simple time delay of the galaxy merger rate with respect to the DM merger rate. Assuming that  $T$  is small we expand this to

$$\dot{N}_{\text{Galaxies}}(t) = \dot{N}_{\text{DM}}(t) - T \frac{d}{dt} \dot{N}_{\text{DM}}(t). \quad (5.6)$$

Inserting into Eqn. 5.4 and performing the integral yields:

$$N_{\text{Pairs}}(t) = \int_0^t T \frac{d}{dt} \dot{N}_{\text{DM}}(t) dt = T \dot{N}_{\text{DM}}(t), \quad (5.7)$$

which is the expected result that firstly the number of pairs is indeed a measure of the underlying merger rate and secondly that one will observe the more pairs the longer the merging process takes. The second relation has to be calibrated thoroughly in order to make use of the first one, and since in reality the merging time is not a delta function but has an actual distribution, one has to be careful. Many observational studies assume that this distribution is rather narrow, typically a width of about  $500 \text{ Myr}/h$  is adopted for a pair sample with projected separations below  $30 \text{ kpc}/h$ . As we will see in Section 5.4.4 of this paper, such a choice may lead to an overestimation of the merger rate

### 5.2.4. Fiducial merger rates of DM haloes and galaxies

At this point, having a semi-analytic catalogue of galaxies at several cosmic times, one can straightforwardly test the assumption that galaxy and DM halo merger rates differ only in a moderate time delay as derived in Eqn. 5.5. To this end Fig. 5.2 shows the redshift evolution of major galaxy mergers with mass ratios greater than 4:1 and a given lower limit in stellar mass (black), compared to the rate at which such galaxies would merge if  $t_{\text{fric}}$  was zero (green). This latter quantity is identical to the DM halo disruption rate extracted from the Millennium simulation and depends on the semi-analytic model only through the stellar mass cut and ratio. Additionally the rate at which major satellite galaxies are produced is shown as well (red line). In our simulation where we follow substructure, this is the rate at which independent DM haloes are turned into sub-haloes within a bigger halo and thus corresponds to the fiducial halo merger rate as it is usually defined.



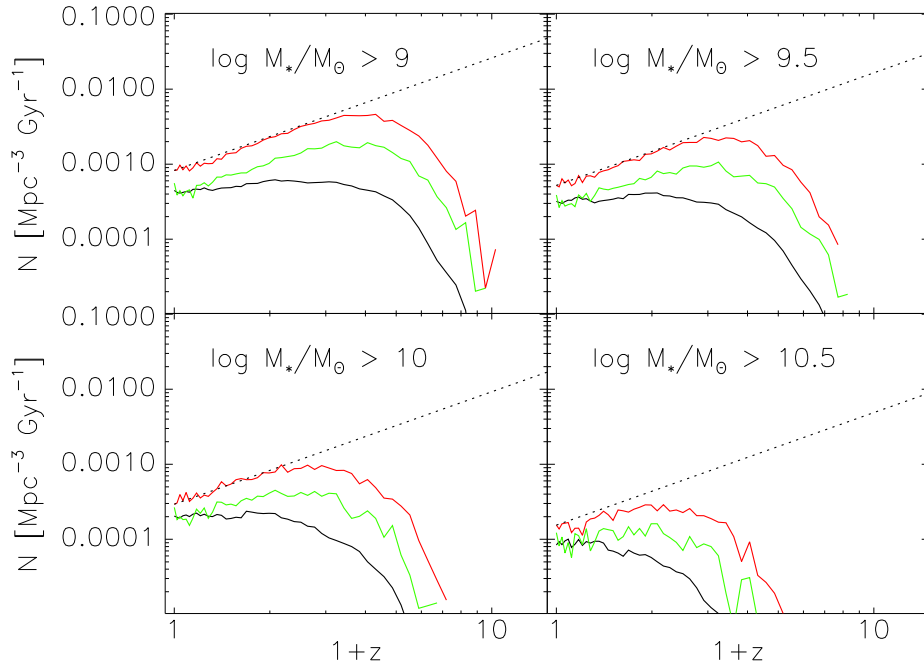


Figure 5.2.: Redshift evolution of major galaxy mergers with a given lower limit in stellar mass compared the rate at which major satellite galaxies are produced (red) and to the rate at which these satellites' DM haloes are disrupted (green). The dotted line indicates a slope of  $(1+z)^{-1.5}$  in order to guide the eye.

What is apparent at first sight is that the merger rate peaks at an earlier redshift for smaller objects. The obvious reason for this behaviour is that in a hierarchically growing universe, as we have simulated it here, more massive objects form later, and the merger rate is proportional to the square of the abundance of the source populations. An analytical treatment of the dependence of the merger rate evolution on mass is the derivation of [Lacey & Cole \(1993\)](#) who find exactly such a behaviour, however only considering dark matter halos, based on the excursion set formalism (see [Press & Schechter 1974](#); [Bond et al. 1991](#)). It is therefore interesting to note that even though their prediction for *DM haloes* agrees with the results from the Millennium simulation, the *galaxy* merger rate evolution has a slope that depends on stellar mass contrary to the DM merger rate. In effect for typical major merger mass ranges of  $M_* > 10^{10} M_\odot/h$  the galaxy merger rate is constant out to  $z = 1$ . This was

## 5. Galaxy pairs

---

also found by [Lin et al. \(2004\)](#) and [Lotz et al. \(2006\)](#) observationally, which seemed to be a contradiction to theoretically and semi-analytically predicted DM halo merger rates, as pointed out by [Berrier et al. \(2006\)](#), who tried to explain this result in the context of a HOD model. They attribute it to a lower halo occupation at earlier redshift which in terms of our more detailed semi-analytic treatment is equivalent to the accumulation over time of satellite galaxies in large host haloes due to an extended intrinsic merging time distribution, as opposite to the delta function we assumed for our simple derivation above. Combining such an extended distribution, e.g. a rectangle function  $\Pi(x)$

$$P(t_{\text{fric}}) = \frac{1}{T_0} \Pi(t_{\text{fric}}/T_0 - 1/2) \quad (5.8)$$

with a constant DM halo merger rate in a universe of finite age modelled by a step function  $\theta(x)$

$$\dot{N}_{\text{DM}}(t) = \frac{1}{t_0} \theta(t) \quad (5.9)$$

will yield a rather different result from what we derived previously in Eqn. 5.5. After inserting into Eqn. 5.3 we get

$$\dot{N}_{\text{Galaxies}}(t) = \frac{1}{t_0 T_0} \int_0^\infty \theta(t - t_{\text{fric}}) \Pi(t_{\text{fric}}) dt_{\text{fric}} \quad (5.10)$$

$$= \frac{t'}{t_0 T_0} \theta(t) \equiv \frac{t'}{T_0} \dot{N}_{\text{DM}} \quad (5.11)$$

where  $t' = \min(t, T_0)$  is defined as the minimum of the two arguments. The rise with  $t$  for  $t < T_0$  accounts naturally for the flattening of the galaxy merger rate with respect to the halo merger rate and for the eventual but late coincidence of the two.

[Berrier et al. \(2006\)](#) conclude that measuring galaxy merger rates is an important tool to understand the formation and evolution of galaxies. However it is not a good probe for cosmological structure formation, because the connection to the theoretically predicted halo merger rate is subject to too many uncertainties, for exactly the same reason. The discrepancies seen in Fig. 5.2 seem to support this view. On the other hand in the times of *concordance cosmology* determining cosmological parameters is not necessarily the top priority any more and to explore the details of galaxy formation is not a less worthwhile cause. Additionally it should be noted that the derivation of the galaxy merging timescale we will present later on is still valid but with the condition that it depends on mass and redshift, and keeping in mind that it is only an average value.

### 5.2.5. Dependence on mass and luminosity

Now we move on to study the evolution of galaxy merging rates with redshift subject to selection by various properties as shown in Fig. 5.3. In the upper row the major

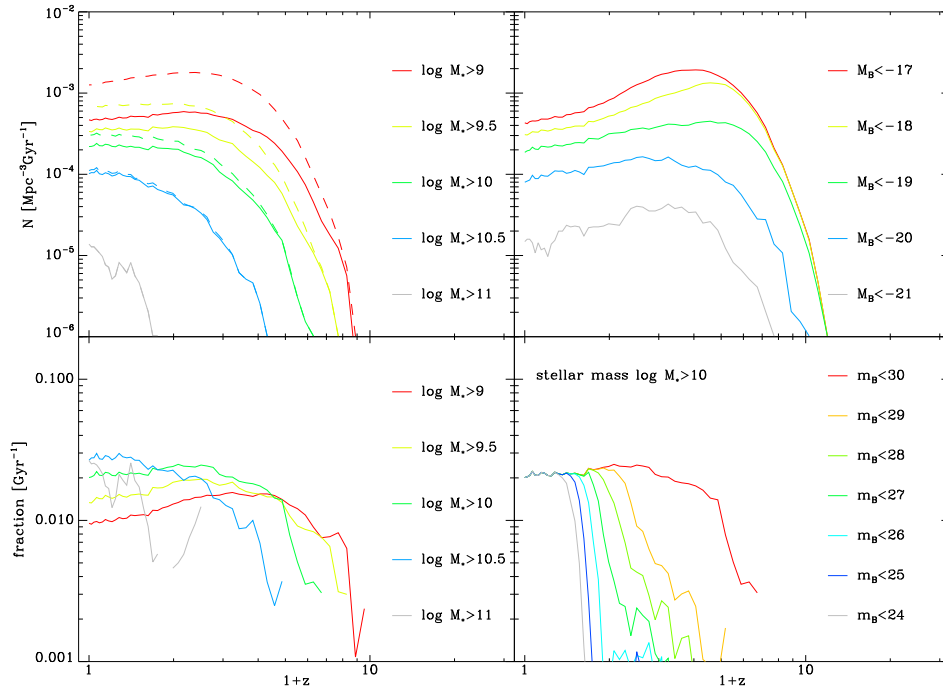


Figure 5.3.: The evolution of the major merger density and fraction in a box of size  $125 \text{ Mpc}/h$  on a side for galaxies satisfying different selection criteria in the following properties: stellar mass (left column), absolute rest-frame magnitude (top right panel), and apparent observer frame magnitude (bottom right panel). As indicated in the individual panels different colours denote different lower limits for mass and luminosity respectively. The dashed lines denote all mergers, including minor ones.

merger rate per comoving volume and unit time is shown whereas the bottom row shows major merger fractions normalised to the total abundance of galaxies with the given properties. These properties are stellar mass (left column; cf. Fig. 5.2), absolute rest-frame magnitude (top right panel), and apparent observer frame magnitude (bottom right panel). All cuts are lower limits, meaning the curves include galaxies which are more massive or brighter than the given threshold respectively, therefore the overall rate of mergers has to decrease with mass/luminosity in the top panels. The dashed lines in the top left panel denote the total of major and minor mergers for comparison reasons.

As already seen in Fig. 5.2 the merger rate peaks at an earlier redshift for smaller

## 5. Galaxy pairs

---

and/or fainter objects. Also the biggest objects make an appearance only very late, below a redshift of  $z = 1$ . These dependencies are most obvious when one cuts by stellar mass, using absolute rest-frame magnitude instead, the trends are slightly washed out. Especially the evolutionary brightening of the population with redshift leads to a cancellation and even overcompensation of the drop in merger rate with redshift that would otherwise be seen in massive galaxies. Cutting by apparent magnitude instead (plus a stellar mass cut to avoid resolution limit effects), the shape of the redshift evolution gets lost completely since the sample is not volume limited anymore and the sole difference between the differently deep samples becomes the cut-off redshift of the distribution.

The conclusion we draw from a look at these distributions is that cutting by stellar mass will yield the least biased result of the intrinsic galaxy merger rate, thus for the remainder of this paper we will ignore any other galaxy property. It should be noted that, since we need stellar masses for the definition of major versus minor mergers anyway, this choice does not produce any additional overhead. Secondly, for studies using surveys without stellar masses, using evolution corrected absolute magnitudes and defining major mergers based on magnitude difference may still yield valid results for redshifts  $z < 1$ . However this will introduce a strong additional dependence on the assumed luminosity evolution in the selected band, and also may be affected by starbursts due to tidal interactions, rendering the result considerably more uncertain.

### 5.2.6. The mock lightcone

The fundamental question we are addressing in this paper is how well the actual merger rate of galaxies of certain physical properties can be recovered from counting apparent pairs of galaxies on the sky. Naturally for such a study first of all we have to assign projected positions to our simulated galaxies. To this end we place a virtual observer at the origin of our simulation box and calculate which galaxies fall onto his backward lightcone<sup>2</sup>. For the near universe these will be the ones in the last snapshot of the simulation output at redshift  $z = 0$ , however as we go out along the line of sight we will have to populate the field of view with galaxies from progressively earlier snapshots. We also interpolate redshifts and most importantly luminosities in different filters between these snapshots in order to get a smooth evolution of these properties along the line of sight. A more detailed account of the exact methods used to produce mock observations from the Millennium Run semi-analytic galaxy catalogues can be found in [Kitzbichler & White \(2007\)](#).

---

<sup>2</sup>The backward light cone is defined as the set of all light-like worldlines intersecting the position of the observer at redshift zero. It is thus a three-dimensional hypersurface in four-dimensional space-time satisfying the condition that light emitted from every point is received by the observer now. Its space-like projection is the volume within the observer's current particle horizon.

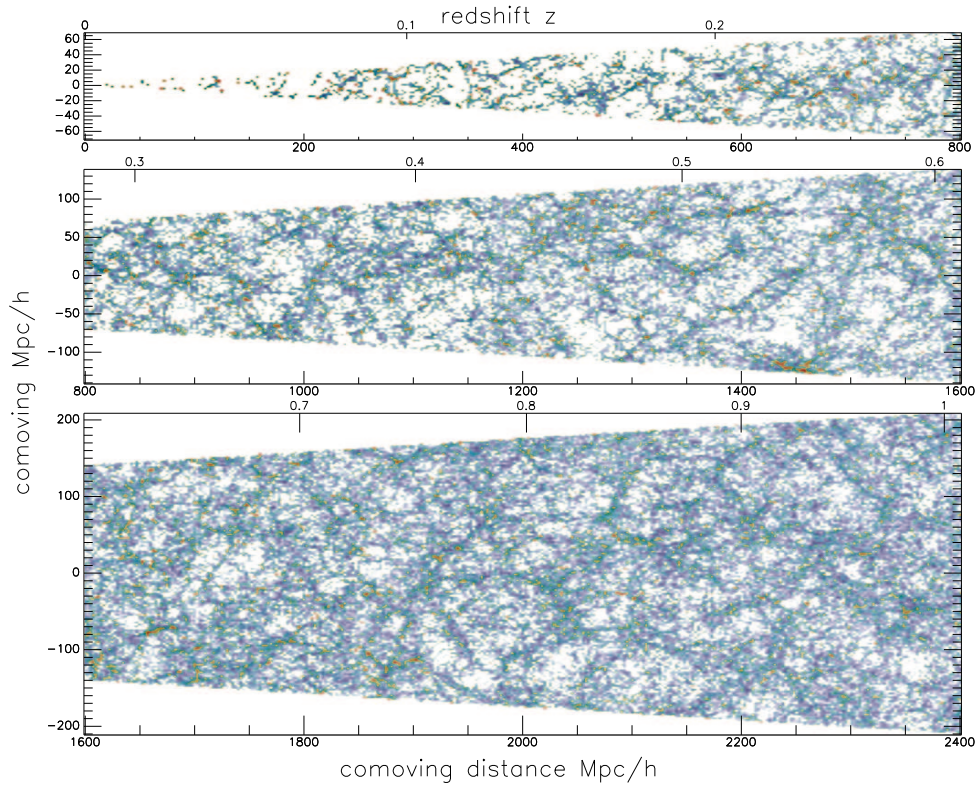


Figure 5.4.: The lightcone with a field of view of  $10 \times 1.4 \text{ deg}^2$  used for the subsequent pair and merger fraction studies. The colourmap encodes projected galaxy density as saturation and satellite galaxy fraction as colour (from blue to red). Only the region out to  $z = 1$  is displayed.

For the study presented in this paper we chose a field of view of  $10 \times 1.4 \text{ deg}^2$  which we found to be a good compromise between having a sufficiently large sample for robust statistics at all redshifts under consideration on the one hand and computational feasibility on the other hand. Additionally we assume a limiting apparent magnitude of  $B_{AB} \leq 26$  close to what can be considered as observationally possible for a survey of a larger area on the sky at the moment, and distinctly faintward of the current limit for reliable multi-object spectroscopy. This will make sure that our analysis is not compromised by missing faint objects out to redshift  $z \simeq 1$  (cf. bottom right panel in Fig. 5.3). However in practice this number depends on the assumed mass and absolute magnitude cut, as we will see in Section 5.4.5.

The final mock catalogue comprises 3236337 galaxies. In Fig. 5.4 we depict the

## 5. Galaxy pairs

---

spatial distribution of all galaxies out to  $z = 1$  in order to illustrate the extent of this mock lightcone. The large scale structure forming filaments and voids emerges vividly in this plot, where the projected galaxy density is encoded as saturation and the colour indicates the satellite galaxy fraction from blue to red. Clearly in the most clustered regions a majority of galaxies is in satellites whereas in the filaments and the sparsely populated voids galaxies are more independent and isolated.

### 5.3. Methods

#### 5.3.1. Finding pairs

A fundamental limitation of our mocks is that contrary to real observations, there are no signs of interaction between galaxies prior to merging, a criterion for pending mergers often used in close pair studies. Several authors have shown that especially in major mergers of massive galaxies the companions show clear signs of enhanced star formation and/or disturbed morphologies (e.g [Patton et al. 2005](#); [Lin et al. 2006](#), and references therein). This is a big advantage for observed galaxy pair counts that allows to dramatically increase the level of confidence of a putative pair detection. Our semi-analytic model of galaxy formation doesn't include any kind of environmental effects on galaxies, apart from the distinction between central galaxies and satellites.

Depending on the quality of the used galaxy sample such additional information is either decisive, in the case of the classical approach as described below, or a mere consistency check, if spectroscopy is available for the complete sample. In either case usually observational pair studies involve only of the order of a few dozen to a few hundred pairs, making it possible to look at every single pair manually to assess its probability to be real. However some surveys currently in progress or proposed for the near future will produce much larger samples that have to be analysed, which necessitates to automatize the pair classification. The reliability of such automatic morphological classification techniques depends crucially on a good signal-to-noise value and sufficient optical resolution. Provided both conditions are met, combining the classical CAS quantities (concentration, asymmetry, clumpiness) with *Gini* and  $M_{20}$  indices as for example described in detail by [Lotz et al. \(2004\)](#), will produce large samples of ten- to hundred thousand galaxy morphologies (see e.g. [Abraham et al. 2003](#); [Prescott et al. 2004](#); [Zamojski et al. 2006](#)) out of which about 1 – 3% can be assumed to show the signatures of an ongoing interaction. Our mock sample is yet an order of magnitude larger than these surveys but we lack the option to utilize distorted morphologies as evidence for a pending merger. Therefore it should be noted that even though we made the mock catalog to mimick true observations as closely as possible, there are certain aspects that will have to remain unaccounted for.

### 5.3.1.1. The classical approach

The most straightforward way to find pairs of galaxies is to simply identify galaxies which are close in angular projection in a purely photometric survey. This technique has been used for some of the earliest pair fraction studies (e.g. Zepf & Koo 1989) because it could be applied to the majority of surveys, yielding large enough galaxy catalogs ( $> 1000$  at that time); where one has to keep in mind that the pair fraction is in the range of a few percent, thus in order to get acceptable statistics for the pair sample the original catalog has to be much larger. The disadvantage of this purely photometric method is of course that one will inadvertently pick up a number of false pairs, i.e. chance projections that are not physically close. This “background noise” is naturally more problematic for higher mean background galaxy densities, corresponding to deeper magnitude limits - one reason why for the early studies at comparatively shallow limits this simple method worked reasonably well.

An estimate of the fraction of true companions can be derived from the angular correlation function  $w(\theta)$ . Only in the range where  $w(\theta) > 1$  is the probability greater than 50% that a companion found at an angular distance less than  $\theta$  is a true physical pair member. According to Limber’s equation (Limber 1953) the angular two-point correlation function depends on the limiting flux density  $f = L/4\pi r^2$  as  $w(\theta) \propto f^{\gamma/2}$  (assuming a power law  $\xi = (r_0/r)^\gamma$  for the spatial function). For such a deep survey as we simulate it here the angular separation  $\theta_0$  at which the condition  $w(\theta < \theta_0) > 1$  is satisfied is  $\theta_0 < 0.1''$  and thus unpractically small (independent of the fact that evolutionary effects render the Limber equation invalid in this case).

### 5.3.1.2. Primary redshift catalog with secondary companions

More recent pair studies (e.g. Yee & Ellingson 1995) usually have redshifts for at least one pair member which allows to search for companions within a radius in physical rather than angular coordinates and on the basis of an individual object. This yields a much better defined pair sample, even though the problem with purely optical pairs compromising the measurements remains. Additionally and most importantly this method makes it possible to quantify the evolution of pair galaxy fraction and properties over time.

### 5.3.1.3. Photometric redshift identification

If photometric redshifts are available for all galaxies in the catalog, this will allow an even better estimate of the pair fraction. As in the previous method one can define a physical search radius around each galaxy and additionally limit possible companion galaxies to the ones with redshifts within the measurement accuracy. However some correction for random pairs is still required. For a completely random distribution

## 5. Galaxy pairs

---

the number of galaxies within the cylindrical search volume around each galaxy within which we identify pairs is given by:

$$\mathcal{N}_{\text{Random}}(z) = \int n(z) dV \quad (5.12)$$

with the volume integration given by

$$\int dV = \int_{z-\Delta z}^{z+\Delta z} \frac{c dz}{H} \int_0^R 2\pi r dr \quad (5.13)$$

where  $R = (1+z)r_p$  is the search radius in comoving coordinates,

$$H(z) = H_0 \sqrt{\Omega_M(1+z)^3 + (1-\Omega_M)}$$

is the evolution of the Hubble expansion, and  $\Delta z$  is the assumed accuracy of our photometric redshifts. We also need the average galaxy density per unit volume  $n(z)$  which we can simply calculate from our catalogue.

Under the assumption that  $\Delta z$  is small, we can write:

$$\mathcal{N}_{\text{Random}}(z) = n(z) \frac{2c \Delta z}{H} \pi r_p^2 (1+z)^2 \quad (5.14)$$

Another issue that we have to account for is that we are restricting our survey to major mergers/pairs. Therefore we have to estimate the probability that a given random galaxy picked up in the search volume around our primary galaxy has also a similar mass. This number depends simply on the galaxy mass and is given by the integral over the stellar mass function  $\Psi$

$$P(M) = \frac{\int_{M_{\text{lim}}}^{\infty} \Psi(m) \Gamma(m/M) dm}{\int_{M_{\text{lim}}}^{\infty} \Psi(m) dm} \quad (5.15)$$

with the selection function  $\Gamma(x)$

$$\Gamma = \begin{cases} 1 & \text{if } |\log(x)| \leq \delta \\ 0 & \text{if } |\log(x)| > \delta \end{cases} \quad (5.16)$$

where  $\delta = \log(4)$  with our particular choice of major merger threshold. We can either choose to apply this probability on a per object basis or, in order to simplify things, we average over the whole mass range under consideration to get  $\langle P \rangle_{M > M_{\text{lim}}}$ .

The counts from Eqn. 5.14 times this probability give the number of major companions *per galaxy* that we will find in the search volume and thus it is identical to



the random pair *fraction*. Therefore we have to correct our raw pair counts  $N'_{\text{Pairs}}$  by subtracting the random pair fraction times number of galaxies:

$$N_{\text{Pairs}} = N'_{\text{Pairs}} - \langle P \rangle \mathcal{N}_{\text{Random}} N_{\text{Galaxies}} \quad (5.17)$$

Again, for the sample to be useful it should at least be satisfied that we are not dominated by the random galaxy counting noise, i.e.  $N_{\text{Pairs}}^2 \gg N'_{\text{Pairs}}$  in the redshift range under consideration.

### 5.3.1.4. Complete spectroscopic redshift identification

Clearly the ideal sample for a pair study is one that includes exact spectroscopic redshifts for all galaxies which allows to find kinematic companions in a combined physical separation – velocity space. This method yields an unbiased sample with minimal contamination by optical pairs since even though in principle the same correction for random pairs as derived in the previous section has to be applied, in practice this correction is so small that it can be neglected. Additionally one can discriminate between the physical pair population and its subset of true close pairs, i.e. such that are very likely to actually merge within a short timescale. How this is done will be explained in the next section.

### 5.3.2. Identifying mergers

Starting from a catalogue of the 20 closest projected companions on the sky for each galaxy we apply different criteria to define a subset of pairs that we assume to be pending mergers. These criteria are: (i) projected physical distance  $r_p$ , (ii) real three dimensional distance  $r_0$ , (iii) radial velocity difference  $\Delta v$ , (iv) redshift difference  $\Delta z$ , and they can be applied in different combinations. Additionally we distinguish between major and minor mergers based on the stellar mass ratio between the two pair members.

For the rest of the paper we will concentrate on major mergers which we define to have mass ratios of 4:1 or less. This restriction has been chosen for several reasons. First also observational studies usually concentrate on galaxy pairs that have members of similar brightness, either intrinsically because the absolute magnitude range under consideration is very small or by applying a limit in magnitude difference. This is to prevent confusion between actual companions and morphological features within the same galaxy. Also restricting to galaxy pairs in a narrow range of mass ratios defines a sample that suffers much less from selection effects and systematics than if we were to count every companion galaxy with the same weight, whether it is a dwarf or a giant. And finally from a theoretical point of view it is the growth from major mergers that is the relevant one for most galaxies, except for very massive cluster central galaxies which are not the main subject of our study. Also since

## 5. Galaxy pairs

---

we are only presenting counts and fractions here their relative contribution in terms of numbers is quite small due to their low spatial density.

Based on the set of parameters listed above we define a number of samples satisfying different criteria: for the projected physical distance  $r_p$  we chose values of 30, 50, and 100 kpc/ $h$ . Additionally we assume infinitely accurate redshifts for what we will subsequently call the “spectroscopic” sample and select pairs with radial velocity difference less than  $\Delta v < 300 \text{ km s}^{-1}$ . Finally we simulate also limited photometric redshift accuracy by selecting pairs with a rather generous redshift difference of  $\Delta z < 0.05$  comprising our “photometric” redshift sample. In the following section we will use the pair samples defined in such a way to compare the evolution of galaxy pair counts to the evolution of the merger rate of galaxies in the simulation.

### 5.4. Results

#### 5.4.1. Redshift distribution of pairs

Without looking at individual pairs we can already test our assumption that counting pairs can give the merger rate, by comparing the respective redshift distributions of pairs with that of mergers. Fig. 5.5 shows the redshift counts of pairs with different selection criteria, in particular different assumed redshift accuracy (black histograms). In the upper panel we show the “spectroscopic” sample selected for pairs with radial velocity difference less than  $\Delta v < 300 \text{ km s}^{-1}$  whereas the lower panel is for the “photometric” redshift sample with  $\Delta z < 0.05$ . Left and right columns denote different stellar mass cuts, left being for all galaxies and right for galaxies with  $M_* > 10^{10} M_\odot/h$ .

It is interesting to note that comparing to the merger rates in the full catalogue as seen in Fig. 5.3 one finds that for the total mass range the trend of pair counts with redshift seems to be the exact opposite. This is mostly a consequence of the apparent magnitude cut applied here which leads to a decreasing merger density with redshift if no explicit mass cut is applied because we go to higher effective masses at higher redshifts. For the higher mass cut we are essentially volume limited out to at least  $z = 0.5$  and thus we recover the intrinsic (flat) distribution.

The spectroscopic sample in combination with the mass cut yields almost exclusively real pairs, i.e. a correction for random pairs as derived in Eqn. 5.17 for the “photometric” redshift sample can be neglected since it is entirely insignificant. However, even though all spectroscopic pairs are real, a small fraction of them does not merge in finite time, therefore the pair counts in the top right panel are about 20% high compared to the merging pairs. This is due to companion galaxies that are close in projection and radial velocity, but not in terms of true spatial distance, because the chosen value of  $\Delta v < 300 \text{ km s}^{-1}$  will in effect allow distances along the line of sight of up to 3 Mpc/ $h$ . On this scale the 2-point correlation function is still

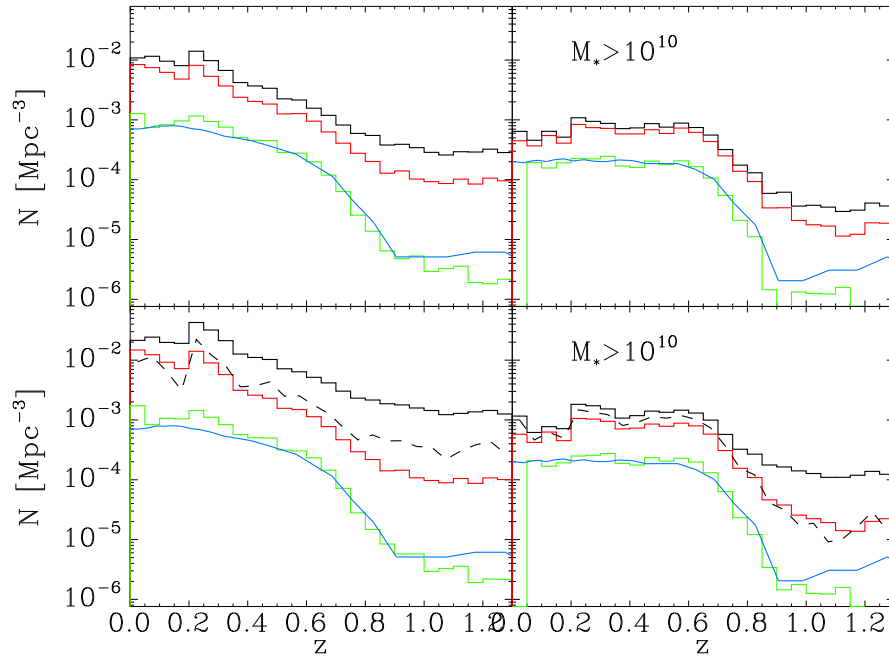


Figure 5.5.: Evolution of the number of identified galaxy pairs per unit volume with projected distance  $r_p < 50 \text{ kpc}/h$ . The additional identification criteria are radial velocity difference  $\Delta v < 300 \text{ km s}^{-1}$  in the upper panels (“spectroscopic” sample) and redshift difference  $\Delta z < 0.05$  in the lower panels (“photometric” redshifts). Colours encode full sample (black), sample corrected for random pairs (dashed), real pairs confirmed to merge (red), and such merging within  $1000 \text{ Myr}/h$  (green) respectively. Additionally the blue solid line indicates the merger density taken from the full simulation directly, where the merging time limit is again  $1000 \text{ Myr}/h$ , and an apparent magnitude limit similar to the one in the mock catalogue was applied. The panels in the left column show all major mergers whereas the right column shows only pairs with both galaxies more massive than  $10^{10} M_{\odot}/h$ .

non negligible and thus the random pair correction does not account sufficiently for these pairs. Choosing a more restrictive value for  $\Delta v$  would help but at the expense of missing an increasing number of pairs that would merge. The trade-off between these two considerations will be briefly addressed in the following section.

## 5. Galaxy pairs

---

For the moment however we discuss Fig. 5.5 a bit more, now concentrating on the bottom panels where the “photometric” redshift sample is shown. In the absence of accurate spectroscopic redshifts and failing to correct for random pairs the merger rate results in an overestimation by as much as one order of magnitude as the bottom left panel shows. It compares the black curve of total pair counts to the red curve showing the fraction of identified pairs which are confirmed to merge with their companion eventually. Clearly for the more massive pairs accurate redshifts are less important, as shown in the right column of Fig. 5.5. In the high mass regime the overprediction due to redshift uncertainties is only a third of the sample comprising all masses and the overall shape of the distribution is recovered correctly out to  $z \sim 0.7$  where false detections become dominant. However beyond this redshift the sample is not anymore volume limited and the merger counts drop by two orders of magnitude due to the apparent magnitude cut, making this range unsuitable for a study of the merger rate anyway. The fraction of wrong identifications becomes worse with redshift for both the total and mass limited samples, however, again the latter suffers much less from the problem.

Even though we don’t know for an individual pair whether it is real, i.e. will merge eventually, we can correct for the wrong identifications statistically by subtracting the expected number of random pairs according to Eqn. 5.17. This yields the dashed curves in the bottom panels of Fig. 5.5 which are in much better agreement with the distribution of real pairs given by the red histogram. Thus we have established that a corrected sample of pairs from surveys using photometric redshifts will give the right number of real pairs. This means that the average timescale for conversion from pair counts to merger rates that we will present in the following section can be derived for pairs with “photometric” redshifts in the exact same way as in the case of spectroscopic pairs in order to calculate the overall merger rate. However in the remaining part of this paper where we look at the merging timescale of pairs in detail we will consider only spectroscopic pairs since only for those can we identify real pairs on the basis of individual objects.

### 5.4.2. The average merging time of galaxy pairs

The most important issue we want to address here is the timescale on which galaxy pairs merge. If we follow the usual practice and assume this to be at the most  $t_{\text{fric}} \leq 1000 \text{ Myr}/h$  and count all galaxies from the full catalogue that will have a merger within this period as a function of redshift we get the blue solid line in Fig. 5.5. It is readily apparent that this timescale must be much too short since we underpredict the number of pairs by an order of magnitude. The discrepancy is worst at low redshifts and without mass cut since the average timescale is much larger than  $1000 \text{ Myr}/h$  for the low mass objects dominating the sample nearby. We can confirm immediately that it is really the timescale that is responsible by requiring a merging time below

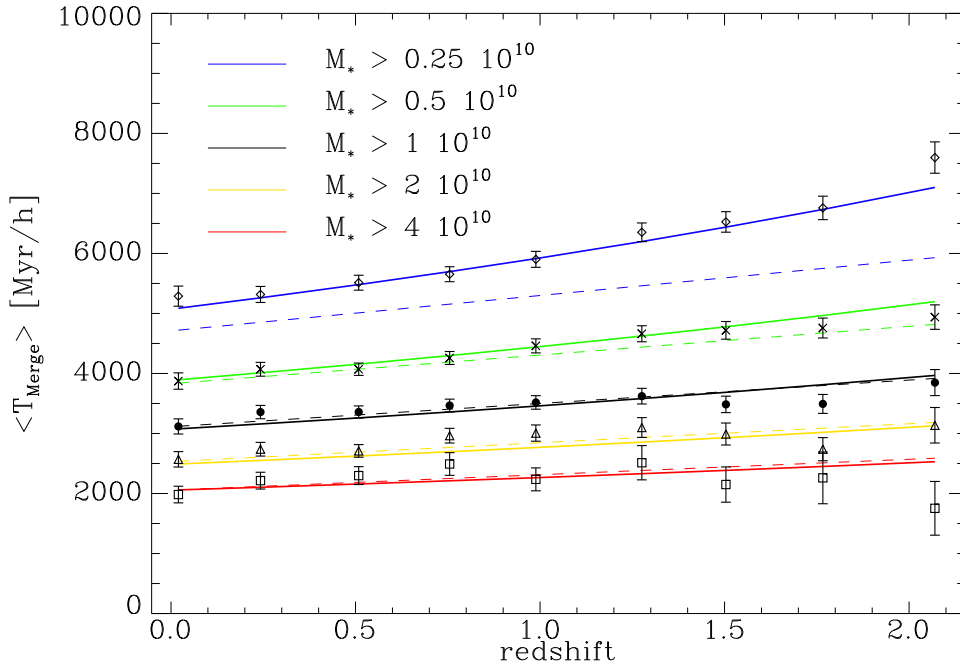


Figure 5.6.: Redshift evolution of the timescale  $T = N_{\text{Pairs}}/\dot{N}_{\text{Merge}}$  for conversion from pair fraction to merger rate. Two-dimensional linear regression fits are plotted for a range of mass cuts denoted by different colours. The fiducial  $M_* > 10^{10} M_{\odot}/h$  is indicated by the black curve for which the data together with error bars is also shown, as well as for the lowest mass cut (blue curve). The pair identification criteria were projected distance  $r_p < 50 \text{ kpc}/h$  and radial velocity difference  $\Delta v < 300 \text{ km s}^{-1}$ . The dashed lines are for a simplified fit.

1000 Myr/h for the sample of real pairs as well which yields the green line in Fig. 5.5 lying exactly on top of the intrinsic merger rate. Unfortunately in practice such a selection cannot be made and one has to assume a reasonable average timescale of merging instead.

We demonstrated in Eqn. 5.7 that such a typical timescale is simply given by the relative ratio between pair and merger distribution,

$$\langle T_{\text{Merge}} \rangle = N_{\text{Pairs}}/\dot{N}_{\text{Merge}} \quad (5.18)$$

Calculating this ratio as a function of redshift and mass cut yields the results pre-

## 5. Galaxy pairs

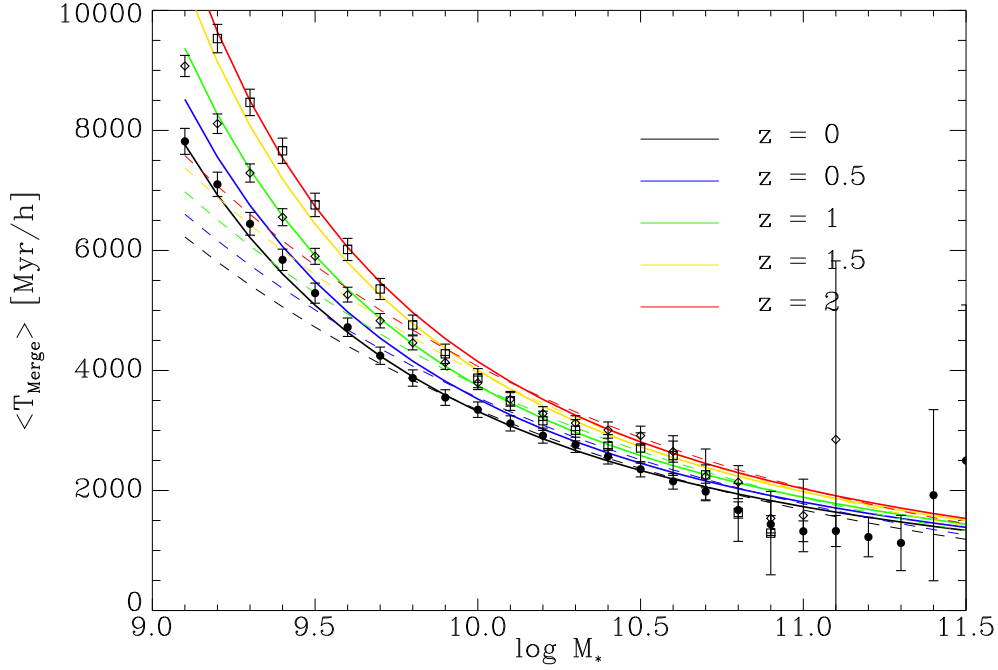


Figure 5.7.: Analogous to Fig. 5.6, dependence of  $T = N_{\text{Pairs}}/\dot{N}_{\text{Merge}}$  on stellar mass cut. Different colours denote different redshifts, where black is for  $z = 0$  and green is for  $z = 1$  for which the data together with error bars are shown as well. Only fits are plotted for the other redshift ranges. It should be noted that, because this is a cumulative plot, the data points and error bars are not independent of each other. The dashed lines are for a simplified fit.

sented in Figs 5.6 and 5.7. Since the square root of the inverse of this dependency seems to be linear within the scatter for mass cuts below  $10^{10} M_{\odot}/h$  we decided to apply a two-dimensional linear regression fit to  $\langle T_{\text{Merge}} \rangle^{-1/2} \equiv T^{-1/2}(z, M_*)$  assuming the relation

$$\langle T_{\text{Merge}} \rangle^{-1/2} = T_0^{-1/2} + f_1 z + f_2 (\log M_* - 10). \quad (5.19)$$

The value  $T_0$  as well as the coefficients  $f_x$  and their uncertainties calculated from the fit have been tabulated for different identification criteria in Table 5.1.

In the low redshift regime and for stellar masses above  $10^{10} M_{\odot}/h$  an even simpler

fitting formula can be approximated with

$$\langle T_{\text{Merge}} \rangle = 2200 \text{ Myr}/h \frac{r_p}{50 \text{ kpc}/h} \left( \frac{M_*}{4 \cdot 10^{10} \text{ M}_\odot/h} \right)^{-0.3} \left( 1 + \frac{z}{8} \right), \quad (5.20)$$

for spectroscopic redshifts and

$$\langle T_{\text{Merge}} \rangle = 3200 \text{ Myr}/h \frac{r_p}{50 \text{ kpc}/h} \left( \frac{M_*}{4 \cdot 10^{10} \text{ M}_\odot/h} \right)^{-0.3} \left( 1 + \frac{z}{20} \right), \quad (5.21)$$

for photometric redshifts. These simplified fits give the results indicated by the dashed lines in Figs 5.6 and 5.7.

Aside from the dependence on mass cut and redshift that are illustrated in these figures, the timescales change strongly with the pair identification criteria, in particular with the projected radius  $r_p$ . This is a natural consequence of Eqn. 5.18 since the denominator  $N_{\text{Merge}}$  is independent of  $r_p$  whereas the numerator  $N_{\text{Pairs}}$  is not. Instead it is equivalent to the integral of the projected 2-point correlation function  $w_p(r)$  out to  $r_p$  (see Eqn. 5.2). If we choose the usual parametrisation  $w_p \sim (r/r_0)^{-\alpha}$  we get  $N_{\text{Pairs}} \sim r_p^{2-\alpha}$ , where a value of  $\alpha = 0.8$  is commonly assumed in the literature. Thus we would expect the values in the table to scale as  $r_p^{1.2}$  which is qualitatively consistent with the actual values but slightly too strong. If we conversely calculate  $\alpha$  from the measured values we get  $\alpha = 1.06$  and  $\alpha = 0.93$  for the intervals 30-50 kpc/h and 50-100 kpc/h respectively. This result reflects the same finding in Fig. 5.1 where we have seen that the projected 2-point correlation function on scales below 100 kpc/h and for masses above  $3 \cdot 10^{10} \text{ M}_\odot/h$  can be considerably steeper than the fiducial  $\alpha = 0.8$ .

Thus we have shown that the average timescale we have derived from studying individual close pairs in our simulation is consistent with the general large-scale structure statistics presented earlier in the paper. Before we apply this timescale to the galaxy pair counts extracted from our mock lightcone in Section 5.4.5 we will briefly digress and study the remaining question how well this average timescale reflects the actual merging times of individual galaxy pairs. This is necessary since, due to the way it was defined, this average value also includes a number of additional effects such as the contamination with false pairs, missed pairs, and the shape and time evolution of the true merging time distribution. These issues will be addressed in the following.

### 5.4.3. Completeness and contamination

Even though for the purpose of studying the merger rate evolution in the universe it may be sufficient to find the correct timescale to convert pair counts into merger rate, it is still a relevant question how many of the individual pairs we find are real and on

## 5. Galaxy pairs

Table 5.1.: Coefficients for different pair identification criteria obtained from the linear regression fit of  $\langle T_{\text{Merge}} \rangle = T(z, M_*)$  to the data  $N_{\text{Pairs}}/\dot{N}_{\text{Merge}}(z, M_*)$  according to Eqn. 5.19.

VELOCITY	PROJECTED DISTANCE		
	$r_p$		
$v_p < 300 \text{ km s}^{-1}$	$\leq 30 \text{ kpc}/h$	$\leq 50 \text{ kpc}/h$	$\leq 100 \text{ kpc}/h$
$T_0 [\text{Myr}/h] \dots\dots$	2038	3310	6909
$10^5 f_1 [\text{Myr}/h^{-1/2}]$	$-165. \pm 4.4$	$-105. \pm 3.3$	$-30.4 \pm 2.2$
$10^5 f_2 [\text{Myr}/h^{-1/2}]$	$690. \pm 10.$	$668. \pm 7.7$	$571. \pm 5.2$
$v_p < 3000 \text{ km s}^{-1}$	$\leq 30 \text{ kpc}/h$	$\leq 50 \text{ kpc}/h$	$\leq 100 \text{ kpc}/h$
$T_0 [\text{Myr}/h] \dots\dots$	2806	4971	11412
$10^5 f_1 [\text{Myr}/h^{-1/2}]$	$-94.7 \pm 3.7$	$-38.6 \pm 2.7$	$18.0 \pm 1.7$
$10^5 f_2 [\text{Myr}/h^{-1/2}]$	$671. \pm 8.7$	$615. \pm 6.3$	$491. \pm 4.2$

the other hand how many we miss. In Fig. 5.8 the latter issue is addressed. It shows, for galaxies from the full catalog that are going to merge within the next simulation timestep, the distribution in the  $\Delta v$  versus  $r_p$  plane, where in the absence of a line of sight the projection was arbitrarily chosen along the z-axis. The pair identification criteria of projected distance  $r_p < 50 \text{ kpc}/h$  and radial velocity difference  $\Delta v < 300 \text{ km s}^{-1}$  chosen for an assumed spectroscopic mock sample are indicated by the grey lines. When one considers mergers in all mass ranges, one will miss more than half of the merging pairs with these criteria, but very few of the massive ones with  $M_* > 10^{10} M_\odot/h$  as the overlaid contours in the plot show.

Conversely, the fraction of identified pairs that are real pairs is presented in Fig. 5.9, where a real pair was defined to be one that will merge into the same object eventually. The most obvious correlation is with projected distance, pairs closer than  $r_p < 10 \text{ kpc}/h$  have a very high probability to be real whereas for larger separations this probability drops to less than 50%. However, if pairs with masses  $M_* > 10^{10} M_\odot/h$  are considered, only the ones with both pair selection criteria close to their limiting thresholds have low real fractions. It should be noted that most of the pairs are concentrated in this region of the  $\Delta v$  versus  $r_p$  plane due to geometrical and stochastic reasons, thus giving increased significance to this apparently small contamination.



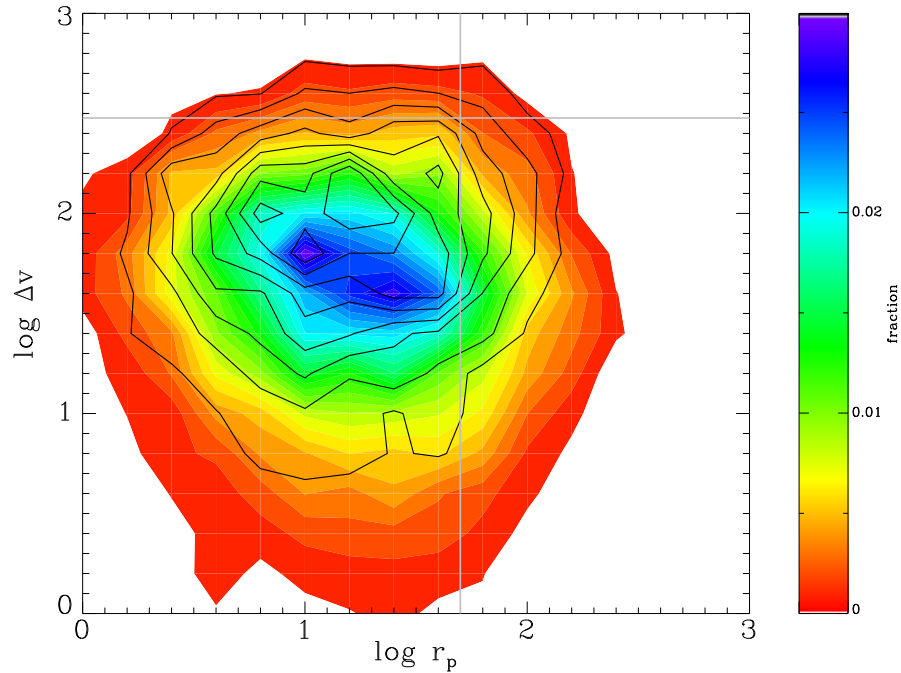


Figure 5.8.: The distribution in the  $\Delta v$  versus  $r_p$  plane of galaxies from the full catalog that are going to merge within one timestep, where the projection was arbitrarily chosen along the  $z$ -axis. The filled contours in color denote (major) pair galaxies of all masses (colors mean fraction of total with linear mapping) whereas the overlaid contours are with a mass cut of  $M_* > 10^{10} M_\odot/h$ . Grey lines indicate the selection criteria projected distance  $r_p < 50 \text{ kpc}/h$  and radial velocity difference  $\Delta v < 300 \text{ km s}^{-1}$ .

#### 5.4.4. Distribution of merging times

Fig. 5.10 shows the distribution of merging times in the lightcone and in the full catalog at four different redshifts for galaxies with  $M_* > 10^{10} M_\odot/h$ . The pair selection criteria were  $r_p < 50 \text{ kpc}/h$  and  $\Delta v < 300 \text{ km s}^{-1}$ . Most importantly it is readily apparent that the usual assumption that pairs found with such criteria are going to merge within a short timescale well below  $1000 \text{ Myr}/h$  cannot be confirmed. Even though in the lowest redshift panel it appears that the maximum lies at only  $2000 \text{ Myr}/h$ , this limit is not real but forced by the finite timespan between  $z = 0.25$  and  $z = 0$  as merging times were derived by following galaxy histories up to the present, but not

## 5. Galaxy pairs

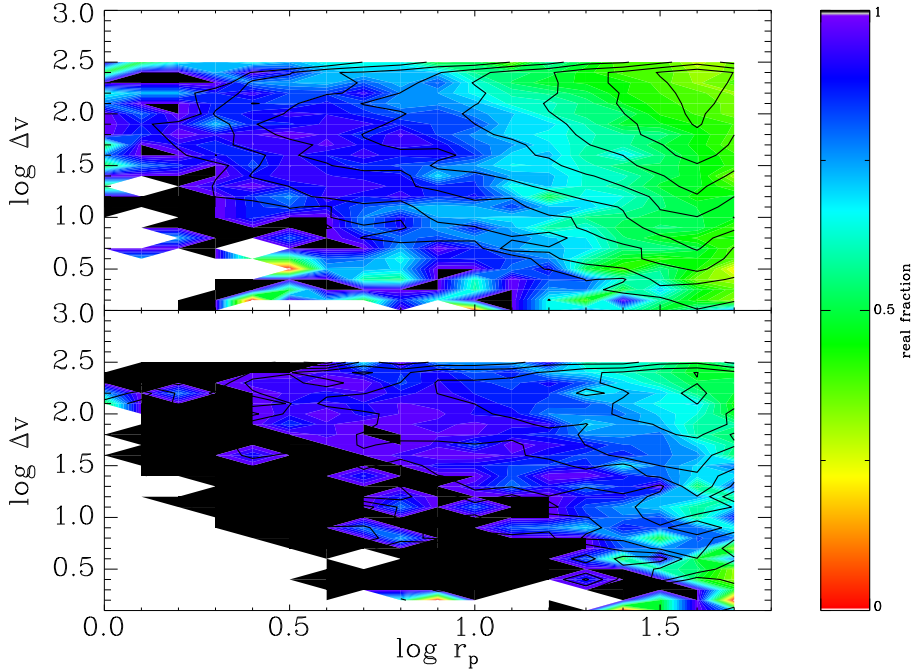


Figure 5.9.: The distribution in the  $\Delta v$  versus  $r_p$  plane of galaxy pairs in the lightcone. The filled contours in color denote the fraction of real mergers from 0 to 1. Overlaid contours show the logarithmic distribution of identified pairs with projected distance  $r_p < 50 \text{ kpc}/h$  and radial velocity difference  $\Delta v < 300 \text{ km s}^{-1}$ . The top panel is for the complete mass range whereas the bottom panel shows only pairs with  $M_* > 10^{10} M_\odot/h$ .

into the future. If instead merging times defined by the internal counters of merging galaxies are plotted, a rather extended tail appears since those do not suffer from this limitation. Secondly one can see how the considerable incompleteness of the sample with this mass cut at redshifts beyond  $z \sim 0.75$  affects the distribution. The magnitude cut in the  $B$ -band causes preferentially the reddest faint galaxies to be missed which tend to be galaxies that have been satellites for a long time and thus little time left until the merger. Finally the distributions from the lightcone and the full catalog have similar shapes and also agree quantitatively, which mirrors the same good agreement found in Fig. 5.5 and is evidence for a fair sampling of the merger population. This is an important result because it confirms that it is possible to infer the actual merger rate from counting pairs even in the absence of any information

about the real merging time of an individual observed pair.

Fig. 5.11 emphasises this point by showing the cumulative distribution of the data in Fig. 5.10 for the pairs extracted from the lightcones, now normalised to unity and with all redshift ranges plotted on top of each other. It is interesting to note that a primitive model of a uniform initial merging time distribution with a limit of 4000 Myr/h (see Eqn. 5.8 and also Eqn. 5.9) indicated here by the dotted black lines represents already quite good a fit to the data. One has to assume a fraction of galaxies between 20% and 35% to have infinite merging times however. The data curves all coincide within the errors apart from the red one which is for the highest redshifts where the effects from incompleteness dominate (cf. bottom right panel in Fig. 5.10). Hence for a volume limited sample with  $M_* > 10^{10} M_\odot/h$  and in the redshift range  $z = 0 - 0.75$  one can derive the fraction of pairs which are going to merge within a certain timescale. In our case we can state that 30% of pairs are going to merge within  $T_{\text{Merge}} = 1000 \text{ Myr}/h$ .

### 5.4.5. Pair versus merger fraction evolution

The average timescales derived in Section 5.4.2 and presented in Table 5.1 provide a calibration that allows to convert measured pair counts to merger rates. In Fig. 5.12 we demonstrate that this conversion gives correct results by comparing the intrinsic merger rate in the full simulation to the calibrated merger rate derived from the pair counts in our mock lightcone for three different stellar mass cuts. In all cases the original merger rate evolution can be recovered within the uncertainties of the intrinsic scatter of the observation. With a pair selection criterion of  $r_p < 50 \text{ kpc}/h$  and  $v_p < 300 \text{ km s}^{-1}$  the agreement with the fiducial merger rate derived from the full catalog is excellent out to  $z = 0.6$  where the sample loses its volume limited property. It should be noted that the merger fraction shows a considerably smaller scatter than the merger density because cosmic variance cancels to first order. On the other hand information is lost about the change with stellar mass of the merger frequency and the slope of the evolution.

It should be noted that the “photometric” sample can be used in the same way as the “spectroscopic” one since it gives identical pair counts after the correction for random pairs has been applied, as was shown in Fig. 5.5. Naturally a larger scatter is found in this case however, because of the cumulative uncertainties from counts and corrections.

## 5.5. Conclusions

We have investigated the rate of galaxy mergers in our semi-analytic model based on the Millennium N-body simulation and compared it to the number of galaxy pairs.

## 5. Galaxy pairs

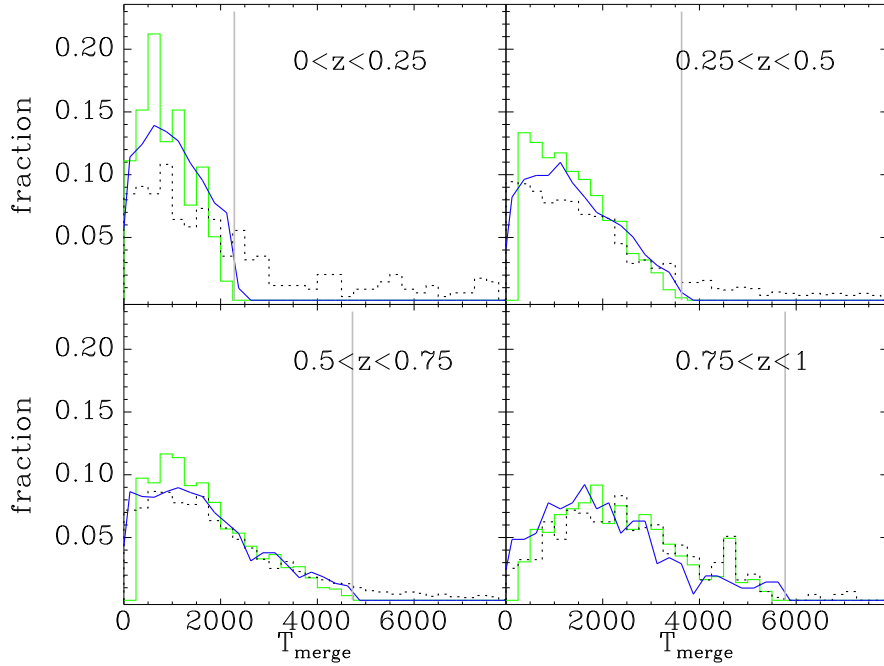


Figure 5.10.: Distribution of merging times of galaxies more massive than  $M_* > 10^{10} M_\odot/h$  at four different redshifts. Green is for pairs from the light-cone with  $r_p < 50 \text{ kpc}/h$  and  $\Delta v < 300 \text{ km s}^{-1}$ . Blue is for the full catalogue. Merging times were determined by following the galaxy histories until the present. The timespan between the highest redshift in a panel and  $z = 0$  is indicated by the grey vertical line. Merging times of cone galaxies determined by their internal counter are indicated by the dashed black line. All samples have been subject to an apparent magnitude cut of  $B < 26$  and only major mergers were considered.

From this we have derived an average timescale for major galaxy mergers that calibrates the conversion from observed galaxy pairs of similar stellar mass to major merger rate. Furthermore it was established that this timescale is consistent with the real merging times of individual galaxy pairs. Finally we have shown that the fiducial galaxy merger rate can be recovered from the pair counts in the mock catalog. The ideal survey to be used for this purpose is volume limited, selected by stellar mass, and provides spectroscopic redshifts of all galaxies, even though neither of these properties is essential. Photometric redshifts can be used provided an accurate

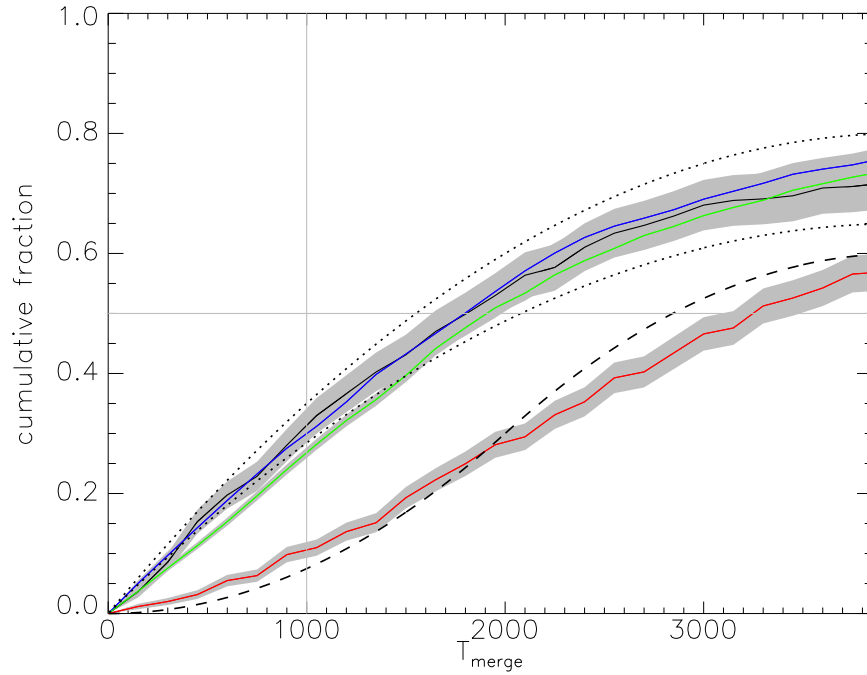


Figure 5.11.: Similar to Fig. 5.10 but cumulative and normalised to unity. Also only data from the lightcone is shown and all four redshift ranges are overplotted, where colours denote redshifts from black, blue, green to red, corresponding to the redshift ranges in Fig. 5.10. The gray lines indicate a merging time  $T_{\text{Merge}} = 1000 \text{ Myr}/h$  and the 50% percentile respectively in order to guide the eye. Solid lines are for the sample with mass cut  $M_* > 10^{10} M_{\odot}/h$ . The dotted and dashed black lines are predictions derived from a simple model.

correction for random pairs is applied. However, the result will have intrinsically larger error bars. Also the study of individual properties of merging galaxies will be less reliable.

The main results of our study are as follows:

1. A calibrating average merger timescale can be found that reliably converts corrected pair counts into merger rates (Fig. 5.12). It depends on the pair identification criteria, stellar mass cut and weakly on redshift and can be approximated

## 5. Galaxy pairs

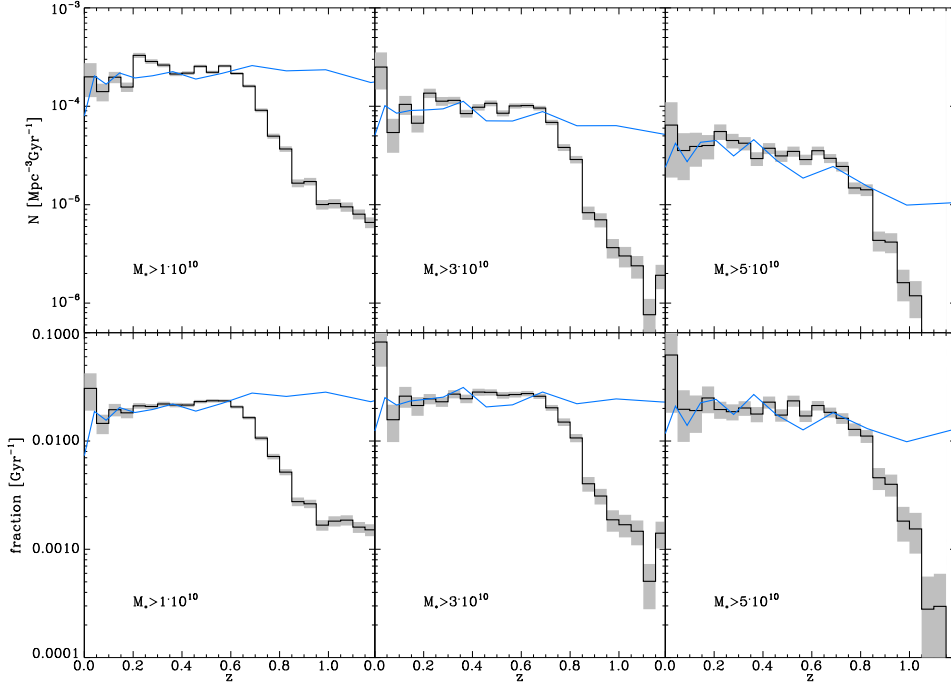


Figure 5.12.: Comparison of lightcone merger rates derived from calibrated pair counts (black histograms) to intrinsic merger rate evolution in the full catalog (blue lines). The upper panels show the comoving density of major mergers whereas the lower panels are major merger fraction as a function of redshift. The columns correspond to three different stellar mass cuts of 1, 3, and 5 times  $10^{10} M_{\odot}/h$ . In the case of the pairs the identification criteria were  $r_p < 50 \text{ kpc}/h$ , and  $v_p < 300 \text{ km s}^{-1}$ . For the conversion from pair counts to merger rates the corresponding average timescales from Table 5.1 were used.

by the simple relation

$$\langle T_{\text{Merge}} \rangle = 2200 \text{ Myr}/h \frac{r_p}{50 \text{ kpc}/h} \left( \frac{M_*}{4 \cdot 10^{10} M_{\odot}/h} \right)^{-0.3} \left( 1 + \frac{z}{8} \right),$$

for radial velocity difference  $v_p < 300 \text{ km s}^{-1}$  and by

$$\langle T_{\text{Merge}} \rangle = 3200 \text{ Myr}/h \frac{r_p}{50 \text{ kpc}/h} \left( \frac{M_*}{4 \cdot 10^{10} M_{\odot}/h} \right)^{-0.3} \left( 1 + \frac{z}{20} \right),$$

for  $v_p < 3000 \text{ km s}^{-1}$  respectively. A more accurate fitting formula is given in Eqn. 5.19 for which the corresponding coefficients  $T_0$ ,  $f_1$  and  $f_2$  are listed in Table 5.1 for a range of pair selection criteria.

2. Since  $T_0$  is at least  $2000 \text{ Myr}/h$ , depending on projected pair distance, the average merger timescale is considerably larger for all masses and redshifts than the  $500 \text{ Myr}/h$  typically assumed in the majority of pair studies.
3. In the mass range  $M_* > 10^{10} M_\odot/h$ , the intrinsic galaxy merger rate evolution, as also recovered from the mocks, goes like  $\dot{N} \sim (1+z)^{1/2}$ . For larger masses the exponent can even turn negative and overall the distribution is quite flat out to redshift  $z = 1$  (see e.g. Fig. 5.12). Observational results lie in the range  $N_{\text{Pair}} \sim (1+z)^{2\pm 2}$  where the large uncertainties are presumably due to small sample sizes and selection effects not sufficiently well taken into account. It was demonstrated that cutting by magnitude instead of mass will lead to a steepening of the relation (top right panel in Fig. 5.3). The samples we have defined are volume limited and we select major merger pairs by stellar mass, thus our sample should be affected as little as possible by this issue.
4. Due to the extended intrinsic merging time distribution peaking well beyond  $1000 \text{ Myr}/h$ , the flat galaxy merger rate evolution we find is different from the DM halo merger rate which has an intrinsic slope of  $\dot{N} \sim (1+z)^{3/2}$  for all masses (Fig. 5.2). Such a discrepancy has already been described by other authors, and we follow their conclusion that merger rate studies are less suitable as a probe of cosmic structure formation, as they were originally intended. Instead they can be of great help to understand the formation and evolution of galaxies in a hierarchical universe.

**Acknowledgements:** MGK acknowledges a PhD fellowship from the International Max Planck Research School in Astrophysics, and support from a Marie Curie Host Fellowship for Early Stage Research Training.

## 5. Galaxy pairs

---



# 6

## Conclusions

### 6.1. Discussion of results

In Chapter 3 we studied the question whether the available observational data are consistent with the idea that present-day luminous galaxies assembled the bulk of their stars at high redshift. If so, it should be possible to find a set of parameters such that traditional “Pure Luminosity Evolution” (PLE) models can simultaneously reproduce: (i) the present-day luminosity and colour distributions of massive galaxies; (ii) the passive evolution in colour and M/L ratio observed for massive early-type galaxies in clusters; and (iii) the observed galaxy counts as a function of redshift in deep surveys.

We used the local LF split up by colour from the SDSS survey to construct a variety of possible PLE models differing in their IMF, metallicity, formation redshift  $z_f$ , and star formation history (SFH). Out to redshift  $z \sim 1$  our model predictions are very similar to each other and also fit the data reasonably well, given their error bars. At higher redshifts all models predict too many galaxies. Only one model with a slope of the initial mass function (IMF) of  $x = 2$ , comes close to the data. The more conventional standard model using a Salpeter IMF produces the predictions most inconsistent with the data. However models with  $x = 2$  are inconsistent with observation. Most models for the light output and metal production of high-redshift galaxies require IMF’s with substantially *more* high mass stars than Salpeter (e.g. [Nagashima et al. 2004](#)), an IMF as steep as  $x = 2$  appears very unlikely as an explanation of the apparent lack of high-redshift massive galaxies. This is an important result since many observational publications still compare their data to PLE models

## 6. Conclusions

---

with rather steep Scalo IMF's, finding reasonably good agreement (e.g. [Cimatti et al. 2002c](#), and references therein). All of our realistic models overpredict the counts at redshifts  $z > 1$  by a large factor, in the interval  $2 < z < 3$  they are off by factors between 4 and 11. It is unlikely that cosmic variance could account for this. Extinction by dust, on the other hand, might indeed be important. However our results show that the simple dust treatment conventionally applied to PLE models is not sufficient. A more extreme assumption about the amount of extinction at high redshift like that of [Totani et al. \(2001\)](#) would be needed. However, we have demonstrated that the  $M/L$  values assumed in our standard PLE model with no or moderate obscuration are very similar to those measured in real high-redshift galaxies. Thus PLE models with moderate obscuration match the observed mass-to-light ratios at high redshift but overpredict abundances, while models with sufficient obscuration to fit the observed abundances substantially overpredict high-redshift mass-to-light ratios.

Our main conclusion in this chapter is thus that “traditional” PLE models, as originally introduced by [Tinsley \(1980\)](#), cannot reconcile the relatively small number of high-redshift galaxies found in deep  $K$ -selected redshift surveys with the abundance of massive galaxies seen in the local Universe.

In Chapter 4 we took a much more ambitious approach compared to the simplified PLE models in order to study the high-redshift galaxy population. Based on the largest N-body simulation of dark-matter carried out to date, we used a semi-analytic model of galaxy formation to follow the physics of baryons as they cool into the potential wells of DM haloes and form stars. The model we have used was that of [Springel et al. \(2005\)](#) and [Croton et al. \(2006\)](#) as updated by [De Lucia & Blaizot \(2007\)](#) and involves several types of feedback processes which regulate star formation as described in detail in Chapter 2. Earlier work had compared this model to a wide range of properties of low redshift galaxies: their luminosity functions, their bi-modal luminosity-colour-morphology distribution and their Tully-Fisher relation ([Croton et al. 2006](#)), which were the most important data to calibrate the model. Here we compared its predictions in detail with observations of high redshift galaxies for the first time. We decided to produce mock observations of our model galaxies, which would allow us to make use of high-redshift data directly, without having to rely on less robust derived quantities like rest-frame luminosities or stellar mass. To this end we constructed a set of deep light-cone surveys from the simulation as outlined in the second part of Chapter 2 and described in detail in the modelling section of Chapter 4.

Comparing the model predictions from these mock catalogues to the observed counts, to redshift distributions and to observational estimates of luminosity and mass functions at high redshift painted a consistent picture. Whereas the low-redshift properties of simulated galaxies match the observations they have been calibrated on, the evolution of abundance, luminosities, and colours in the model deviates from the

observed one, especially in the  $K$ -band where the predicted evolution is considerably weaker than the data. Hence our model appears to have too many relatively massive galaxies at high redshift and these galaxies appear to be too red. This overabundance of apparently red galaxies shows up in the redshift distributions as an overprediction of the number of galaxies with apparent magnitudes  $m_K(AB) > 22$  at redshifts between about 1 and 3. These correspond to moderately massive systems near the knee of the luminosity function, where also in the rest-frame  $K$  our luminosity functions are noticeably high beyond  $z = 0.5$  except possibly for the brightest objects. The problem shows up most clearly in our mass functions which overpredict observationally estimated abundances by about a factor of 2 at  $z = 2$ . Apparently the mass function of galaxies evolved more strongly in the real Universe than in our simulation.

The fact that the model we test here apparently *overpredicts* the abundance of moderately massive galaxies at high redshift, despite the fact that late merging plays a major role in the build-up of its more massive galaxies (e.g. De Lucia et al. 2006; De Lucia & Blaizot 2007), demonstrates that current data are still far from constraining the importance of this process. As the data improve, the models will have to improve also to remain consistent with them. This interplay between theory and observation should eventually lead to an improved and more complete picture of how galaxies came to take their present forms.

Finally in Chapter 5 we made use of the capability of the sophisticated semi-analytic model in combination with the light-cone construction to produce mock observations of unprecedented statistical power to study the connection between number counts of observed galaxy pairs and evolution of galaxy merger rate in the universe. To this end we have investigated the rate of galaxy mergers in our semi-analytic model based on the Millennium N-body simulation and compared it to the number of galaxy pairs. From this we have derived an average timescale for major galaxy mergers that calibrates the conversion from observed galaxy pairs of similar stellar mass to major merger rate. Furthermore it was established that this timescale is consistent with the real merging times of individual galaxy pairs. Finally we have shown that the fiducial galaxy merger rate can be recovered from the pair counts in the mock light-cone.

The main results of this study was that a calibrating average merger timescale can be found that reliably converts corrected pair counts into merger rates. It depends on the pair identification criteria, stellar mass cut and weakly on redshift and we have presented a simple prescription how to calculate in from these quantities. We find that the average merger timescale is considerably larger for all masses and redshifts than the  $500 \text{ Myr}/h$  typically assumed in the majority of pair studies. Moreover, the intrinsic galaxy merger rate evolution, as also recovered from the mocks, is almost flat out to redshift  $z = 1$ , whereas observational results predict much stronger evo-

## 6. Conclusions

---

lution in the range  $N_{\text{Pair}} \sim (1+z)^{2\pm 2}$ . The large uncertainties are presumably due to small sample sizes and selection effects not sufficiently well taken into account. It was demonstrated that a steeper relation could be the consequence of cutting by magnitude instead of cutting by stellar mass, as we did for this analysis.

Another fundamental result we derived in Chapter 5 is that the flat galaxy merger rate evolution we find is different from the DM halo merger rate which has an intrinsic slope of  $\dot{N} \sim (1+z)^{3/2}$  for all masses. This is due to the extended intrinsic merging time distribution peaking well beyond 1000 Myr/h, contrary to the common assumption that the merging time is well defined and small for the typical selection criteria of galaxy pairs. Such a discrepancy between dark-matter and galaxy merger rates has already been described by other authors, and we follow their conclusion that merger rate studies are less suitable as a probe of cosmic structure formation, as they were originally intended. Instead they can be of great help to understand the formation and evolution of galaxies in a hierarchical universe.

### 6.2. Outlook

The potential of the semi-analytic mock catalogue produced in this work has certainly not been explored in full yet with the simple example in Chapter 5. Instead it was devised for a much more general purpose. These lightcones will help observational astronomers to understand their datasets and systematics involved in the data reduction, as well as providing an important tool for theorists to test their hypotheses about the physical processes shaping galaxies. In practice custom tailored lightcones have already been constructed for two of the most ambitious observational efforts to date to collect a large dataset of faint high redshift galaxies, currently being undertaken by the DEEP2 (Davis et al. 2001) and COSMOS (Scoville et al. 2006) collaborations. Even though very deep pencil beam surveys like these are the most important application of the lightcone catalogues since they depend on the accurate treatment of redshift evolution, in principle also shallow but wide surveys like the SDSS () can be simulated. The only limitation is given by the total survey volume that cannot exceed the volume of the underlying simulation box of 500 Mpc/h cubed. In order to provide the mock catalogues publicly to the astronomical community, a number of lightcones in different filter bands has been made available on the “German Astrophysical Virtual Observatory” database, which can be found under <http://www.mpa-garching.mpg.de/Millennium> together with an explanation of the simulation.

We hope that in this way the mock catalogues will be put to good use by a large number of astronomers and help to further reveal the secrets of galaxy formation and evolution. Ultimately this is the origin of our own history and should guide us in understanding the place of humankind in the universe.

# A

## Appendix

In the following some ideas how to improve the recipes incorporated in the semi-analytic model will be presented, and in the second part it will be briefly investigated how a change of cosmological parameters would affect the model predictions and whether these are sufficient to distinguish between different cosmologies.

### A.1. Possible improvements to the model

The current incarnation of the semi-analytic model seems to agree very well with a range of observations of the local universe such as 2-point correlation functions and luminosity functions (LF). However a more detailed comparison of sub-sets of the galaxy population selected by different criteria has revealed that some of the simulated galaxy properties are not in agreement with their counterparts in the real universe. In particular the satellite galaxies seem to be too passive and red and slightly overabundant. This can be seen in Fig. 11 of (Croton et al. 2006), which shows the simulated B-band LF split up by colour compared to observations (reproduced here as Fig. A.1). It is apparent that there are too many faint red objects and these are predominantly comprised of satellite galaxies, as is illustrated in Fig. A.2 taken from Weinmann et al. (2006). They have compared the fraction of blue galaxies in the SDSS with the semi-analytic predictions and find that in reality a large majority of faint satellites is blue, and thus star forming, whereas in the simulation these galaxies are almost exclusively red and passive.

Wang et al. (2007b) have investigated this issue in more detail by devising a novel type of HOD model which allowed them to attribute characteristic star formation

## A. Appendix

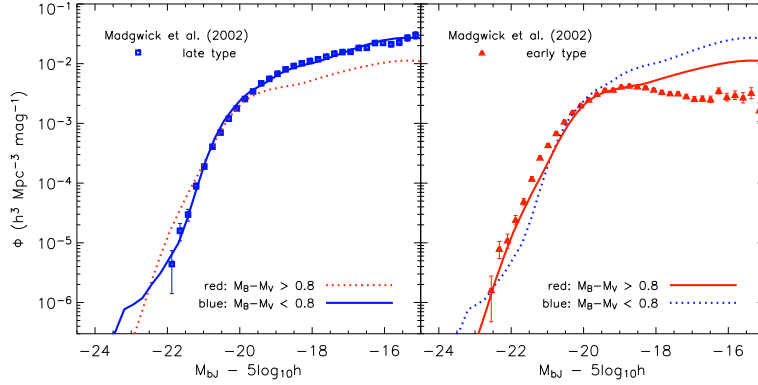


Figure A.1.: Simulated B-band luminosity function split into a red and a blue population. From [Croton et al. \(2006\)](#).

timescales to the satellite galaxies in their simulation which they calibrated with data from the SDSS. They parametrise the SFR with an exponential with fall off time  $\tau$ , where they allow two different timescales for the periods before and after the “infall” time, when a galaxy becomes a satellite. Their results are compared to the star formation rates from the semi-analytic model in Fig. A.3 which suggests that the drop in SFR should be much less rapid. In numbers the fall off time in the semi-analytic model is only 1 Gyr whereas the one inferred from observations should be 2.5 Gyr.

### A.1.1. Star formation in satellites

An obvious reason for the sharp drop in the SFR of satellites is that in our model only central galaxies can cool gas and form stars from it whereas satellites will rapidly use up the reservoir of cold gas they have left such that star formation comes to an end soon after infall into a larger halo. In fact it will not even manage to process all of the remaining cold gas because of our particular star formation recipe that requires the gas surface density to be above a certain critical threshold:

$$\Sigma_{\text{crit}}(R) = 120 \left( \frac{V_{\text{vir}}}{200 \text{ km s}^{-1}} \right) \left( \frac{R}{\text{kpc}} \right)^{-1} M_{\odot} \text{pc}^{-2}. \quad (\text{A.1})$$

which we turned into a critical mass  $m_{\text{crit}}$  assuming a homogeneous distribution of gas over the galaxy disk. So the star formation rate became

$$\dot{m}_{*} = \alpha_{\text{SF}} (m_{\text{cold}} - m_{\text{crit}}) / t_{\text{dyn,disk}}, \quad (\text{A.2})$$

## A.1. Possible improvements to the model

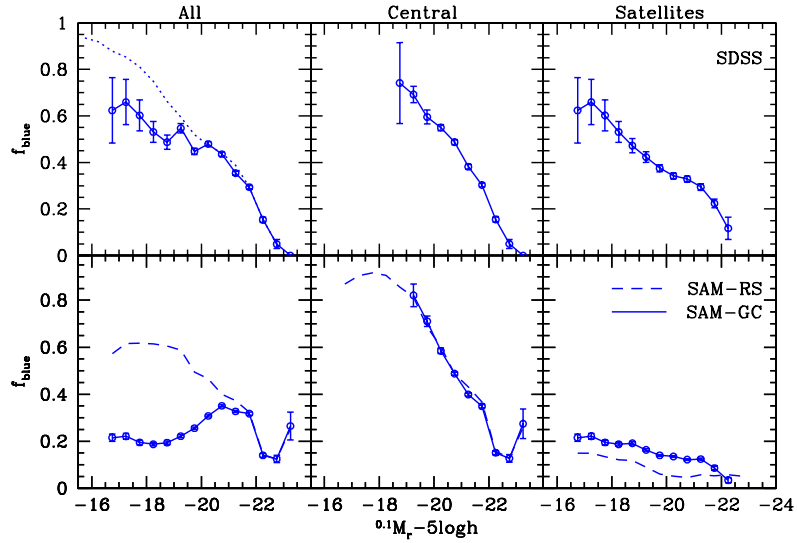


Figure A.2.: The fraction of blue galaxies versus magnitude in the SDSS survey (top) compared to the semi-analytic model predictions (bottom). Clearly satellite galaxies seem to be too red. From [Weinmann et al. \(2006\)](#)

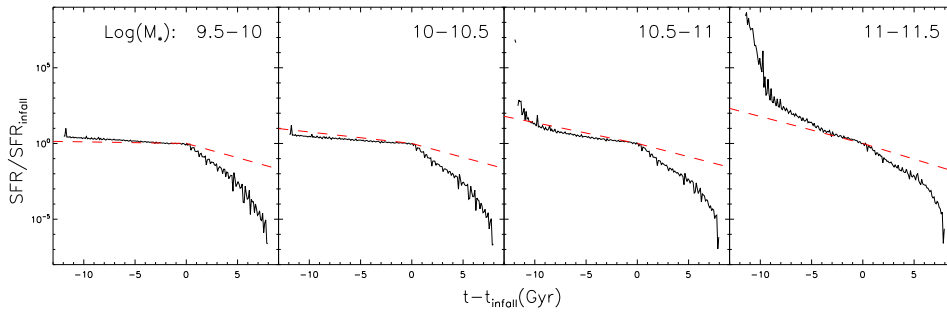


Figure A.3.: Time evolution of the star formation rate in satellite galaxies of different mass ranges. Black is for the semi-analytic model and the dashed red line indicates the evolution inferred from the HOD model in combination with SDSS data (from [Wang et al. 2007b](#)).

from which it is readily apparent that no more stars will be formed after the cold gas mass drops below the threshold value.

## A. Appendix

---

### A.1.2. Disk sizes

The question remains however whether this recipe is universally applicable, even though it seems to give good results for central galaxies. One of the uncertainties by which it is plagued is the strong dependence of the surface density on the assumed disk size, a parameter that we calculate ad-hoc from the properties of the underlying dark matter halo. Since the DM haloes of satellites is embedded in a larger halo and in the process of being tidally stripped, such a derivation is not justified anymore for these galaxies. It would be advantageous to calculate disk sizes from the actual angular momentum of the infalling cold gas at every timestep and to follow the build up of the gas disk much more closely.

### A.1.3. Interactions

Another factor that may be underestimated in the current semi-analytic model is the tidal perturbation of satellites as they experience numerous distant interactions with other members of a galaxy cluster. Observationally this effect is sometimes called “harassment”. Additionally the ram-pressure that works on the gaseous component of a galaxy while it orbits in the hot gas halo of a larger cluster not only leads to the stripping off of its own hot halo and probably the outer parts of its cold gas disk, but it can also lead to a compression of the gas in the disk which would effectively lower the critical surface density required for star formation. Currently the model does not include any environmental effects of this kind, mostly for the sake of efficiency since implementing some “awareness” of its surroundings for each of the more than one billion galaxies in the full simulation would be a rather demanding technical challenge.

### A.1.4. Gas recycling

Finally the apparent lack of cold gas in simulated satellite galaxies may also be a consequence of the simplified treatment of gas recycling that is assumed to be instantaneous in the model, but in reality behaves more like a power law with time and is thus a constant source of recycled gas that could be reincorporated into star formation. First tests have shown that following the gas recycling correctly may help to keep the star formation going for a longer period of time in accordance with observations.

## A.2. WMAP 3rd year cosmology

One aspect of the models that cannot be explored easily is the dependence on cosmological parameters since any change requires to completely redo the N-body simula-



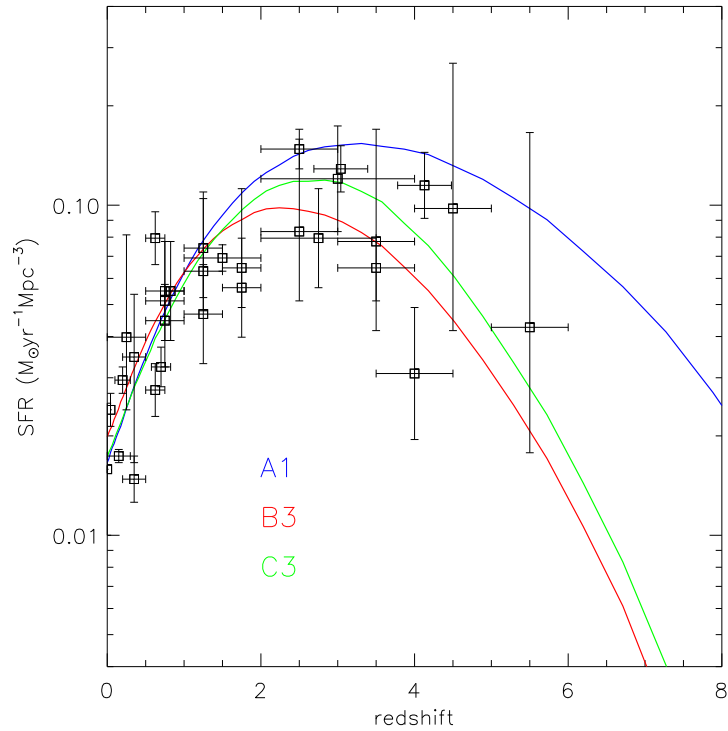


Figure A.4.: Evolution of the cosmic star formation rate in three different semi-analytic models (coloured lines) compared to a compilation of observations (symbols). The cosmological parameters assumed for model A1 are the ones used in the Millennium simulation whereas the other two models were simulated with a lower value of  $\sigma_8$  according to the 3rd year release of WMAP results. (Wang et al. 2007a)

tion from scratch. It would have been too costly to resimulate the whole Millennium run once more with different parameters, but after the release of the 3rd year results from the WMAP satellite it seemed worthwhile to explore the implications of changing to the new values, in particular the much lower  $\sigma_8$ . Wang et al. (2007a) have performed an N-body simulation of one eighth of the volume in the Millennium run with the new cosmological parameters and applied the semi-analytic model to the dark matter merger trees extracted from it. Some of the model parameters for the star formation and feedback recipes had to be adjusted to reestablish agreement with observations of the local universe, but their values remained all in a plausible range

## A. Appendix

---

well within their intrinsic uncertainties. More importantly the changes that had to be made to the recipes in order to achieve agreement were not unique, instead two quite contrary approaches gave equally good results for the present day universe. Also at higher redshift, even though the models did diverge, the observational uncertainties are considerably larger than the differences in the model predictions. This is shown in Fig. A.4, which shows the predictions for the evolution of the cosmic star formation rate, and in Fig. A.5, which compares the stellar mass functions between the models and a compilation of observations. Clearly much better statistics would be required in order to be able to distinguish between the models such that one could rule out all but one. Conversely at the moment no definite constraints on cosmological parameters can be made on the basis of these galaxy formation models since the uncertainties pertaining to the physics of galaxies are much larger than the uncertainties in cosmology.

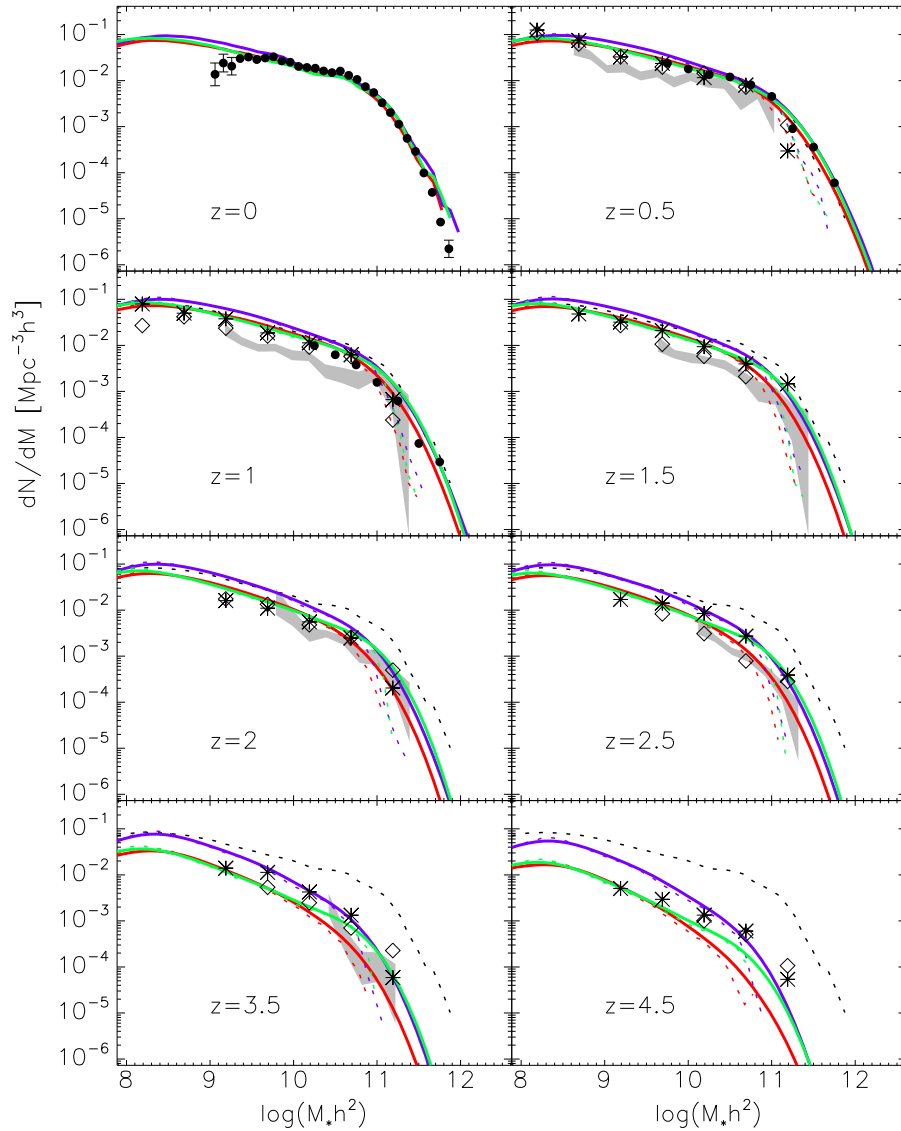


Figure A.5.: The stellar mass function in the redshift range  $z = 0 - 4.5$  for the three models with different cosmological parameters (cf. Fig. 4.7). Locally they are compared to data from Cole et al. (2001) which is repeated as a black dashed line in the higher redshift panels. High redshift data are taken from Drory et al. (2005, symbols) and Fontana et al. (2006, grey shaded areas). Model predictions are shown both with (solid) and without (dotted) convolution with a normal distribution of standard deviation 0.25 representing measurement errors in  $\log M_*$ . (Wang et al. 2007a)

## A. Appendix

---

## Acknowledgements

First and foremost I have to thank my family for allowing me to pursue my interests without compromise. *Ihr habt mich immer ermutigt und in allem unterstützt.* Moreover life wouldn't be the same, and a lot less worth living, without Debora, whom I want to thank for sharing the good and the bad days and always be there.

I am indebted to my supervisor Simon White, for providing critical insights into my work and for every kind of support I received during these three years. Furthermore credit is due to Volker Springel, the father of the Millennium simulation and originator of just about every piece of code I had the pleasure to use during my PhD - except for the bugs of course!

Special thanks have to go to Anja von der Linden, my office mate during most of my time at MPA, who understood when I was not in the mood for conversation because I had to outwit the computer to get it to do what I wanted for once. But she would also always be there to listen to my obscure stories of weekend adventures and car troubles, or lengthy explanations why Austrians are actually totally different from Germans. The same holds for Stefan Hilbert, but in his case no pity needs to be wasted, since he came to our office voluntarily and presumably for exactly this purpose.

I thank the Chinese students, past and present, for interesting conversations, in particular Fan Yi for trying to teach me Chinese and showing infinite patience when we spent six weeks practising the pronunciation of the "Q" sound only - in vain though.

Last but not least I'd like to mention Anna and Stefano, for being good friends, and the rest of the Italians for always being fun company.

Certainly I will have forgotten somebody, so also many special thanks to you, the anonymous benefactor whose name has momentarily slipped my memory!

## Acknowledgements

---

# Curriculum vitae

## Manfred G. Kitzbichler

### PERSONAL DATA

---

Born June 6, 1976 in Kufstein, Austria  
Nationality Austrian  
Current address Max-Planck-Institut für Astrophysik  
Karl-Schwarzschild-Str. 1  
D-85748, Garching b. München, Germany  
Tel.: +49 89 30000 2299  
e-mail: mgk@mpa-garching.mpg.de

### EDUCATION

---

2003 - MPI for Astrophysics / LMU Munich Garching, Germany

---

*Doktor Rerum Naturalium (PhD)*  
International Max-Planck Research School on Astrophysics (IMPRS)  
Doctoral thesis: "Galaxy formation in the Millennium simulation"

1996 - 2003 University of Innsbruck Innsbruck, Austria

---

*Magister Rerum Naturalium*  
Studies of mathematics, astronomy and physics  
First and second diploma exam in physics passed with distinction  
Diploma thesis: "Spatial Orientation of Galaxies in the Coma Cluster"

1999 - 2000 University of Edinburgh Edinburgh, Scotland

---

Year abroad in Scotland - studies of physics

## Curriculum vitae

---

1995 - 1996	Austrian Military	Lienz, Austria
	<i>Corporal</i> Training as radio operator with specialisation in encrypted transmission Assistance mission at the eastern border	
1990 - 1995	Höhere Technische Lehranstalt I	Innsbruck, Austria
	<i>A-level with distinction</i> Training as electronics engineer and education in communication technologies	
1986 - 1990	Grammar School	Kufstein, Austria
	English and Latin	
1982 - 1986	Elementary School	Erl, Austria

### LANGUAGES

---

Native	German: in the flavours Standard German and Tyrolean
Foreign	Official certificates for courses in these languages (one year or more of studies) English: fluent in spoken and written English French: basic linguistic survival skills

### CONFERENCES

---

Conferences, meetings, and schools (involving a talk and/or poster presentation)		
November 2006	Invited Talk	Innsbruck, Austria
September 2006	COSMOS Team Meeting	Ringberg castle, Germany
December 2005	EGS Team Meeting	Berkeley, USA
June 2005	Guillermo-Haro Int. Advanced School	Puebla, Mexico
May 2005	COSMOS Team Meeting	Kyoto, Japan
April 2005	VIRGO Consortium Meeting	Garching, Germany
February 2005	Invited Talk	Innsbruck, Austria
December 2004	EGS Team Meeting	Berkeley, USA
December 2003	Winter School in Theoretical Physics	Jerusalem, Israel
November 2003	VIRGO Consortium Meeting	Durham, UK
September 2003	Meeting of the Astron. Gesellschaft	Freiburg, Germany
June 2003	Cosmology Graduate School	Balatonfüred, Hungary
April 2003	Austrian Astronomers Meeting	Innsbruck, Austria
September 2002	Meeting of the Astron. Gesellschaft	Berlin, Germany
May 2002	Austrian Astronomers Meeting	Graz, Austria



AWARDS AND FELLOWSHIPS

---

2004 - 2005            Marie Curie Fellowship of the European Union

---

Selected as a fellow to participate in a Marie Curie Host Fellowship for Early Stage Research Training granted to the International Max-Planck Research School.

2003 - 2006            IMPRS Fellowship

---

PhD fellowship of the International Max-Planck Research School (IMPRS) on Astrophysics

2003                    Faculty Award for Young Scientists

---

One of three laureates from the department of physics receiving the Faculty Award for Young Scientists from the Faculty of Natural Sciences at Innsbruck University.

## Curriculum vitae

---

# Bibliography

- Abraham, R. G., van den Bergh, S., & Nair, P. 2003, *ApJ*, 588, 218 104
- Adelberger, K. L. & Steidel, C. C. 2000, *ApJ*, 544, 218 35, 68
- Andreon, S. 2002, *A&A*, 382, 495 54
- Arimoto, N. & Yoshii, Y. 1987, *A&A*, 173, 23 47
- Barnes, J. & Hut, P. 1986, *Nature*, 324, 446 23, 66
- Bell, E. F. & de Jong, R. S. 2001, *ApJ*, 550, 212 60, 83
- Bell, E. F., Phleps, S., Somerville, R. S., et al. 2006, *ApJ*, 652, 270 93
- Bell, E. F., Wolf, C., Meisenheimer, K., et al. 2004, *ApJ*, 608, 752 48
- Berrier, J. C., Bullock, J. S., Barton, E. J., et al. 2006, *ApJ*, 652, 56 93, 100
- Binney, J. & Tremaine, S. 1987, *Galactic dynamics* (Princeton, NJ, Princeton University Press, 1987, 747 p.) 95
- Blaizot, J., Wadadekar, Y., Guiderdoni, B., et al. 2005, *MNRAS*, 360, 159 65, 69, 73
- Blanton, M. R., Hogg, D. W., Bahcall, N. A., et al. 2003, *ApJ*, 592, 819 49, 50
- Bond, J. R., Cole, S., Efstathiou, G., & Kaiser, N. 1991, *ApJ*, 379, 440 99
- Bower, R. G., Benson, A. J., Malbon, R., et al. 2006, *MNRAS*, 370, 645 64, 65, 88
- Bruzual, G. & Charlot, S. 2003, *MNRAS*, 344, 1000 50, 52
- Burkey, J. M., Keel, W. C., Windhorst, R. A., & Franklin, B. E. 1994, *ApJ*, 429, L13 92
- Capak, P., Cowie, L. L., Hu, E. M., et al. 2004, *AJ*, 127, 180 76
- Caputi, K. I., McLure, R. J., Dunlop, J. S., Cirasuolo, M., & Schael, A. M. 2006, *MNRAS*, 366, 609 78

## Bibliography

---

- Cardelli, J. A., Clayton, G. C., & Mathis, J. S. 1989, *ApJ*, 345, 245–35, 67
- Charlot, S. & Fall, S. M. 2000, *ApJ*, 539, 718–36
- Chen, H., Marzke, R. O., McCarthy, P. J., et al. 2003, *ApJ*, 586, 745–47, 64
- Ciardi, B., Ferrara, A., & White, S. D. M. 2003, *MNRAS*, 344, L7–27
- Cimatti, A., Daddi, E., Cassata, P., et al. 2003, *A&A*, 412, L1–86
- Cimatti, A., Daddi, E., Mignoli, M., et al. 2002a, *A&A*, 381, L68–86
- Cimatti, A., Daddi, E., Renzini, A., et al. 2004, *Nature*, 430, 184–48
- Cimatti, A., Mignoli, M., Daddi, E., et al. 2002b, *A&A*, 392, 395–54
- Cimatti, A., Pozzetti, L., Mignoli, M., et al. 2002c, *A&A*, 391, L1–47, 58, 64, 77, 124
- Cole, S., Lacey, C. G., Baugh, C. M., & Frenk, C. S. 2000, *MNRAS*, 319, 168–68
- Cole, S., Norberg, P., Baugh, C. M., et al. 2001, *MNRAS*, 326, 255–81, 82, 83, 85, 133
- Colless, M., Dalton, G., Maddox, S., et al. 2001, *MNRAS*, 328, 1039–23, 66, 94
- Croton, D. J., Springel, V., White, S. D. M., et al. 2006, *MNRAS*, 365, 11–5, 7, 25, 63, 64, 65, 66, 67, 78, 79, 81, 86, 87, 88, 93, 95, 124, 127, 128
- Davis, M., Newman, J. A., Faber, S. M., & Phillips, A. C. 2001, in *Deep Fields*, ed. S. Cristiani, A. Renzini, & R. E. Williams, 241–+ 5, 7, 126
- De Lucia, G. & Blaizot, J. 2007, *MNRAS*, 375, 2–5, 7, 25, 36, 63, 64, 65, 66, 67, 87, 88, 89, 93, 95, 124, 125
- De Lucia, G., Kauffmann, G., & White, S. D. M. 2004, *MNRAS*, 349, 1101–26, 29, 67, 95
- De Lucia, G., Springel, V., White, S. D. M., Croton, D., & Kauffmann, G. 2006, *MNRAS*, 366, 499–64, 65, 79, 88, 89, 125
- Devriendt, J. E. G. & Guiderdoni, B. 2000, *A&A*, 363, 851–34, 67
- Devriendt, J. E. G., Guiderdoni, B., & Sadat, R. 1999, *A&A*, 350, 381–34, 67
- Drory, N., Salvato, M., Gabasch, A., et al. 2005, *ApJ*, 619, L131–83, 85, 133

- Faber, S. M., Willmer, C. N. A., Wolf, C., et al. 2005, ArXiv Astrophysics: astro-ph/0506044 84
- Feulner, G., Bender, R., Drory, N., et al. 2003, MNRAS, 342, 605 81, 82
- Firth, A. E., Somerville, R. S., McMahon, R. G., et al. 2002, MNRAS, 332, 617 47
- Fontana, A., Menci, N., D'Odorico, S., et al. 1999, MNRAS, 310, L27 47, 64
- Fontana, A., Pozzetti, L., Donnarumma, I., et al. 2004, A&A, 424, 23 60, 61
- Fontana, A., Salimbeni, S., Grazian, A., et al. 2006, A&A, 459, 745 83, 85, 133
- Gardner, J. P. 1998, PASP, 110, 291 50, 55, 59
- Gavazzi, G., Boselli, A., & Kennicutt, R. 1991, AJ, 101, 1207 52
- Glazebrook, K., Abraham, R. G., McCarthy, P. J., et al. 2004, Nature, 430, 181 48
- Gnedin, N. Y. 2000, ApJ, 542, 535 27
- Hatton, S., Devriendt, J. E. G., Ninin, S., et al. 2003, MNRAS, 343, 75 68
- Hockney, R. W. & Eastwood, J. W. 1981, Computer Simulation Using Particles (Computer Simulation Using Particles, New York: McGraw-Hill, 1981) 23, 66
- Holmberg, E. 1937, Annals of the Observatory of Lund, 6, 1 92
- Im, M., Simard, L., Faber, S. M., et al. 2002, ApJ, 571, 136 47, 64
- Inoue, A. K. 2003, PASJ, 55, 901 35, 68
- Kashikawa, N., Takata, T., Ohyama, Y., et al. 2003, AJ, 125, 53 47, 64, 78
- Kauffmann, G. 1996, MNRAS, 281, 475 27
- Kauffmann, G. & Charlot, S. 1998, MNRAS, 294, 705 46, 67, 95
- Kauffmann, G., Colberg, J. M., Diaferio, A., & White, S. D. M. 1999, MNRAS, 303, 188 33, 67, 95
- Kauffmann, G. & Haehnelt, M. 2000, MNRAS, 311, 576 29, 67, 95
- Kauffmann, G., Heckman, T. M., White, S. D. M., et al. 2003, MNRAS, 341, 33 59, 60, 83
- Kauffmann, G., White, S. D. M., & Guiderdoni, B. 1993, MNRAS, 264, 201 66, 95
- Khochfar, S. & Burkert, A. 2001, ApJ, 561, 517 93

## Bibliography

---

- Kitzbichler, M. G. & White, S. D. M. 2006, MNRAS, 366, 858 65
- Kitzbichler, M. G. & White, S. D. M. 2007, MNRAS, 376, 2 25, 93, 95, 102
- Kochanek, C. S., Pahre, M., Falco, E., et al. 2001, ApJ, 560, 566 52, 54
- Kong, X., Charlot, S., Brinchmann, J., & Fall, S. M. 2004, MNRAS, 349, 769 36
- Kong, X., Daddi, E., Arimoto, N., et al. 2006, ApJ, 638, 72 76, 86
- Kravtsov, A. V., Gnedin, O. Y., & Klypin, A. A. 2004, ApJ, 609, 482 67, 95
- Lacey, C. & Cole, S. 1993, MNRAS, 262, 627 93, 99
- Le Fèvre, O., Abraham, R., Lilly, S. J., et al. 2000, MNRAS, 311, 565 93
- Le Fèvre, O., Paltani, S., Arnouts, S., et al. 2005, Nature, 437, 519 86
- Lemson, G. et al. 2006, ArXiv Astrophysics: astro-ph/0608019 64, 66, 87, 95
- Li, C., Kauffmann, G., Jing, Y. P., et al. 2006, MNRAS, 368, 21 88, 96, 97
- Limber, D. N. 1953, ApJ, 117, 134 105
- Lin, L., Koo, D. C., Weiner, B. J., et al. 2006, ArXiv Astrophysics e-prints 104
- Lin, L., Koo, D. C., Willmer, C. N. A., et al. 2004, ApJ, 617, L9 93, 100
- Lotz, J. M., Davis, M., Faber, S. M., et al. 2006, ArXiv Astrophysics e-prints 93, 100
- Lotz, J. M., Primack, J., & Madau, P. 2004, AJ, 128, 163 104
- Martin, C. L. 1999, ApJ, 513, 156 28
- Meyer, M. J., Zwaan, M. A., Webster, R. L., Brown, M. J. I., & Staveley-Smith, L. 2007, ApJ, 654, 702 88
- Mo, H. J., Mao, S., & White, S. D. M. 1998, MNRAS, 295, 319 28
- Mobasher, B., Idzi, R., Benítez, N., et al. 2004, ApJ, 600, L167 54, 77
- Nagashima, M., Lacey, C. G., Baugh, C. M., Frenk, C. S., & Cole, S. 2004, ArXiv Astrophysics e-prints 51, 58, 123
- Norberg, P., Cole, S., Baugh, C. M., et al. 2002, MNRAS, 336, 907 78, 80
- Page, T. 1952, ApJ, 116, 63 92

- Patton, D. R., Grant, J. K., Simard, L., et al. 2005, *AJ*, 130, 2043–104
- Patton, D. R., Pritchett, C. J., Yee, H. K. C., Ellingson, E., & Carlberg, R. G. 1997, *ApJ*, 475, 29–93
- Peebles, P. J. E. 1993, *Principles of physical cosmology* (Princeton Series in Physics, Princeton, NJ: Princeton University Press, —c1993) 15
- Penzias, A. A. & Wilson, R. W. 1965, *ApJ*, 142, 419–14
- Poli, F., Giallongo, E., Fontana, A., et al. 2003, *ApJ*, 593, L1–84
- Pozzetti, L., Cimatti, A., Zamorani, G., et al. 2003, *A&A*, 402, 837–48, 64, 81, 82
- Prescott, M., Impey, C., Scoville, N., & COSMOS Collaboration. 2004, in *Bulletin of the American Astronomical Society*, Vol. 36, 728–+ 104
- Press, W. H. & Schechter, P. 1974, *ApJ*, 187, 425–99
- Reddy, N. A., Steidel, C. C., Fadda, D., et al. 2006, *ApJ*, 644, 792–35, 68
- Renzini, A. 2006, *ARA&A*, 44, 141–86
- Rudnick, G., Franx, M., Rix, H., et al. 2001, *AJ*, 122, 2205–47
- Saracco, P., Fiano, A., Chincarini, G., et al. 2006, *MNRAS*, 367, 349–81, 82, 84
- Saracco, P., Giallongo, E., Cristiani, S., et al. 2001, *A&A*, 375, 1–76
- Saracco, P., Longhetti, M., Severgnini, P., et al. 2005, *MNRAS*, 357, L40–48
- Scoville, N., Aussel, H., Brusa, M., et al. 2006, *ArXiv Astrophysics e-prints* 5, 7, 126
- Seljak, U., Makarov, A., McDonald, P., et al. 2005, *Phys. Rev. D*, 71, 103515–23, 66, 94
- Sijacki, D. & Springel, V. 2006, *MNRAS*, 371, 1025–30
- Smail, I., Chapman, S. C., Blain, A. W., & Ivison, R. J. 2004, *ApJ*, 616, 71–60, 61
- Somerville, R. S., Moustakas, L. A., Mobasher, B., et al. 2004, *ApJ*, 600, L135–47, 54, 59, 64
- Spergel, D. N., Verde, L., Peiris, H. V., et al. 2003, *ApJS*, 148, 175–23, 66, 94
- Springel, V. 2005, *MNRAS*, 364, 1105–23, 66, 94

## Bibliography

---

- Springel, V., Frenk, C. S., & White, S. D. M. 2006, *Nature*, 440, 1137–72
- Springel, V. & Hernquist, L. 2003, *MNRAS*, 339, 289–29
- Springel, V., White, S. D. M., Jenkins, A., et al. 2005, *Nature*, 435, 629–7, 23, 64, 66, 87, 88, 94, 124
- Springel, V., White, S. D. M., Tormen, G., & Kauffmann, G. 2001a, *MNRAS*, 328, 726–26, 67, 95
- Springel, V., Yoshida, N., & White, S. D. M. 2001b, *New Astronomy*, 6, 79–23, 66, 94
- Tinsley, B. M. 1980, *ApJ*, 241, 41–46, 61, 124
- Toomre, A. 1977, in *Evolution of Galaxies and Stellar Populations*, ed. B. M. Tinsley & R. B. Larson, 401–92
- Toomre, A. & Toomre, J. 1972, *ApJ*, 178, 623–92
- Totani, T. & Yoshii, Y. 2000, *ApJ*, 540, 81–47
- Totani, T., Yoshii, Y., Maihara, T., Iwamuro, F., & Motohara, K. 2001, *ApJ*, 559, 592–47, 55, 59, 124
- van Dokkum, P. G., Franx, M., Fabricant, D., Kelson, D. D., & Illingworth, G. D. 1999, *ApJ*, 520, L95–52
- van Dokkum, P. G. & Stanford, S. A. 2003, *ApJ*, 585, 78–51, 53
- Wang, B. & Heckman, T. M. 1996, *ApJ*, 457, 645–67
- Wang, J., De Lucia, G., Kitzbichler, M. G., & White, S. D. M. 2007a, *ArXiv e-prints*, 706–131, 133
- Wang, L., Li, C., Kauffmann, G., & de Lucia, G. 2006, *MNRAS*, 371, 537–88
- Wang, L., Li, C., Kauffmann, G., & De Lucia, G. 2007b, *MNRAS*, 377, 1419–127, 129
- Weinmann, S. M., van den Bosch, F. C., Yang, X., et al. 2006, *MNRAS*, 372, 1161–88, 127, 129
- White, S. D. M. & Frenk, C. S. 1991, *ApJ*, 379, 52–26, 66, 95
- Willmer, C. N. A., Faber, S. M., Koo, D. C., et al. 2006, *ApJ*, 647, 853–78, 80
- Woods, D., Fahlman, G. G., & Richer, H. B. 1995, *ApJ*, 454, 32–93



## Bibliography

---

Yee, H. K. C. & Ellingson, E. 1995, *ApJ*, 445, 37–105

York, D. G., Adelman, J., Anderson, J., et al. 2000, *AJ*, 120, 1579–49

Zamojski, M. A., Schiminovich, D., Rich, M., et al. 2006, in *American Astronomical Society Meeting Abstracts*, Vol. 209, 225.04–104

Zepf, S. E. & Koo, D. C. 1989, *ApJ*, 337, 34–92, 105